Resisting Resistance: Development of Nanoparticle-mediated Delivery Systems to Explore RNA Interference as a Solution to Biological Resistance

by

Erin McGraw

A dissertation submitted to the Graduate Faculty of
Auburn University
in partial fulfillment of the
requirements for the Degree of
Doctor of Philosophy

Auburn, Alabama
May 10, 2025

Keywords: nanoparticle, resistance, RNA interference, photoporation, fungal infection, pest management

Approved by

Adriana Avila Flores, Chair, Associate Professor of Biological Sciences
Paul Cobine, Lawrence C. Whit Professor and Chair of Biological Sciences
Allan David, John W. Brown Associate Professor of Chemical Engineering
Jason Upton, Associate Professor of Biological Sciences

Abstract

Biological resistance to conventional pesticides and antifungals presents a significant challenge in agriculture and healthcare, necessitating the development of alternative control strategies. RNA interference (RNAi) offers a highly specific and environmentally sustainable approach to managing resistance, but its widespread application is hindered by the lack of efficient RNA delivery methods. This dissertation explores nanoparticle-mediated delivery systems for double-stranded RNA (dsRNA) to enhance RNAi efficiency in both fungal and insect models.

While RNAi is a promising tool for gene regulation, the clear structural and physiological differences between yeast and insects necessitate distinct delivery approaches. For delivery in yeast, we developed the first nanoparticle-mediated photoporation system focused on delivery into fungal cells. This required the meticulous optimization of laser power, wavelength, irradiation time, and several nanoparticle characteristics to maximize RNA uptake while maintaining cell viability. All optimizations were done in *Saccharomyces cerevisiae* before moving on to gene silencing in the clinically-relevant pathogen, *Candida albicans*. In contrast, we investigated branched amphiphilic peptide nanocapsules (BAPCs), a biologically-derived peptide-based nanoparticle, for RNAi delivery in the fall armyworm (*Spodoptera frugiperda*), a major agricultural pest, where nanoparticle concentration and silencing efficiency were studied. Additionally, cellular uptake and trafficking mechanisms were studied using Sf9 cells. Gene silencing efficacy was evaluated in both models using RT-qPCR.

Our findings demonstrate that photoporation successfully facilitates the intracellular delivery of various molecules in yeast, marking the first application of this technique in fungal systems. Additionally, fall armyworms readily consume BAPCs complexed with dsRNA, resulting in effective gene silencing. Evidence suggests that transcytosis plays a role in nanoparticle transport from the gut to systemic tissues, highlighting a potential mechanism for RNAi-based pest control.

This work enhances the field of drug delivery through the development and optimization of of new delivery methodologies and providing insights into mechanisms surrounding nanoparticle-mediated RNA delivery in fungal and insect systems. By bridging the gap between laboratory research and field applications, these nanoparticle-mediated RNAi delivery strategies provide a foundation for novel RNA-based fungicides and insecticides as sustainable alternatives to current chemical treatments.

Acknowledgments

Everyone always says that ~~raising a child~~ writing a dissertation takes a village, and it is not lost on me how lucky I am for my village. First and foremost, I would like to express my deepest gratitude to my advisor, Dr. Adriana Avila Flores. Your unwavering support, patience with my chaotic schedules, and invaluable guidance have been instrumental in shaping both this research and my academic growth. Thank you for your constant feedback, encouragement, and for always pushing me to think critically and aim higher.

I am also incredibly grateful to my committee members and reader – Dr. Paul Cobine, Dr. Allan David, Dr. Jason Upton, and Dr. Jeff Coleman – for their time, support, and insightful advice throughout this journey. Their expertise and mentorship have greatly enriched my research and professional development. I also want to thank Dr. Guillaume Laurent, whose collaboration made much of this work possible.

I never would have gotten here without the love and support of my family, Mom, Uncle Chris, and Aunt Sharlene, who have always believed in me and pushed me to be my absolute best. Words can't justify my appreciation for my husband, Ayden, who has always been my go-to sounding board and who keeps me balanced when life is crazy. To my best friends, Amanda, Serena, Romayne, Brielle, and Benji, your unquestionable love, patience, and encouragement have kept me grounded and motivated through this process. A special thanks is not enough for Nana, Dixie McGraw, who was my #1 partner in crime. I couldn't have done any of this without her encouragement. I love and miss you so much.

To my lab mates - Nitish, Collin, Emilee, Jose, Maede, Aanchal, and Chris - thank you for the camaraderie, the discussions (scientific and otherwise), and for making long hours in the lab more enjoyable.

Finally, I would like to acknowledge the funding and resources provided by Auburn University, NIH, NSF, USDA, and Phoreus Biotech. Their support made this research possible.

Table of Contents

List of Tables

List of Figures

Chapter 1

Introduction:
Breaking the Resistance Cycle: Understanding Biological Resistance Against Antifungals and Pesticides

1.1 Background

Biological resistance, or the ability of an organism to withstand the effects of a harmful chemical agent, impacts human health and food security worldwide. This phenomenon typically arises as a result of prolonged or repeated exposure to sub-lethal doses of treatments, such as antimicrobials, pesticides, or other toxins[5, 6]. Individuals within a population that survive exposure to a chemical agent may produce offspring with an increased prevalence of resistant traits, and over time, this cycle renders previously reliable control measures obsolete. This issue is especially prevalent in medicine and agriculture, both of which must constantly battle with invasive, treatment-resistant organisms.

Medical antimicrobial resistance (AMR) is a well-known phenomenon in several pathogens. While AMR is most widely studied in bacteria such as methicillin-resistant *Staphylococcus aureus*, highly resistant fungal pathogens also exist[7]. Treatment-resistant fungal pathogens contribute to prolonged illnesses, increased hospitalization rates, and higher medical costs, as once easily treatable infections become more difficult to manage[1, 8]. This contributes to elevated morbidity and mortality rates, particularly among vulnerable populations such as immunocompromised individuals, the elderly, and those undergoing surgeries or cancer treatments[1]. Beyond direct medical ramifications, AMR has significant societal and economic impacts (**Table 1.1**), including productivity loss due to prolonged illness, increased caregiving burdens, and a decline in overall quality of life[1]. If left unaddressed, the infection-associated risk of many medical procedures and treatments, such as organ transplants and chemotherapy, will continue to increase due to the expanding threat of antifungal resistance.

The recent prevalence of antifungal resistance has increased the urgency to develop alternative antifungal strategies[8, 9, 10]. In 2022, the World Health Organization released the first Fungal Priority Pathogens List, in which 19 prominent fungal pathogens were classified as critical, high, or medium priority based on factors such as perceived R&D need and public health impact[11]. Several species of *Candida* are featured in all categories: *C. auris* and *C. albicans* as critical threat; *C. glabrata*, *C. parapslosis*, and *C. tropicalis* as high threat; and *C. krusei* as medium threat. Several of these organisms are known to be single- or multi-drug resistant, especially *C. albicans*, a highly prevalent commensal organism that opportunistically causes infection and may become invasive if able to spread[12]. Treating these infections with ineffective or long-term, low-dose antifungals has also resulted in the development of secondary resistance and multi-drug resistance, which can be seen in organisms such as *C. auris*, *C. albicans*, and *C. glabrata*[12, 13, 14].

Disease	Direct Medical Costs	Productivity Losses From Workdays Lost Due to Hospitalizations	Productivity Losses From Workdays Lost Due to Outpatient Visits	Productivity Losses From Premature Deaths	Total Economic Burden
Aspergillosis	$1 291 497 039	$64 749 568	$1 629 791	$419 411 905	$1 777 288 304
Blastomycosis	$24 075 459	$3 503 953	$1 875 481	$44 289 490	$73 744 383
Candida Infection					
Invasive candidiasis	$1 240 388 451	$75 219 548	$501 819	$446 944 883	$1 763 054 702
Noninvasive candidiasis	$2 129 492 530	$14 198 320	$156 492 565	$272 990 358	$2 573 173 773
Coccidioidomycosis	$204 254 578	$24 496 036	$15 098 644	$141 237 843	$385 087 101
Cryptococcosis	$265 266 472	$26 868 318	$820 762	$241 638 975	$534 594 527
Dermatophytosis	$845 434 279	$677 644	$330 556 668	$8 423 048	$1 185 091 639
Histoplasmosis	$222 446 966	$15 650 824	$10 089 587	$84 602 342	$332 789 720
Pneumocystis pneumonia	$489 284 857	$56 065 629	$461 170	$298 512 981	$844 324 636
Mucormycosis	$129 012 825	$7 374 017	$13 581	$123 704 121	$260 104 544
Other and unspecified mycoses	$897 365 285	$37 927 041	$12 980 425	$1 117 224 732	$2 065 497 482
Total	$7 463 346 840	$326 730 897	$530 520 495	$3 198 980 677	$11 519 578 908

Table 1.1: Economic Burden of Various Diseases. Reproduced with permission from Ref.[1].

In agriculture, the growing threat of biological resistance in insect species has placed enormous pressure on farmers to find new strategies for pest management. As traditional insecticides become less effective, farmers are often forced to apply higher doses, resort to more toxic alternatives, or invest in costly new technologies such as genetically modified crops[3, 15]. The overuse of chemical pesticides also results in soil depletion, contamination of water sources, and harm to off-target beneficial insects such as pollinators[16]. These cascading environmental and economic impacts effects ultimately affect long-term crop yields, food security, and agricultural sustainability world-wide.

Invasive insect pests alone are estimated to be responsible for destroying 20-40% of harvested crops and cost over $76.9 billion in damages to goods, services, and human health **Figure 1.1**.[15, 3] For example, *Spodoptera frugiperda*, or the fall armyworm, is a lepidopteran pest that rapidly adapts to a variety of enviornemnts and has become resistant to a majority of pesticides[17, 18]. *S. frugiperda* infestations have been recorded around the world, from southern Alabama to Brazil to sub-Saharan Africa. This environmental adaptability, polyphagous nature, and immense voracity all contribute to the increase of resistance[17]. Typically, infestations are treated with conventional pesticides, transgenic crops, or a combination of these, but a growing number of reports on growing multi-drug resistance has raised concerns on how to effectively manage this pest[16, 17, 18, 19].

Consequences of biological resistance stemming from both medicine and agriculture are far-reaching – impacting human health, creating economic burden, and harming the environment[20, 21]. Addressing this issue requires a multifaceted approach including developing alternatives to current chemical agents and optimizing delivery systems to increase the targeted uptake of molecules. To achieve this, new strategies which leverage innate cellular machinery, such as RNA processing pathways, are being designed to replace traditional treatments[22, 23, 24]. Furthermore, nanoparticle-mediated delivery methods are being explored to enhance cellular uptake for more effective treatment[24, 25]. Combined, these technologies provide a promising blueprint for overcoming biological resistance.

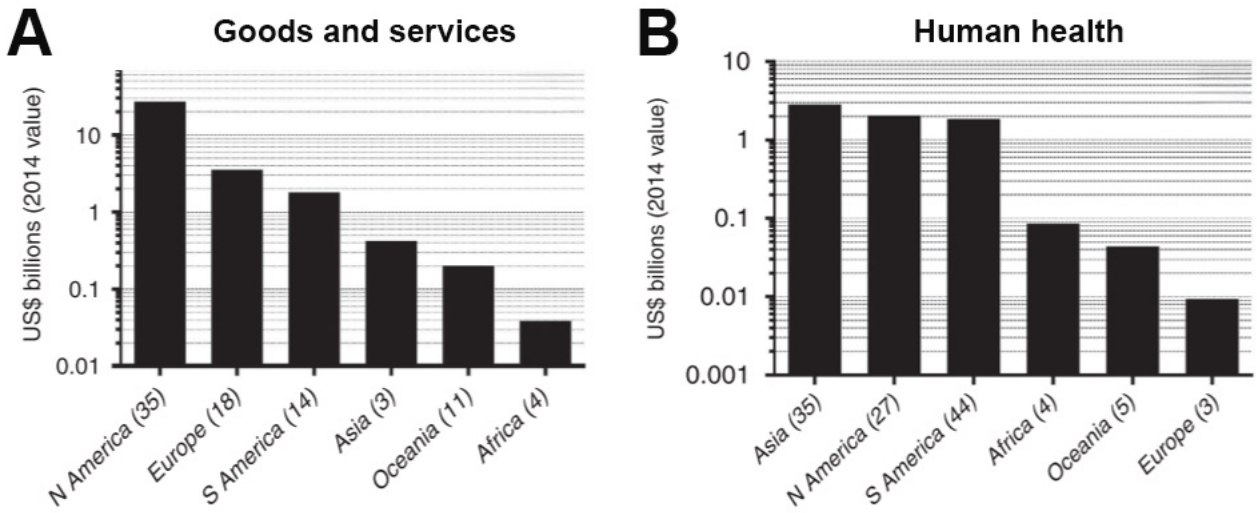

Figure 1.1: Economic impact of insect pests on (A) goods and services and (B) human health. Reproduced from Ref. [3] © 2016, Bradshaw et al., Springer Nature.

1.2 Mechanisms of Resistance

1.2.1 Antifungal Resistance

Antifungal resistance is becoming increasingly more prevalent, especially in *Candida* species[7]. Antifungal drugs typically target cell wall components or the associated synthesis pathways, as the fungal cell wall is essential for cell viability and plays a significant role in pathogenesis[26, 27]. However, many of these medications require prolonged exposure, especially for dermatological and other topical infections[28, 29]. Prolonged exposure to non-lethal treatment vastly increases the potential of an organism to develop resistance. Primary resistance is becoming more common in *Candida* species, especially to azoles and pyrimidines[27, 30], while the continues use of ineffective medications amplifies the occurrence of secondary resistance. Resistance development may occur through the mutation or over-expression of the drug target, increased presence of detoxifying pumps, or changes to the microenvironment of the target that reduces the drug effect[28, 7]. **Table 1.2** summarizes the four common classes of antifungals, their mode of action, and the mechanisms by which resistance is known to develop.

Drug class	Examples	Drug Action	Resistance Mechanism	Ref
Azoles	Triazoles (fluconazole, itraconazole) Imidazoles (ketoconazole)	Inhibits CYP51A1, causing cytotoxic sterol intermediate buildup	1)Binding site mutation 2) Over-expression of drug target and efflux pumps	[10, 7]
Polyenes	Amphotericin B, Nystatin	Binds ergosterol causing membrane destabilization and loss from ergosterol-dependent pathways.	Reduction or modification of ergosterol in the plasma membrane	[7, 31]
Echinocandins	Caspofungin, micafungin, anidulafungin, rezafungin	Binds Fks1p subunit of β-1,3-D-glucan synthase, destabilizing plasma membrane	1) Mutation of the FKS subunit binding site 2) Changes in membrane lipid composition	[10, 32]
Prymidines	5-fluorcytosine	Inhibits DNA, RNA, and protein synthesis as fluorodeoxyuridine monophosphate or fluorouridine triphosphate	Mutations in pyrimidine salvage pathway enzymes and increased production of pyrimidines	[33, 34]

Table 1.2: Available antifungals, their mechanism, and how resistance is developed.

1.2.2 Insecticide Resistance

The development of insecticide resistance involves multiple variables at the cell, organismal, and ecological levels. Conventional pesticides come in many forms. Solids (pellets, baits, dusts, or suspensions) are most commonly used, which insects consume alongside or in place of crops. Similarly, liquid formulations (solutions, pure compounds, or emulsions) may be consumed, or they may soak through the insect's protective outer matrix, called the cuticle. Major factors that contribute to pesticide resistance include insect behavior, physical defenses, metabolic detoxification, target mutation, and environmental fillip and are discussed below:

- Behavioral - Changes in behavior to avoid or reduce the uptake of pesticides is an insect's first line of defense. Many behavioral activities that limit pesticides exposure or intake have been documented, such as avoidance of treated areas, changes in mating and oviposition, changes in activity cycles, and self- or mutual cleaning of colony members[15, 35]. For example, insecticide repellence (non-contact) and irritability (post-contact) has been documented in several species[21].

- Physical - Physical resistance occurs through thickening of the insect cuticle, a protective, double layered coating composed of lipids, proteins, and chitin[36]. Although natural thickening occurs as a result of aging, some evidence suggests that this mechanism may have evolved as an alternative to detoxification[36, 6]. As a result, chemical agents can be slowed or fully prevented from entering the insect body.

- Metabolic - An insect's ability to break down a chemical into a lesser or non-toxic form is referred to as detoxification. Overproduction of detoxifying enzymes, mainly carboxylesterases, glutathione S-transferases, and cytochrome P450 monooxygenases all contribute to this resistance. Studies have shown that inhibition or silencing of especially cytochrome P450 effectively decreases resistance to insecticides[16, 37, 19]. Even higher populations of bacteria capable of degrading pesticides have been found in the gut microbiome of several orders of insects[15].

- Mutation - Changes in the target structure or accessibility of the agent to access the target can render a pesticide fully ineffective. For example, the most common insecticides inhibit neurotransmitters, such as acetylcholinesterase and voltage-gated sodium channels[15, 38]. Evidence of nucleotide- and amino acid-level mutations in these targets has been found widely in *S. frugiperda*, making them highly resistant to insecticides that target these channels such as pyrethroids, carbamates, and organophosphates. Even more modern chemicals that are used to control Lepidopteran pests, such as diamides and *Bacillus thuringiensis* (*Bt*) proteins produced in transgenic plants.

- Environmental - This category, while more challenging to comprehensively study, encompasses fitness, environmental, and human-derived factors that contribute to resistance. Fitness is influenced by the duration of different development phases (e.g, egg, larvae, nymph, adult, etc.), reproduction modes (sexual or asexual), and other factors that influence genetic recombination[15]. Additionally, generation times, lifespan, and population growth also impact resistance. Environmental and human-derived factors, such as food availability, repeated use of similar pesticide formulations, treatment of expansive areas, and the lack of refuge, also impact other forms of resistance, such as behavior and fitness[39, 5].

The interconnected nature of these factors often necessitates the use of higher doses, more toxic insecticides, or combinations of multiple strategies to account for multiple instances of them at once. However, this raises the potential of impacting human health and harming the environment through killing beneficial insects, reducing soil quality, and polluting ground water[15]. Thus, new strategies should ideally incorporate eco-friendly strategies that target harmful insects, like *S. frugiperda*, while limiting off-target effects.

1.3 RNA as a Potential Solution to Biological Resistance

1.3.1 Role and function of RNA

Ribonucleic acids (RNAs) are versatile nucleic acids that play a central role in genetic expression and regulation, and are broadly classified into coding and non-coding RNA. Coding RNA, primarily messenger RNA (mRNA), serves as the template for protein synthesis by carrying genetic instructions from DNA to ribosomes. Non-coding RNAs (ncRNAs), on the other hand, do not code for proteins but perform crucial regulatory and structural functions. These include ribosomal RNA (rRNA) and transfer RNA (tRNA), essential for translation, as well as small interfering RNA (siRNA), microRNA (miRNA), and long non-coding RNA (lncRNA), which are involved in gene silencing, chromatin remodeling, and

post-transcriptional regulation[40, 41]. Many of these ncRNAs function in the cytosol, making them particularly accessible for therapeutic targeting through the delivery of exogenous RNA. This has been leveraged in RNA interference (RNAi) technology, where exogenous siRNA or double-stranded RNA (dsRNA) can trigger the degradation of specific mRNA targets, effectively silencing genes[42, 24]. In recent years, RNA-based therapeutics have revolutionized medicine beginning with the breakthrough SARS-CoV-2 mRNA vaccines, which spurred research of other RNA-based therapies, such as siRNA-based antiviral vaccines, treatment of genetic disorders, and cancer-targeting therapeutics[43, 44, 45, 46]. The ability to harness RNAi for gene-specific silencing offers immense potential for precision medicine and the development of RNA-based biopesticides to manage agricultural pests.

1.3.2 RNA Interference

An exciting alternative to chemical antifungals and insecticides is RNA-mediated gene silencing, also known as RNA interference. RNAi is a highly conserved eukaryotic pathway that results in the down-regulation or silencing of genes through one of three main pathways depending on the small RNA involved[47]. Endogenous RNAi pathways generally occur through the incorporation of miRNA or PIWI-interacting RNA (piRNA), which are responsible for post-transcriptional gene regulation or regulation of transposable elements within the germline, respectively[48]. While miRNA-mediated RNAi has been explored as a potential therapeutic, miRNAs are capable of targeting multiple genes, making them less suitable for specific targeting[49]. The siRNA pathway, depicted in **Figure 1.2**, is primarily activated as a result of detected exogenous dsRNA and is a primary antiviral response[49]. Additionally, unlike miRNAs, siRNAs are single-target, and thus can be designed to target a single gene in a pest with high specificity[49].

When exogenous dsRNA enters a cell, Dicer, a member of the ribonuclease (RNase) III family, binds and cleaves it into 19-25 nt siRNA fragments [50]. These short dsRNAs often

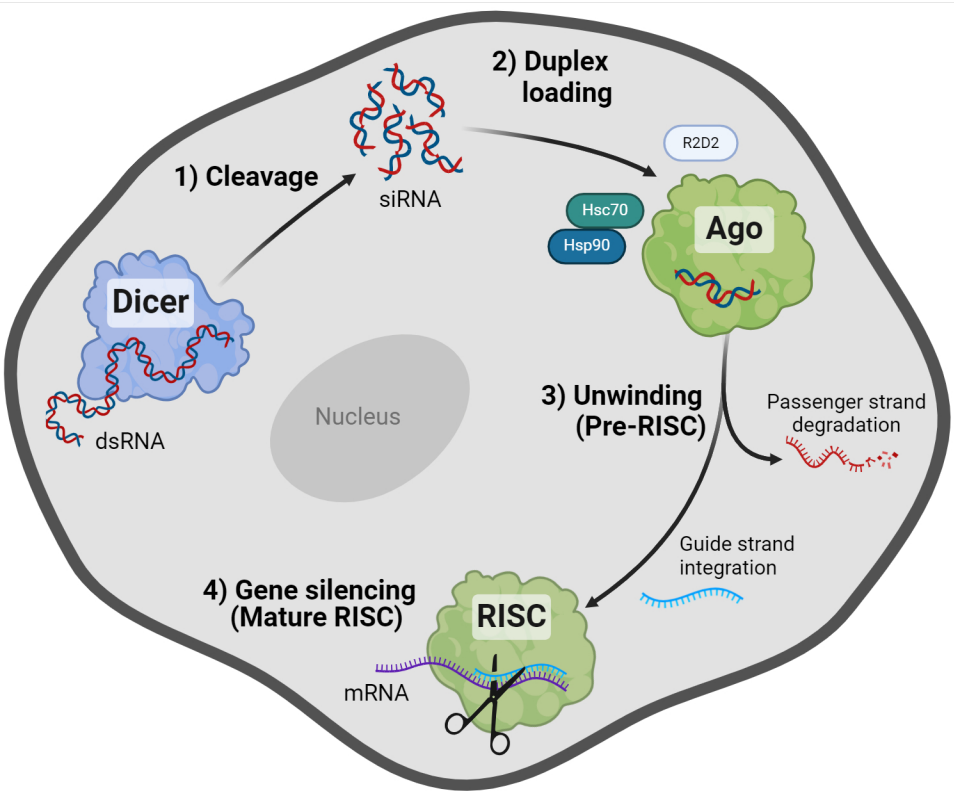

Figure 1.2: RNA interference pathway schematic. First, dsRNA is cleaved into siRNA fragments. The siRNA duplex is then loaded into Argonaute (AGO) with the help of R2D2, Hsc70/Hsp90, and other chaperone proteins, forming a precursor to the RNA-induced silencing complex (pre-RISC). After siRNA duplex unwinding, the guide strand is retained forming a mature RISC that is capable of mRNA binding, resulting in gene silencing.

feature TT or UU 3' overhangs that are recognized by RNAi machinery. The siRNA duplex is then loaded onto Argonaute.

Argonaute proteins are divided into two main subfamilies: PIWI, which interact with piRNAs in the germline, and AGO a ubiquitously expressed protein that can bind both siRNA and miRNA[48]. Duplex loading has been most fully understood in *Drosophila*. Liu et. al demonstrated that in duplex loading, the protein R2D2, which contains 2 RNA-binding domains, captures the most thermodynamically stable end of the siRNA, while Dicer binds the less stable end. While this thermodynamic instability creates a favorable, ATP-dependent reaction, Iwasaki et. al showed that depletion of ATP prevented loading[51]. Thus, ATP-dependent factors, namely heat shock cognate protein 70 (Hsc70), heat shock

protein 90 (Hsp90), and associate chaperone proteins, are needed to mediate the ATP-dependent conformational change of AGO to accommodate the duplex[51]. Studies in mouse embryonic fibroblasts indicate that in full Dicer knockout cell lines, Argonaute loading still occurs, suggesting only R2D2 may be essential for duplex loading in mammals[52], but no studies on Hsc70/Hsp90 machinery has been performed. Future work on this will provide key insight on the necessity of siRNA duplex loading in different organisms.

After loading, the two strands of the siRNA duplex are then unwound by AGO. In mammals, the strand with the more thermodynamically stable 5' end is favored as the guide strand, while the other strand, termed the 'passenger strand', is then degraded. While thermodynamics is a key factor of guide strand selection, other factors, such as the presence of specific dsRNA binding proteins and 5' nucleotide identity, also play a significant role[53]. The remaining AGO and siRNA guide strand complex form the mature RISC, and is ready for mRNA binding[52, 54].

Once assembled, the mature RISC binds mRNA transcripts complementary to the guide stand. Translation is then prevented by steric hinderance of translational machinery or mRNA hydrolysis. Studies in *Drosophila* suggest that endonucleolytic cleavage results in a free 3' and 5' end that are vulnerable to nuclease activity, however this mechanism is not fully understood and depends on the AGO protein [55].

Although RNAi is a promising alternative that uses innate cellular machinery to overcome resistance, one weakness of RNA-based treatments is the fragile nature of the RNA. For example, early degradation by nucleases and the inability to penetrate the cell membrane unaided both contribute to "dsRNA resistance"[56, 57]. Knockdown and silencing through RNAi has been documented in a wide variety of species, including insects and fungi[58, 59].

1.4 Delivery Strategies

The delivery of exogenous biological molecules (*e.g.*, RNAs, plasmids, proteins) into cells is a crucial part of the development of new therapeutics, alternative pesticide delivery

systems, and fundamental cell-based research. One of the first obstacles encountered when selecting or designing a delivery system is the protective barrier that surrounds the cell. While all cells have a plasma membrane, some cells, such as fungi, also feature a highly protective cell wall, a rigid defensive barrier that is difficult to penetrate and may require harsher treatment. However, no single method is suitable for all applications and it is important to select techniques suitable for the specific objectives of the research. For example, if only a small number of successfully transformed cells are needed, a method that prioritizes increased delivery over cell viability may be more appropriate. Thus, even the delivery technique itself is a variable. Delivery methods can be generally classified as chemical, biological, or physical:

- Biological methods - Biological delivery techniques utilize another 'body' to deliver cargo. Viral vectors are the most common biological delivery system, and are capable of crossing through cellular barriers to deliver nucleic acids into the cytosol. Depending on the objective, such as treating genetic disorders or infectious diseases, several viral vectors are available. For example, some viruses like adeno-associated viruses (AAVs) can be easily modified to deliver therapeutic nucleic acids to specific cells types without chromosomal integration[60]. Lentiviruses, on the other hand, are useful for stable, long-term expression due to chromosomal integration of their genome[61]. Other biological methods include utilizing transgenic organisms, often plants, to deliver a protein into a target organism. This is most clearly demonstrated in genetically modified plants that express *Bt* toxins for agricultural pest control. However, health risks (e.g., iummogenicity, genotoxicity, and insertional mutagenesis) and a growing hesitancy of the public to purchase genetically modified goods has increased the demand for non-biological gene delivery methodologies[61, 62, 63].

- Chemical methods - Chemical transfection reagents, such as calcium phosphate and cationic polymers, often take advantage of electrochemical interactions between the cargo and cell membrane. For example, calcium phosphate forms precipitates with

plasmid DNA that are readily internalized by cells, but have also shown high toxicity in some cell types[64]. Chemical methods may also utilize endocytosis or intracellular mechanisms to their advantage[65, 66, 67]. For example, linear polyethylenimine, is able to cause osmotic swelling to rupture endosomes, ultimately leading to the release of the nucleic acid it had condensed[68]. While chemical methods are generally the most simple and accessible for many applications, they are limited by factors such as stability in blood/serum, toxicity, and challenges related to solubility[69].

- Physical methods - Common physical delivery methods are able to utilize energy to permeate cell barriers through phenomena such as force, electricity, heat, light, or acoustic waves. physical methods are often used to deliver molecules into resilient cells, such as fungi, which may require more intense force. The increased intensity often results in low cell viability, but often only a single colony of successfully transformed cells is required. These high-intensity forces are useful for disrupting cell walls, but may be too intense for cells with only a plasma membrane[69]. For example, electroporation is one of the most common fungal transformation techniques, but is known to result in high cell death, and thus is not considered an idea method for mammalian cells[70, 71].

1.4.1 Nanoparticles as Delivery Enhancers

Nanoparticles (NPs) as delivery enhancers have been a major focus of nanotechnology research over the last decade. When designing any NP-mediated delivery system, key characteristics such as size, surface properties, drug loading/release have to be carefully considered in the context of system they will be applied in[72, 73, 74, 75]. NPs can also be be composed of numerous organic or inorganic materials. NP-mediated delivery of nucleic acids most commonly utilize lipids, peptides, or cationic polymers, or inorganic materials such as mesoporous silica, metal oxides, or gold[76]. This customizability can help protect delicate cargo, shield potentially immunogenic molecules, and enhance overall delivery rates, thus making NPs an attractive tool for enhanced biomolecule delivery.

Organic NPs are composed of of lipid- or polymer-based formulations and generally take advantage of the previously discussed chemical delivery mechanisms. Lipid-based NPs include liposomes, solid lipid nanoparticles, and lipid nanocarriers, and are the most commonly used non-viral nucleic acid delivery system due to their stability and ability to fuse with cellular membranes due to chemical similarities[76, 77]. Lipid-based NPs are the most used NP type in clinical trials and available treatments due to their high homogenicity, stability, and favorable pharmacokinetics[76]. Polymeric NPs are produced using natural polymers such as polyethyleneimene, poly(lactic-co-glycolic acid), chitosan, and others. Polymeric NPs are highly customizable and have high structural versatility. However, they are often highly cationic which may compromise cell viability, thus limiting their clinical application[78]. Peptide-based polymeric NPs, such as cell penetrating peptides, poly-L-lysine, and branched amphiphilic peptide capsules (BAPCs) are a relatively new class of NP that are highly promising as nucleic acid delivery tools due to low immuogenicity, high transfection rates, and customizable synthesis[79, 80]. Even many commercially available chemical methods are often organic NP-based, such liposomes (Invitrogen Lipofectamine™), cationic denrimers (PolyPlus jetPRIME®), PEI polymers (Polyplus jetPEI®), or lipid-polymer hybrids (Mirus *Trans*IT®).

Inorganic NPs, such as metal oxides and gold, can be used alone but are also often added to physical delivery methods[81]. For example, the superparamagnetic properties of iron oxide NPs (FE_2O_3 or Fe_3O_4) can be used to enhance thermal delivery[82]. Gold nanoparticles (AuNPs) have unique optical properties which make them ideal for NP-mediated photoporation, a physical technique that utilizes pulsed laser light that interacts with NPs to deliver exogenous molecules[83, 84]. The surface of AuNPs can also be easily functionalized to include moieties such as polyethylene glycol (PEG), peptides, and even nucleic acids[85, 86]. Unlike chemical methods, no new physical methods have been developed recently, despite their advantages in cells such as fungi that are not susceptible to many chemical methods.

1.5 Objectives

This work seeks to develop and optimize NP-mediated RNA delivery systems for dsRNA- or siRNA-mediated RNAi in yeast and insect systems. Both yeasts, such as *C. albicans* and insects like the fall armyworm are exhibiting increased biological resistance against current antifungal or pesticidal treatments, and RNAi presents a potential solution in both fields[22]. However, while NPs have been demonstrated to enhance delivery, NP-mediated systems are not a "one size fits all" solution, and the clear differences between insects and yeast necessitate different delivery strategies[87, 88]. As previously discussed, physical methods, such as photoporation, are ideal for penetrating rigid barriers such as the fungal cell wall, but are not ideal for insects due to the delicate nature of their cells and scaling limitations. On the other hand, delivery into insect cells requires exposing the organism to NP-containing media, thus making chemical delivery a more suitable method to protect and shuttle nucleic acids into and through cells. Additionally, chemical delivery more realistic for potential field applications as insects infest expansive fields. Combined, these considerations gave rise to the following objectives for each system:

- Design and optimization of AuNP-mediated photporation delivery for RNAi in *C. albicans*:

  In order to explore RNAi as an alternative antifungal, we aimed to create the first AuNP-mediated photoporation system for delivery in fungi. This was necessary as current fungal transformation methods are limited to the laboratory settings and greatly compromise cell viability, thus greatly limiting their clinical translation. While NP-mediated photoporation has been previously reported in mammalian cells, developing this method for fungal cells required extensive optimization of both laser- and nanoparticle-related experimental parameters, where the goal was to achieving high intracellular delivery while maintaining cell viability. The yeast model *Saccharomyces*

cerevisiae was chosen for initial optimization experiments due to its ease of manipulation and wealth of available knowledge, and Chinese hamster ovary (CHO) cells were used to understand how each condition may impact more delectate mammalian cells. However, *S. cerevisiae* lacks necessary RNAi machinery, so the ability of this method to deliver dsRNA or siRNA was demonstrated by silencing *EFG-1*, a key virulence gene, in *C. albicans*. First, delivery of fluorescently-tagged siRNA was use to compare delivery efficiency to the initial experiments in *S. cerevisiae* and confirm the ability to deliver RNA. Subsequently, quantification of transcript levels were used to compare knockdown efficiencies of siRNA and dsRNA. This served as both a way to establish AuNP-mediated photoporation as a successful RNA delivery method and as a comparison between siRNA and dsRNA silencing, something that has not yet been explored in fungal cells.

- Elucidation of cellular uptake, intracellular trafficking, and delivery efficiency of BAPC-dsRNA complexes for RNAi in *S. frugiperda* larvae

  While proof of concept experiments have established feeding BAPC-dsRNA complexes causes RNAi in insects, this project aimed to understand the mechanisms underlying BAPC internalization, intracellular fate, and movement through tissues in insects[59]. These factors were explored using the *S. frugiperda*-derived cell line Sf9. Following this, the impact of BAPC consumption on larval feeding behaviors was explored by feeding increasing concentration of BAPCs to second instar *S. frugiperda*. This provided a threshold at which BAPC concentration caused adverse effects to feeding behavior, thus establishing an efficient BAPC concentration for formation of BAPC-dsRNA complexes. Feeding *S. frugiperda* larva BAPCs complexed with dsRNA targeting subunits of the ubiquitous, essential enzyme vacuolar-type ATPase (V-ATPase) complexes was used to explore RNAi impact on larval survival, physiology, and gene transcript levels. The effect of feeding BAPC-dsRNA complexes on different diet substrates was also explored to determine larval food preference on survival.

Ultimately, this research creates new NP-mediated delivery platforms which enhance the potential applications of RNAi both in laboratory and applied sciences, thus contributing important knowledge about NP-mediated RNA delivery, RNAi as an alternative antifungal and bio-pesticide, and potential strategies to address the threat of biological resistance.

Chapter 2

Laser Assisted Delivery of Molecules in Fungal Cells

2.1 Introduction

Life-threatening fungal infections are an important cause of mortality worldwide in patients with compromised immune systems. Infections by fungal pathogens often require prolonged drug administration, which in turn can trigger adverse effects[89, 9, 8]. Currently, there are only three major classes of antifungals in clinical practice to treat this type of infection (amphotericin B, echinocandins, and azoles), and only one new class of antifungal drug has been developed in the last 30 years[89, 20, 77]. A limiting factor for the success of new antifungal therapies is the high impermeability of the rigid and thick fungal cell wall primarily composed of chitin, glucans, mannans, and glycoproteins[26]. As a result, nucleic acid-based therapies such as siRNA- and DNA-based drugs remain inefficient for the treatment of fungal infections[42]. These molecules have the potential to regulate gene expression of fungal vital genes and trigger cell death without affecting host cells and with low risk of developing resistance[42].

Current methods available to disrupt the cell wall, namely electroporation, biolistic bombardment, glass bead agitation, and monovalent cations, are restricted to in vitro applications due to the collateral damage that these techniques could cause to healthy living tissues[90, 91, 92, 93]. Consequently, antifungal delivery is still an ongoing subject of study as methods enabling transport of chemicals through the cell wall with improved efficiency, lower toxicity, and higher versatility are highly desirable[94].

With the development of femtosecond (fs) laser systems, a new class of drug delivery method is currently emerging. The high peak intensity associated to their extremely short pulse duration (1 fs = 10^{-15} s) enables the triggering of various direct and/or indirect transient biological and physical phenomena[88, 95]. For instance, fs lasers have been recently used to generate temporary openings in cell membranes, a process known as photoporation[88, 95, 96, 97]. There are few reports available that use this technology. The underlying mechanisms are still under debate and presumably encompass a variety of photothermal, photomechanical, and photochemical processes[88].

Although photoporation of living cells can be induced directly by a fs laser beam, recent findings have demonstrated that indirect effects, such as cavitation and shock waves generated by the interaction of the laser with nanoparticles, can significantly enhance the photoporation process[96]. Both approaches have been demonstrated exclusively in mammalian cells. The applicability of such a method for delivery of molecules in fungal cells still remains to be demonstrated. Mammalian cell membranes are composed of a single phospholipid bilayer that is known to be relatively easy to penetrate using chemical and physical methods[60, 98, 69]. On the contrary, fungal cells are more resilient to perturbations due to the presence of the cell wall in addition to the single phospholipid bilayer[26]. In fact, transfection reagents such as liposomes and polymers have proven to be inefficient, and, as mentioned before, physical methods such as electroporation usually compromise cell viability[91, 94]. In most cases, the cell wall has to be removed or treated with hypertonic solutions to make it more porous. These additional steps are time-consuming and unfeasible for medical applications[90, 99, 100].

The present investigation demonstrated the delivery of membrane-impermeable molecules (i.e., calcein and pDNA) into a fungal model organism, *Saccharomyces cerevisiae*. Although *S. cerevisiae* is innocuous, the majority of fungal infections in humans are caused by similar single-celled fungi (or yeast)[101]. In this study, gold nanoparticles (AuNPs) were irradiated with fs laser pulses to induce temporary openings in the fungal cell wall (**Figure 2.1**).

As a result, nearly 60% of the cells responded positively to the internalization of calcein, while cell integrity and viability remained almost intact during the process. In addition to the fluorescent dye calcein, delivery of pDNA for expression of green fluorescent protein (GFP) in *S. cerevisiae* mitochondria was also possible. After irradiation in the presence of the pYX142-mtGFP plasmid, successful transformation and generation of brightly fluorescent mitochondria in living yeast was achieved. Experimental methods that triggered pore formation in *S. cerevisiae* were also tested in animal cells (Chinese Hamster Ovary cells). Notably, viability was minimally affected by fluences lower than 2.8 mJ/cm^2, and cells were able to divide and proliferate after laser treatments.

AuNPs were synthesized through photoreduction using fs laser pulses as well. Such methodology enabled the elimination of reducing agents frequently used in conventional procedures to generate AuNPs. In this way, generation of oxidized products was avoided as such materials may exhibit cell toxicity or affect the stability of the AuNPs[102, 103]. Concerning fs lasers, phototoxicity is low in the near-infrared window (700-800 nm). In addition, compared with continuous wave lasers, ultrafast pulse radiation avoids environmental heating. This type of laser is currently being used in refractive eye surgery, and minimal collateral tissue damage is observed after irradiation[104].

These results might pave the way toward new treatments of fungal infections, particularly of the skin and oral and vaginal mucosa. This methodology could be adapted to clinical settings by adding topical aqueous solutions containing AuNPs and the antifungal agent to the affected area, followed by subsequent exposure to short laser pulses. The use of specific fungal drugs such as siRNA will allow to target and destroy exclusively fungal transcripts, limiting undesired effects on the mammalian cells.

2.2 Results and Discussion

Synthesis and Characterization of AuNPs. The strategy employed for the gold nanoparticle preparation involved reduction of Au(I) sodium thiosulfate employing fs laser pulses of

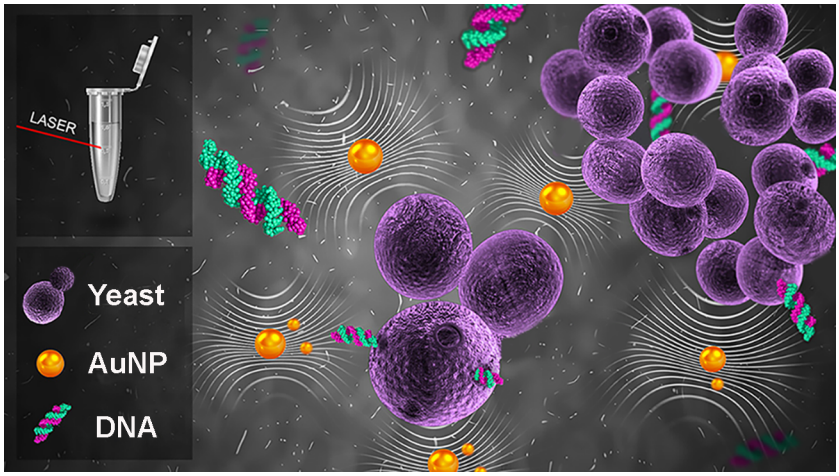

Figure 2.1: Schematic overview of the experimental protocol. *S. cerevisiae*, AuNPs, and DNA (or calcein) are placed in a phosphate-buffered saline solution. Subsequently, the solution is exposed to the radiation of a near-infrared fs laser. The interaction of the laser pulses with the nanoparticles induces cavitation and shock waves, which in turn induce transient pores in cell membranes.

800 nm photons in a way analogous to that reported earlier for $HAuCl_4$[105, 106]. Exposure of liquid water to very intense and short light pulses enabled laser-induced breakdown (LIB) of H_2O with generation of solvated electrons, e^-_{aq}, and hydroxyl radicals, •OH, according to[107] $H_2O + h\nu \rightarrow \bullet OH + H^+ + e^-_{aq}$. This process is somewhat akin to the transformation of water when exposed to high-energy radiation[106]. The strategy consisted of using e^-_{aq} to transform the Au(I) complex into metal particles. Such methodology enabled the elimination of reducing agents frequently used in conventional procedures to generate AuNPs. In this way, generation of oxidized products from the reductant was avoided as such materials may exhibit cell toxicity or affect the stability of the AuNPs. Furthermore, the Au(I) complex was selected instead of $AuCl^-_4$ because the former is currently used for treatment of arthritis, whereas the latter is a toxic chemical[108]. Sodium thiosulfate was the anticipated byproduct from the photoreaction, which is an FDA-approved compound free of toxic effects and currently used to treat cyanide poisoning and pityriasis versicolor[103]. The photoreduction was performed in the presence of poly-(ethylene glycol), PEG, known to function as an efficient stabilizer for AuNPs even in the presence of high phosphate concentrations[102]. PEG is a

biocompatible polymer employed in several medical and pharmaceutical applications[109]. Formation of AuNPs was anticipated to proceed according to the following sequence of steps:

$$AuL_2^{-3} + e_{aq}^- \rightarrow Au + 2L^{2-}$$

$$nAu \rightarrow Au_n$$

$$\bullet OH + RH_2 \rightarrow H_2O + \bullet RH$$

$$2\bullet RH \rightarrow HR\text{–}RH \text{ (polymer crosslinking)}$$

where AuL_2^{-3} = Au(I) thiosulfate complex, L^{-2} = thiosulfate ligand, Au_n = AuNP with agglomeration number n, RH_2 = PEG, and $\bullet$RH is the radical resulting from H atom abstraction from the polymer.

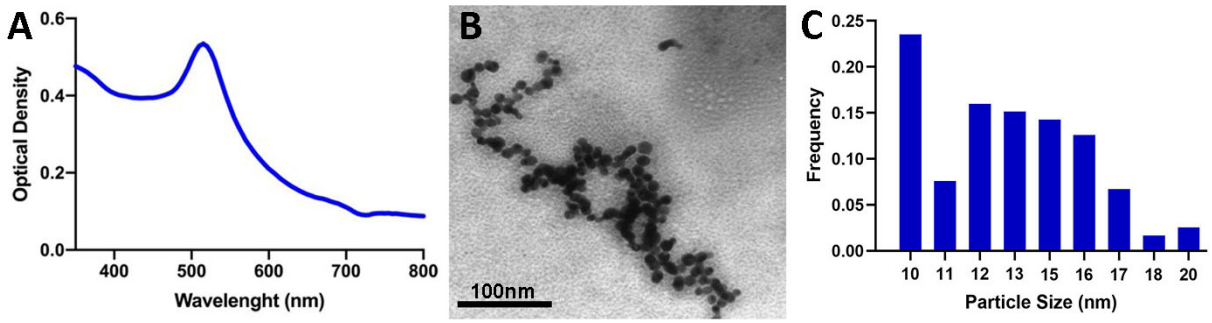

Figure 2.2: Characterization of aqueous colloidal dispersions of AuNPs: (A) spectrum from a Au colloid prepared by exposing a degassed solution containing 2×10^{-4} M Au(I) thiosulfate and 1×10^{-3} M PEG to fs pulses of 800 nm photons for 22 min, (B) TEM image of the photogenerated Au colloid, and (C) corresponding size histogram.

Exposure of degassed solutions containing Au(I) thiosulfate and PEG to the laser beam induced growth of a signal above 500 nm together with red coloration and simultaneous decrease of the optical signal at 300 nm of the Au(I) precursor. After photolysis for about 22 min, the 300 nm signal vanished and the intensity of the signal at longer wavelengths ceased to change. **Figure 2.2A** depicts a typical optical spectrum of the solution recorded after illumination featuring an absorption with a maximum at 515 nm corresponding to the surface plasmon resonance (SPR) signal typical of nm-sized spherical Au particles[110, 111]. The SPR signal is in good agreement with that centered at 518 nm of small colloidal

Au crystallites prepared via the thermal reduction of $AuCl_4^-$ induced by PEG at room temperature[102]. Efforts to reduce Au(I) sodium thiosulfate using PEG as a reducing agent failed even when the solutions were heated at about 90 °C. These results demonstrated that the strategy of utilizing the Au(I) compound to obtain AuNPs was successful only during exposure to intense fluxes of 800 nm photons.

Presented in **Figure 2.2B** is an image obtained from transmission electron microscopy (TEM) measurements revealing that the colloids consisted of nearly spherical metal crystallites. Diameters estimated from the longest particle dimension were the basis for the size histogram displayed in **Figure 2.2C**, which yielded a statistical average diameter (d_{av}) of 13 nm. This quantity is useful to evaluate the agglomeration number n corresponding to the average quantity of Au atoms present per particle. The evaluation employs $n = V_{particle}/V_{atom}$, where $V_{particle}$ is the average particle volume equal to $4/3\pi(d_{av}/2)^3$ and $V_{atom} = V_m/N_A$ is the atomic volume with V_m and N_A corresponding to the Au molar volume and Avogadro's number, respectively. Assuming that the density of the particles is equal to that of bulk Au, the calculation yields $n = 1 \times 10^5$ atoms per particle. To further evaluate particle size, we performed a dynamic light scattering (DLS) analysis of AuNPs in suspension.[112] The size distribution and statistical average diameter (11.5 nm) appeared to be in accordance with the results observed in TEM (**Figure A.1**).

As mentioned previously, the SPR signal of Au particles made photochemically is very similar to that of colloids prepared via reduction of $AuCl_4^-$ with PEG, which exhibited an extinction coefficient (ϵ) of about 3 x $10^3 M^{-1}cm^{-1}$[102]. Utilization of such ϵ value in conjunction with the absorbance at 518 nm (0.534) shown in **Figure 2.2A** resulted in a concentration of reduced Au(I) equal to 1.8×10^{-4} M, meaning that 90% of the precursor was transformed into metal. Estimation of the concentration of metal particles by means of n yielded 1.8 x 10^{-9} M or 1.1 x 10^{15} particles/L. The photochemical procedure generated highly stable colloids given that optical measurements failed to detect any particle precipitation for a

couple of weeks in the presence of air. Also, the colloids remained stable against precipitation after exposing them to solutions containing cells and their corresponding buffers.

2.2.1 Perforation of *S. cerevisiae* and Chinese Hamster Ovary Cells Exposed to fs Laser Irradiation in the Presence of AuNPs

Formation of transient pores in the cell wall was demonstrated via laser irradiation of *S. cerevisiae* in the presence of calcein and AuNPs. Calcein is a fluorescent dye unable to penetrate this cell type. However, after exposing cell suspensions to 800 nm fs laser for 10 min at 3.6 mJ/cm^2, up to 60% of the cells showed green fluorescence as a result of calcein passing through the transient breaks formed after the laser treatment (**Figure 2.3A**). Cell fluorescence due to calcein internalization was examined by flow cytometry; this is a rapid and reliable method to quantify fluorescence emission from single cells and viability (gating strategy is shown in (**Figure A.2**)[113, 114]. Dead cells are identified by the fluorochrome 7-AAD, which binds to the DNA of damaged cells. As a result, those cells emit fluorescence at 647 nm and are excluded from the analysis. Around 97% of cells were viable, meaning that viability was not significantly affected after the laser treatments. Confocal microscopy was used to corroborate the results obtained from flow cytometry by observing cellular morphology and green fluorescence of irradiated cells. According to **Figure 2.3C**, after laser treatment, no substantial damage was observed in the cell structure of *S. cerevisiae* and green fluorescence was observed in around 60% of the cells, which agrees with flow cytometry. All laser treatments and subsequent analysis were performed in the biological buffer PBS.

Exposure of *S. cerevisiae* to AuNPs and calcein in the absence of fs laser pulses led to insignificant perforation rates, ruling out the possibility that AuNPs alone promote the cellular internalization of calcein. Similarly, treatment of *S. cerevisiae* with only fs laser pulses failed to produce significant perforation (**Figure 2.3E**). Thus, the presence of both

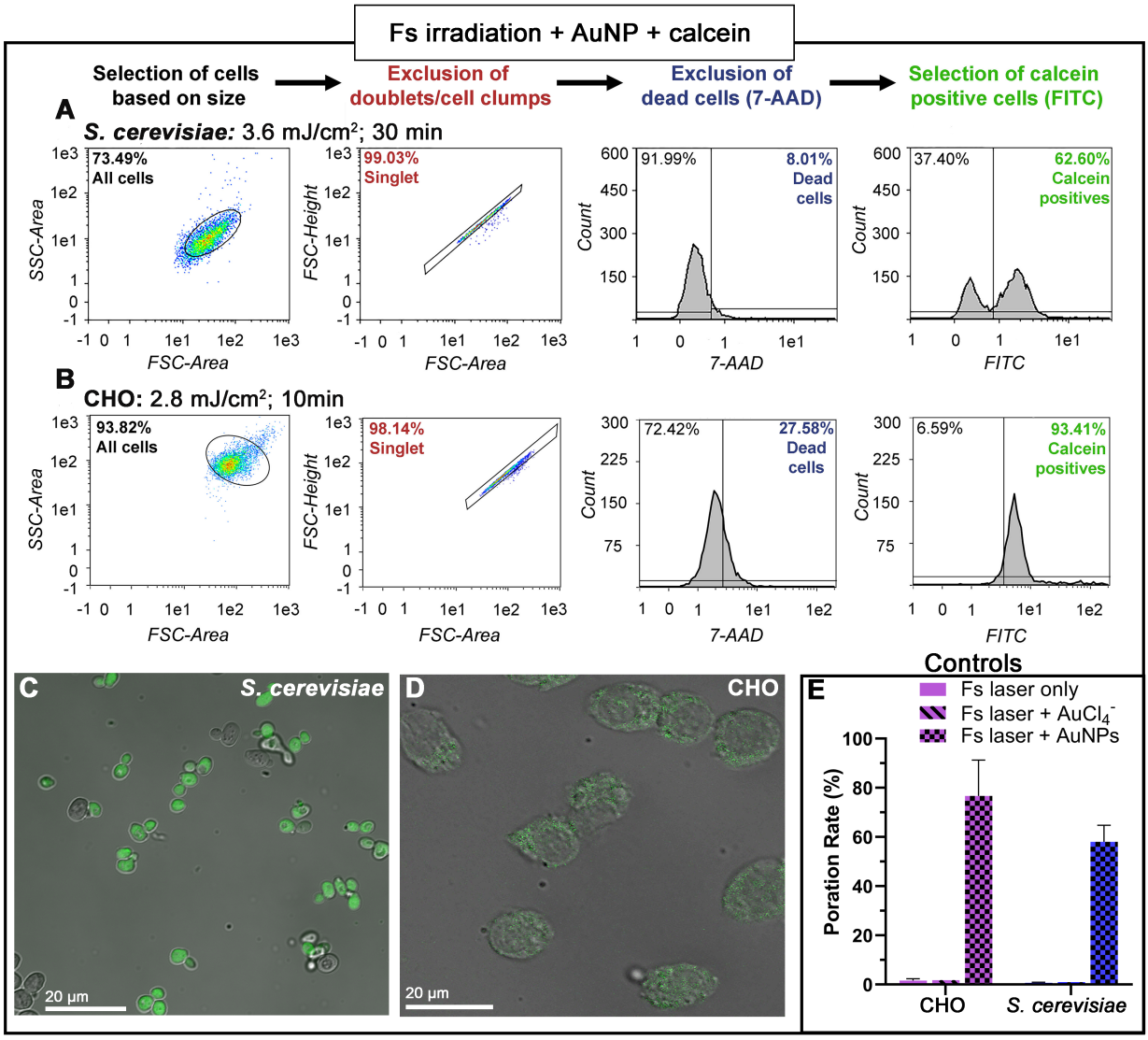

Figure 2.3: Exposure of *S. cerevisiae* and CHO cells to fs laser pulses in the presence of AuNPs and calcein. For this experiment, 1×10^7 *S. cerevisiae* cells/mL and 1×10^6 CHO cells/mL were suspended in phosphate-buffered saline solution and irradiated at 3.6 and 2.8 mJ/cm^2, respectively. Irradiation lasted 30 min for *S. cerevisiae* and 10 min for CHO. (A) Flow cytometry gating strategy for *S. cerevisiae*. In the first step, selection of cell size by plotting side scatter (SSC) versus forward scatter (FSC), then exclusion of cell clumps and doublets applying FSC-height vs FSC-area. Last two plots represent histograms to evaluate dead cells (7-AAD positive) and perforated cells (positive for calcein). (B) Same flow cytometry strategy applied for CHO cells. (C) Confocal microscopy analysis of *S. cerevisiae*. (D) Confocal microscopy analysis for CHO cells. (E) Exposure of *S. cerevisiae* and CHO cells to only fs laser pulses or fs pulses and AuNP precursor.

AuNPs and fs pulses seems to play a key role in the pore formation process. Most photoporation experiments have been performed with AuNPs exhibiting SPR signals that overlap (in resonance) with the incident laser radiation. Several mechanisms have been proposed to explain cell photoporation for those systems including: (a) thermal decompositions, (b) transformations due to cavitating bubbles, and (c) photochemical processes and/or attack by oxidizing free radicals[88]. In turn, cavitating bubbles are produced either thermally or when near-field enhancement effects generate a plasma. Participation of near-field enhancement effects have been proposed for AuNPs unable to absorb directly (off-resonance with) the laser photons. Yet both cavitating bubbles and plasmas can yield radicals as well as light able to initiate photoreactions. Not surprisingly, conclusive evidence for a specific mechanism has been elusive due to the complex nature of these reaction pathways and also because several of them may occur simultaneously. As the AuNPs used in the present study are off-resonance with the 800 nm photons, a plausible way to understand our results is if the metal crystallites experience localized heating due to multiphotonic absorption of the laser radiation. Cell perforation can then ensue in a way similar to the thermal processes thought to take place when photons are in resonance with the SPR signal[88].

However, an alternative rationalization assumes that the AuNPs undergo a LIB process akin to that of water[107]. LIB originates from multi-photonic absorption processes experienced by all materials; for H_2O, the breakdown is characterized by immediate plasma formation[115]. This event then leads to cavitating gas bubbles, which generate solvent radicals at longer times[105, 106, 107]. A key fact supporting such rationalization is that nanoparticles of numerous materials (Au, polystyrene (PS), SiO_2, Al_2O_3, etc.) suspended in H_2O experience LIB by the action of short laser pulses[78, 116]. Interestingly, the LIB thresholds for particles are significantly lower than that of H_2O. Also, LIB occurs for particles showing optical signals in resonance with the laser photons, as well as for those unable to absorb directly that radiation (off resonance). In the present system, the initial effect of the fs pulses for solutions free of particles was to yield LIB of H_2O, eventually forming AuNPs.

After particles are generated, the pulses induce LIB of the metal crystallites, but propagation of the resulting plasma into the surrounding solvent is expected to be fast through the solid-liquid interface. Consequently, the laser-induced particle breakdown is anticipated to produce transformations similar to those resulting from the LIB of the solvent. According to this scenario, the net effect of the AuNPs is equivalent to lowering the threshold for the water LIB.

Support for the involvement of LIB in membrane photoporation is provided by findings from investigations utilizing intentional breakdown of optically trapped PS and Au particles[117, 118]. Although direct absorption of the laser light occurred only for the metal particles, transfection of cells was achieved in both cases. Furthermore, unequivocal evidence was gathered that cavitating bubbles played a role in the transfection process. Involvement of LIB seems to be a general way to understand photoporation transformations obtained under a wide range of experimental conditions. In particular, such explanation constitutes an elegant way to rationalize the findings obtained in the present study but also the perforation results gathered with other materials (including carbon nanoparticles) unable to absorb directly the photon pulses[96, 119, 120].

The effect of laser irradiation was also investigated in cells without a cell wall. For this purpose, CHO cells, which are surrounded only by a single phospholipid bilayer, were subjected to the same experimental conditions used for *S. cerevisiae*. Hence, more effective photoporation was anticipated, and results confirmed such expectation, as perforation was around 2.5 times higher as compared to that of *S. cerevisiae* (**Figure 2.3 B,D**). Notably, CHO cells exposed to only fs laser pulses showed ∼10% of calcein uptake (**Figure 2.3E**). This supports the idea that during direct laser photoporation, LIB of water and photochemical processes can also take place without the need of nanoparticles to mediate those effects. Viability in CHO cells was slightly more impacted than *S. cerevisiae* potentially due to the formation of more transient pores that the cell was unable to seal. Despite this fact, around 70% remained alive for some fluences, which is comparable with viability rates reported for

CHO cells treated with common delivery vehicles such a liposomes or polymeric vesicles currently used in clinical trials[78, 121]. These observations are also consistent with previous photoporation treatments reported for mammalian cells in which under similar irradiation conditions, similar cell survival rates were obtained[96, 119, 122].

2.2.2 Effect of Laser Fluence and Irradiation Time on Perforation Rates in *S. cerevisiae* and CHO Cells

Effects of different laser parameters in photoporation such as fluence and irradiation time were investigated for both cell types. In the first set of experiments, *S. cerevisiae* and CHO were irradiated for 10 min at different fluences (0, 0.8, 2.0, 2.8, 3.6, and 4.4 mJ/cm^2). Perforation rates increased proportionally with the fluence. Similarly, when fluence was kept constant (3.6 mJ/cm^2) and time was modified (0, 5, 10, 20, and 30 min), perforation increased uniformly with longer irradiation times (**Figure 2.4A**). Adequate controls without fs laser pulses were performed to corroborate that AuNPs or calcein do not promote cell perforation under the conditions tested (**Figures A.3A,B** and **A.4**). For *S. cerevisiae*, comparation of calcein positive cells irradiated for 10 min at 4.4 mJ/cm^2 versus 20 min at 3.6 mJ/cm^2 showed no significant difference, meaning that similar efficiency can be achieved with shorter irradiation times by applying higher fluence. According to flow cytometry, viability in *S. cerevisiae* was not significantly affected in all conditions tested (**Figure 2.4B, left panel**).

The ability of *S. cerevisiae* to grow on solid medium after the irradiation process was also investigated qualitatively using the spotting test[123]. Exclusion of dead cells with 7-AAD provides a clear distinction between alive or dead cells and measures percent of these two categories[124]. However, the use of exclusion dyes does not provide information about the ability of yeast to divide. To demonstrate that *S. cerevisiae* can undergo division after laser treatment, irradiated cells were suspended in sterile water at different dilutions. Subsequently, samples were inoculated on solid medium, and colony growth was inspected after 48 h. The growth of colony-forming units at concentration of 1×10^7 and 1×10^6

cells/mL appeared to be consistent for all laser conditions, but minimal effects of laser treatments on cell division can be noticed at the lowest dilution (1×10^5 cells/mL) (**Figure 2.4C, left panel**). In the case of CHO cells, viability dropped more significantly with laser fluences higher than 2.8 mJ/cm^2 most likely due to the absence of the cell wall (**Figure 2.4C, right panel**). The ability of CHO cells to divide and grow after laser treatments was also tested. Similar to *S. cerevisiae*, growth was not greatly affected, and confluent cultures were observed after incubating cells for 48 h in supplemented media.

According to the data available in the literature, the present study is the first in which a systematic comparison of photoporation involving mammalian and fungal cells is presented. We demonstrated that perforation can be achieved in both cell types at fluences lower than 2.8 mJ/cm^2. Even though under these conditions, the percent of perforated *S. cerevisiae* is ∼30%, repeated treatments with nucleic acid drugs (i.e., RNAi, DNA) could trigger the desired killing effect. There is no known mechanism by which fungal cells could develop resistance against nucleic acids. Other physical methods, such as electroporation, can also create pores in fungal cells through the application of strong electric pulses. However, experimental conditions to achieve perforation would be too aggressive for skin cells, hampering clinical applications[9].

2.2.3 Delivery of Plasmid DNA in *S. cerevisiae* via Nanoparticle-Assisted Photoporation

In addition to the fluorescent dye calcein, plasmid DNA was also delivered via AuNP-assisted photoporation into *S. cerevisiae*. As mentioned before, nucleic acids such as double stranded RNA (dsRNA), antisense oligonucleotides, messenger RNA (mRNA), and pDNA have the potential of being useful as specific antifungal agents[125, 126, 58, 22]. Moreover, delivery of nucleic acids into fungal cells is also crucial for manipulating these organisms and advancing fungal-based biomedical and basic research[20]. Intracellular delivery of pDNA in *S. cerevisiae* was demonstrated by irradiating solutions of cells with fs laser

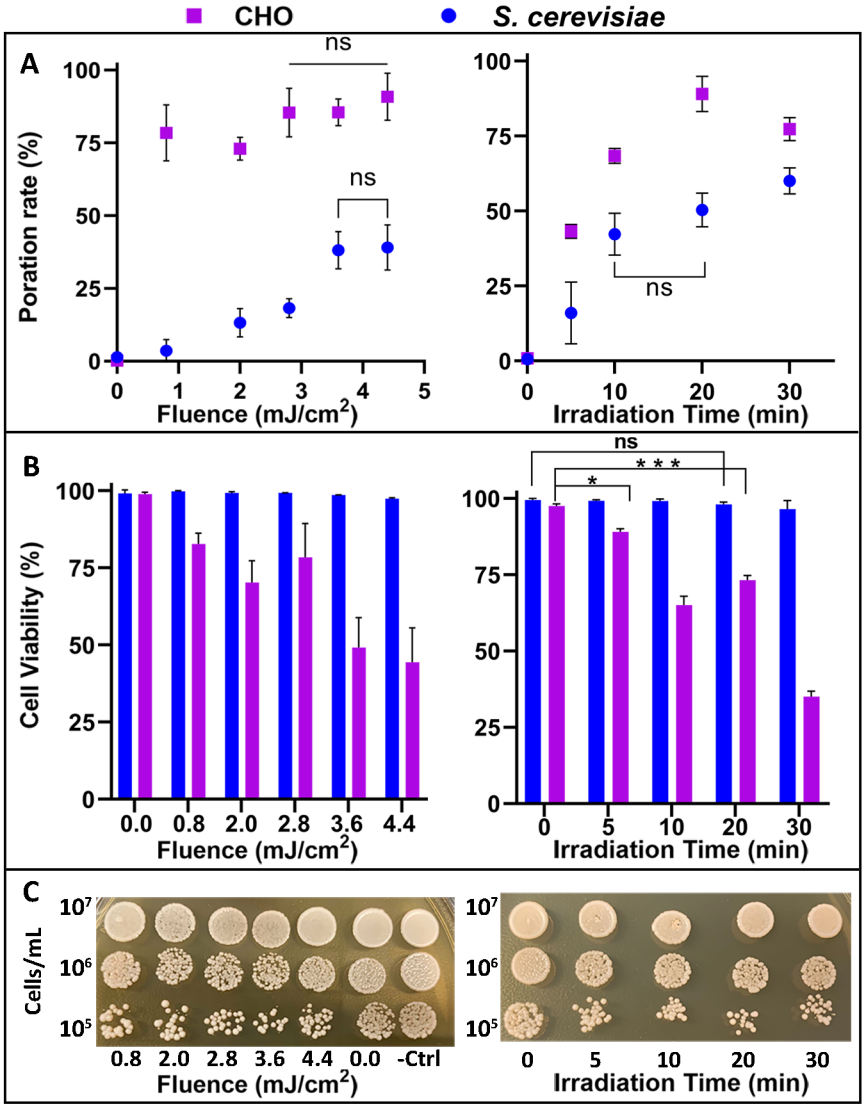

Figure 2.4: Effect of laser fluence and irradiation time in *S. cerevisiae* and CHO perforation. *S. cerevisiae* (1×10^7 cells/mL) or CHO (1×10^6 cells/mL) were suspended in a phosphate-buffered saline solution and exposed to fs laser pulses at different times and fluences in the presence of AuNPs (14 μM) and calcein (10 μM) (A) Irradiation for 10 min at different fluences (left plot) and irradiation at different times while maintaining the fluence at 3.6 mJ/cm^2 (right plot) (B) Viability analysis using the dead cell exclusion dye 7-AAD. The left plot shows irradiation for 10 min at different fluences and the right plot shows irradiation at different times while maintaining the fluence at 3.6 mJ/cm^2 (C) *S. cerevisiae* growth after irradiation treatments determined by the spotting test. Ctrl = untreated cells. Data represent mean values +SD of two experiments combined. Statistical significance: (*) $p < 0.033$; (***) $p < 0.001$; (ns) $p > 0.12$ versus control group or as indicated in the bars (ANOVA, Dunnett posttest).

pulses in the presence of AuNPs and fluorescently labeled pDNA (pDNA-BOBO-3 iodide). Cellular uptake of pDNA-BOBO-3 iodide was monitored qualitatively by fluorescence microscopy and quantified using flow cytometry. pDNA-BOBO-3 iodide was present in many cells (**Figure 2.5A,B**), and quantitative flow cytometry data (**Figure 2.5C**) shows that, relative to nonirradiated controls, nearly 30% were pDNA-BOBO-3 iodide positive. In non-irradiated controls, cells were not irradiated but were subjected to all other procedures, and non-significant uptake was detected (**Figures A.6** and **A.7**). Cell viability remained close to 100%. Concerning laser parameters, cells were treated with a laser fluence of 3.6 mJ/cm^2 and irradiation time of 10 min. These parameters were selected based on results obtained from calcein experiments.

To demonstrate that fs laser pulses do not cause detrimental damage to pDNA, a plasmid DNA (pYX142-mtGFP) designed to encode for GFP in mitochondria was also delivered into *S. cerevisiae*. Gene expression (transformation) was evaluated by growing irradiated leucine auxotrophic yeast at 30 °C on leucine-deficient media. The plasmid pYX142-mtGFP contains a LEU2 selective gene; thus, only cells that successfully maintain the plasmid can proliferate in leucine-deficient media[127]. Subsequent analysis of the transformed yeast by fluorescence microscopy indicated bright green fluorescence of the characteristic branched, tubular mitochondrial network below the cell cortex (**Figure 2.5D,E**). This shows that this method does not detrimentally damage the pDNA structure[90].

Other commonly used physical and chemical transformation methods, such as electroporation and protoplast transformation, subject cells to harsh experimental conditions that usually result in low viability or transformation rates. In an electroporation procedure, an electric field is applied to induce the formation of transient pores in the cell wall. However, before subjecting the cells to electric pulses, several steps are required to reduce leakage of intracellular material and prevent cell death, including placing cells in a hypertonic solution of 1 M sorbitol[42, 100]. A high number of cells is also needed due to the low survival rate

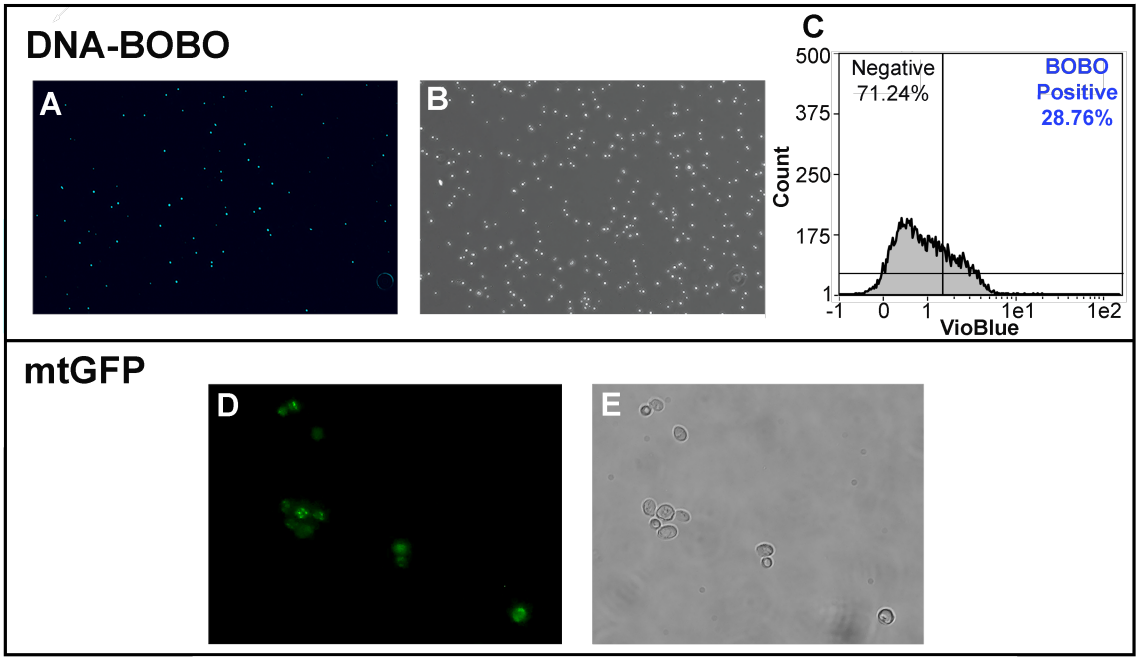

Figure 2.5: Fluorescence microscopy images of *S. cerevisiae* showing intracellular delivery of pDNA-BOBO-3 iodide and expression of mtGFP. (A) Fluorescence micrograph showing uptake of pDNA-BOBO-3 iodide and (B) bright-field micrograph to demonstrate integrity of the cells. (C) Flow cytometry analysis to quantify intracellular delivery of pDNA-BOBO-3 iodide. (D) mtGFP expression in *S. cerevisiae* grown in leucine-deficient media to mid-logarithmic growth phase and directly subjected to fluorescence and phase contrast microscopy, FITC filter, and (E) bright field.

after the procedure, which takes around 7 h. Another common method, protoplast transformation, consists of removing the cell wall via an enzymatic treatment to yield cells with a single phospholipid bilayer membrane. Subsequently, transfection reagents such as PEG and liposomes are used to deliver genetic material inside the cells[90, 58]. This method takes around 13 h to be completed, requiring a significant amount of effort because the components of the fungal cell wall are highly variable among different strains. Meticulous optimization is required for each species, and cell survival is highly compromised. AuNP-assisted photoporation is an alternative method to deliver genetic material into yeast that does not require extensive pre-sample preparation, is gentle with cells, and can be performed in less than 1 h.

2.2.4 Hyperspectral Microscopy Analysis of AuNPs in *S. cerevisiae*

As demonstrated in previous sections, photoporation in *S. cerevisiae* can be immensely enhanced by AuNPs. Phenomena such as LIB and multi-photonic absorption processes are believed to be boosted in the presence of the AuNPs[88, 96, 97]. However, mechanistic aspects such as the proximity needed between the nanoparticle and the cell membrane for these processes to take place remains largely unknown. Explanations proposed in prior studies assumed that adherence of the AuNPs to the cell surface was required to induce photoporation, but not much experimental evidence is available that can confirm this notion[88, 96, 97]. To gain an insight of how AuNPs co-localize inside the cells during irradiation, hyperspectral darkfield images were obtained from *S. cerevisiae* immediately after the laser treatment. This type of microscopy allows to visualize AuNPs by combining rapid optical observation and hyperspectral confirmation[128]. For this analysis, hyperspectral and darkfield images of the *S. cerevisiae* free of AuNPs (reference material) was collected and then compared with hyperspectral images of cells containing AuNPs; such comparison is shown in (**Figure 2.6A,B,C**). When AuNPs interact with cells, their physicochemical properties can be altered due to adsorption of proteins on the surface and agglomeration within cell vesicles or

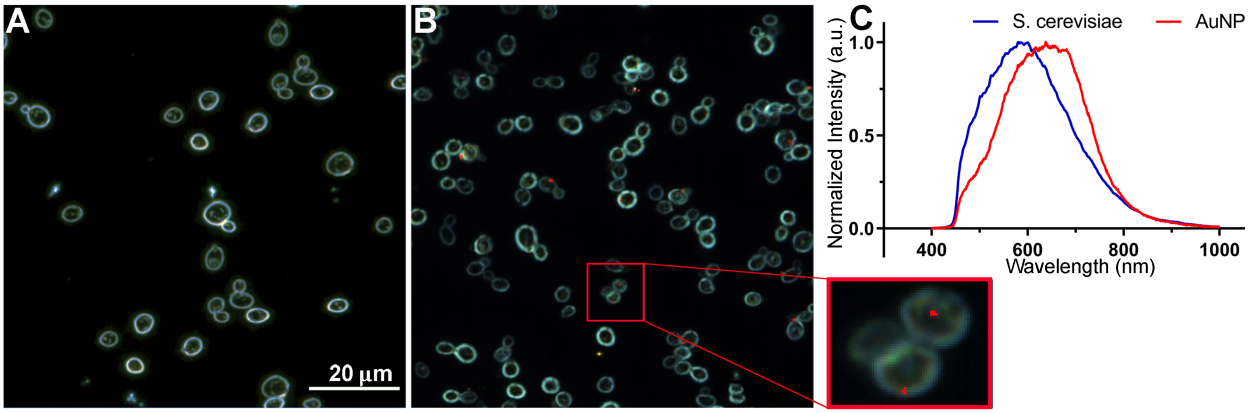

Figure 2.6: Hyperspectral imaging of *S. cerevisiae* exposed to fs laser pulses in the presence of AuNPs (14 μM), calcein (10 μM) and fs laser irradiation (3.6 mJ/cm^2). Images were acquired using CytoViva's patented enhanced darkfield optics at 100× magnification. (A) *S. cerevisiae* free of AuNPs (B) *S. cerevisiae* with AuNPs after laser treatment. (C) Spectral comparison of *S. cerevisiae* with (red) and without AuNPs (blue).

endocytic receptors. For instance, dimers or trimers of AuNPs can be formed inside endosomes. Thus, the spectrum presented in **Figure 2.6C** is red-shifted as compared to the spectrum of AuNPs acquired in water (**Figure 2.2A**) due to the modification of the NP environment[129, 130]. After analyzing ∼200 cells, results indicate that only around 20% of the cells showed AuNPs adhesion to cell walls or particles within the cytosol. In contrast, about 60% of the cells present in the sample exhibited photoporation. Hence, these data suggest that not all AuNPs need to adhere to the cell membrane or enter the cytosol in order to trigger pore formation. For instance, transient contacts between AuNPs and cells may suffice to induce this effect. Also, the LIB of water facilitated by the AuNPs probably occurs near the particle surface. Given that such energized region extends somewhat into the solution, particles located a few nanometers away from cells may also trigger photoporation.

2.3 Conclusions

The present study showed that laser-activated AuNPs can induce a reversible perforation of the *S. cerevisiae* cell wall. This action allows small molecules, such as calcein, and

relatively large molecules, such as pDNA, to be introduced into fungal cells. Until now, membrane breaks triggered by laser-activated nanoparticles had been demonstrated exclusively in mammalian cells which are relatively easy to penetrate because the cellular envelope is made only of a single phospholipid bilayer. However, yeast is surrounded by a thick cell wall made primarily of sugars, making delivery processes more challenging.

Although there are other physical methods available (such as electroporation) that can trigger breaks in the yeast cell wall, these methods generally compromise cell viability and require several preparative steps. More importantly, clinical applications to treat potential yeast infections in humans through electroporation have been hampered due to the aggressive nature of such approaches. Results in this study demonstrated that photoporation by means of 800 nm fs photon pulses is a somewhat milder method. The duration of the laser pulse is so brief that over-heating of the solution and surroundings is avoided. This novel method may also constitute an alternative tool for genetic transformation of yeast routinely used in research laboratories.

The synthesis method of the AuNPs solely involved the photoreduction of an FDA-approved precursor using fs laser pulses and removed the need of chemical reducing agents. It is also worth mentioning that using off-resonance pulses induces significantly less particle shape changes and fragmentation derived from extreme temperature increases resulting from resonant excitations[131, 132]. As a result, cell viability is often higher for off-resonance excitation[131]. In addition, to trigger perforation, AuNPs are needed in micromolar amounts (14 μM). Based on results obtained using hyperspectral imaging, only around 20% of cells showed AuNP adhesion to cell walls or nanoparticle uptake within the cytosol after irradiation at 3.6 mJ/cm^2 for 10 min. These data suggest that cellular internalization of AuNPs is minimal compared with perforation rates or calcein internalization.

Current methods to treat fungal infections of the skin are rather scarce. This approach might become an alternative to treat topical fungal infections because this technique will allow the entrance of novel and yeast-specific antifungal drugs such as dsRNA, mRNA, or

pDNA. Future studies will involve the use of differently shaped AuNPs with the aim of achieving higher perforation with less laser power.

2.4 Acknowledgments

We would like to thank Dr. P. Cobine for his guidance on how to grow and manipulate *S. cerevisiae*. We also thank Dr. M. Miller for his assistance with confocal microscopy and Stewart Mills for his help with hyperspectral microscopy. Finally, we would like to thank Grafika Labs for the design of Figure 2.1.

2.5 Materials and Methods

2.5.1 Materials and Cell Lines

Chinese hamster ovary (CHO) cells were purchased from American Type Culture Collection (Manassas, VA). As the fungal model, we used *S. cerevisiae* BY4741 (kindly provided by Dr. Paul Cobine, Auburn University, Auburn, AL)[127]. Cell culture media and supplements were obtained from Thermo Fisher Scientific (Manassas, VA), with the exception of peptone that was obtained from VWR (Radnor, PA) and non-essential amino acids MEM-NEAA that were obtained from Quality Biological (Gaithersburg, MD). The cell detachment reagent Accutase was acquired from Corning (Corning, NY), and the 7-aminoactinomycin dye (7-AAD) was from TONBO Biosciences (San Diego, CA). DNA plasmids pcDNA3-EGFP-5.2 kbp and pYX142-mtGFP-4.7 kbp were obtained from Addgene (Watertown, MA). Au(I) sodium thiosulfate, $Na_3Au(S_2O_3)_2$ was purchased from Alfa Aesar (Ward Hill, MA) and PEG with a molar mass of Mn = 8×10^3 g/mol was from Thermo Fisher Scientific (Manassas, VA). All remaining reagents were purchased from Millipore Sigma (St. Louis, MO) unless otherwise indicated. TEM formvar-coated Cu grids were obtained from electron microscopy sciences (cat # FCF330-Cu) and quartz spectrophotometer cells were from Starna Inc (Atascadero, CA).

2.5.2 Pre-Irradiation Preparation

Cell Cultures and Growth Conditions

Wild-type *S. cerevisiae* BY4741 were grown in YPD medium (10 g of yeast extract, 5 g of peptone, and 20 g of glucose per liter) at 30 °C[127]. CHO cells were cultured in Ham's F-12 Kaighn's Medium supplemented with 10% (v/v) fetal bovine serum and nonessential amino acids. CHO cells were passaged with Accutase every third to fourth day. A day before irradiation, an overnight culture of *S. cerevisiae* was inoculated into 3 mL of YPD at 1×10^7 cells per mL and grown at 30 °C with shaking (200 rpm) to an OD600 of 0.6. The cells were harvested at 3000 g for 10 min, and the pellet was resuspended in alkaline PBS at a final concentration of 1×10^7 cells per mL. CHO cells were seeded in 25 cm^2 cell culture flasks at a density of 1×10^5 cells per mL, and 24 h later or after cells reached 80% confluency, cells were detached and harvested at 1500 rpm for 5 min. The pellet was resuspended in PBS at a final concentration of 1×10^6 cells per mL.

AuNP Preparation

Solutions containing 2×10^{-4} M Au(I) $Na_3Au(S_2O_3)_2$ and 1×10^{-3} M PEG (in terms of monomer concentration) were placed inside 1 cm quartz cells and degassed with Ar for 20 min. The solutions were exposed to the laser radiation (power = 8.3 Watts) for five consecutive exposures of 1 min, followed by nine consecutive exposures of 2 min each. A dark time of about 3 min followed each exposure in which the progress of the particle formation process was monitored via spectrophotometric determinations. Solutions were prepared from water purified using a Millipore Milli-Q Biocell system; all glassware that contacted the Au colloids was cleaned with aqua regia.

AuNP Characterization

Spectral characterization of the Au colloids employed a Varian-Cary 50 Bio UV-vis instrument. Images of the Au particles were obtained via TEM on a Zeiss EM10 instrument operating at 60 kV. Samples for TEM analysis were prepared by placing a drop of a colloid diluted by a factor of 5 with H_2O on formvar-coated Cu grids. Size distributions of the nearly spherical Au particles were determined from about 200 individual particles present in the TEM images. AuNPs were diluted by a factor of 3 in sterile DDI H_2O. DLS was performed on nanoparticles in a 10 mm path length cuvettes (Sarstedt Standard Cuvettes) on a Zetasizer Nano ZSP (Malvern Instruments Ltd., Westborough, MA).

2.5.3 Cell Irradiation

For irradiation experiments, 1×10^7 (*S. cerevisiae*) or 1×10^6 (CHO cells) suspended in 1 mL of PBS were transferred into a 10 mm path, quartz spectrophotometer cell. Subsequently, AuNPs were added to the cell suspensions at a final concentration of 14 μM and, after a gentle mixing, the uptake marker calcein was added to the AuNPs-cell suspension at a final concentration of 10 μM. Samples were irradiated with a 11 W, 800 nm Ti:Sapphire fs instrument; fluence was controlled by varying the output power of the laser. This process was performed within less than 60 s of the final mixing of components (cells, AuNPs, and calcein) by placing the quartz cells in the path of the laser beam. A 20 cm convergent lens was placed in the beam path before the sample, and the sample itself was placed 10 cm away from focus (**Figure A.5**). At regular time interval (every 3 min), the laser was blocked and the solution was remixed. After the whole irradiation process was completed (5, 10, 20, or 30 min), cells were allowed to sit for 5 min at room temperature and then washed twice with PBS to remove any remaining fluorescent dye and AuNPs from the solution. For the intracellular delivery of DNA in *S. cerevisiae*, 10 μg of pYX142-mtGFP was added to the AuNPs-cell suspension[133]. Samples were irradiated at 3.6 mJ/cm^2 for 20 min following the same conditions used for calcein. The intracellular delivery of pcDNA3-EGFP labeled with

the fluorescent dye BOBO-3 iodide was tested following the conditions described for mtGFP and calcein. The labeling procedure was performed following the manufacturer's instructions (Thermo Fisher Scientific, Manassas, VA). All controls were subjected to similar conditions except exposure to fs laser pulses or addition of calcein, DNA, or AuNPs.

2.5.4 Post-Irradiation Analysis

Flow Cytometry Analysis

Upon irradiation, *S. cerevisiae* or CHO cells were suspended in PBS. 7-AAD was added to detect/exclude dead cells. A total of 10,000 cells per sample were analyzed using a MACSQuant Analyzer 10, Miltenyi Biotec. A 490 nm laser was used to excite calcein dye, and the emitted fluorescence was detected using a 515 nm filter. For DNA-BOBO-3 iodide, a 462 nm laser was used to excite the fluorescent material, and the emission was detected with a 481 nm filter. Cellular fragments and debris were excluded from the analysis by using a side-scatter versus forward-scatter detection procedure, and cellular clumps were excluded by using forward-scatter height versus forward-scatter area detection. Gating strategy for untreated cells is shown in A.2. Data were analyzed using Flowlogic (Miltenyi Biotec) software.

Cell Viability Determined by the Spotting Test in *S. cerevisiae*

S. cerevisiae was suspended in sterile water and diluted to give 10^7, 10^6, or 10^5 cells/mL. Samples (5 μL) of each suspension were inoculated on solid YPD medium and incubated at 30 °C. Colony growth was inspected after 48 h.

Cellular Uptake of AuNPs Using Darkfield Imaging

To analyze the intracellular uptake of AuNPs in *S. cerevisiae*, cells irradiated at 3.6 mJ/cm^2 for 10 min in the presence of calcein and AuNPs were washed three times with PBS. Next, cells were fixed in 3.7% formaldehyde at room temperature for 30 min, followed by

two PBS washings and analyzed using CytoViva's patented hyperspectral microscopy. The CytoViva system utilized Olympus microscope components (Tokyo, Japan) and is equipped with CytoViva's patented enhanced darkfield illumination condenser optics (US7,564,623, US7,542,203). Spectrally smooth illumination needed for hyperspectral imaging with the darkfield optics was provided by an aluminum halogen light source (Dolan Jenner, Boxborough, MA). The enhanced optics were designed to create high signal-to-noise darkfield optical images of samples such as yeast cells and nanoparticles. The microscope images were captured using a 100× oil iris objective with a variable numerical aperture of 0.6-1.3. The microscope was equipped with a 10 nm step translational stage (Prior Scientific, Cambridge, UK) which serves as a "push broom" mechanism for the line-scan hyperspectral image capture. A transmission diffraction grating hyperspectral imager, which acts as a prism, (Specim Spectral Imaging, Oulu, Finland) was used for spectral delineation. A CCD integrated into the spectrograph was used to capture the spectral data from the spectrograph. The system includes customized CytoViva ENVI 4.8 hyperspectral image capture and analysis software, which integrates all microscopy and hyperspectral image capture components. In addition to managing image capture, this software includes custom hyperspectral image analysis capabilities for pixel-level spectral characterization, comparison, and mapping of images.

Fluorescence Microscopy and Confocal Laser Scanning Microscopy

Images were obtained using a confocal LSM 700 laser scanning microscope (Carl Zeiss, Gottingen, Germany) and an Olympus IX73 fluorescent microscope with a DP74 camera (Tokyo, Japan).

2.5.5 Software and Statistical Analyses

Statistics were performed using GraphPad Prism 5 software (GraphPad Software, La Jolla, CA). A minimum of three replicates was performed for all conditions. Figures were created using Adobe Photoshop CC 2019.

Chapter 3

Optimization of AuNP-mediated Photoporation for Gene Knockdown in *Candida albicans*

3.1 Introduction

Candida, the leading cause of candidiasis worldwide, is a commensal, opportunistic pathogen that presents a significant threat to human health[27]. *Candida* species are among the most common fungal pathogens, responsible for a wide range of infections that affect both immunocompromised and healthy individuals[14]. These infections range from superficial mucosal diseases to life-threatening systemic infections, particularly in hospital settings. The increasing prevalence of antifungal resistance across multiple *Candida* species has made treatment more challenging, as many conventional therapies are losing efficacy. Addressing this challenge requires innovative approaches to developing alternative antifungal therapies, such as RNA-based strategies that can selectively silence essential fungal genes. However, the delivery of nucleic acids into fungal cells remains a significant obstacle due to the presence of a rigid cell wall that limits the uptake of exogenous molecules and the lack of research on clinically translatable fungal transformation methods[134, 135]. Overcoming these delivery challenges is critical for advancing RNA-based antifungal treatments and enhancing the efficacy of existing therapies.

The efficient intracellular delivery of therapeutic molecules remains a fundamental challenge in drug development[136]. Many treatments require direct access to the intracellular space, necessitating the circumvention of cellular barriers. In eukaryotic cells, the selectively permeable plasma membrane serves as the primary defense, whereas microorganisms, including fungi, possess an additional protective cell wall. This cell wall not only maintains structural integrity but also acts as a key interface with the environment and plays a critical

role in immune system interactions during infections[26]. Overcoming these barriers is particularly important in antifungal therapy. Current clinical treatments often require prolonged drug exposure, thus increasing the likelihood of drug resistance[137]. Furthermore, existing benchtop fungal transformation techniques are reagent-intensive, time-consuming, and often compromise cell viability, underscoring the need for more efficient delivery systems[91, 90].

Traditional fungal transformation methods, such as electroporation, have long been the cornerstone for introducing foreign molecules into fungal cells, yet their limitations become increasingly evident when applied to complex genetic manipulations[71]. Common fungal transformations rely on physical disruption techniques such as electroporation, heat shock, or biolistic bombardment to introduce exogenous cargo into cells[91]. However their limitations become increasingly evident when applied to complex genetic manipulations. For example, electroporation requires an additional enzymatic degradation of the cell wall to prime the cell for transformation by these methods, further compromising viability[100, 71].

The previous chapter established photoporation, a technique that utilizes femtosecond laser pulses in combination with gold nanoparticles (AuNPs) to generate transient pores in cellular barriers – as a viable method for the intracellular delivery of molecules into yeast. Photoporation offers a unique and promising approach to intracellular delivery by leveraging the photophysical and photochemical effects resulting from the interaction between ultrafast pulses and AuNPs. The exact role and contribution of these phenomena, largely believed to be laser-induced breakdown (LIB) and cavitation, is still an active area of research[122, 120, 83]. LIB occurs when the laser energy exceeds the dielectric breakdown threshold of the medium, resulting in the generation of plasma and high-energy shock waves capable of permeabilizing cell membranes[118]. This effect is amplified by the AuNPs, which concentrate the laser energy to localized regions. Additionally, cavitation – the rapid formation and collapse of vapor nanobubbles – generates shock waves and jets of air that transiently disrupt cellular barriers without compromising cell viability[138]. Importantly, photoporation enables the delivery of diverse molecular cargo, including nucleic acids and

potentially large CRISPR/Cas9 complexes[139]. This positions photoporation as a powerful alternative to traditional transformation techniques, particularly for species with robust cell walls such as *C. albicans*.

A critical application of novel intracellular delivery methods in fungi is RNA interference (RNAi), which has historically been challenging in *Candida albicans*[140, 135]. A recent discovery by Iracane et al. revealed that the reference strain SC5314, the most common reference strain used for studying genetic manipulations in *C. albicans*, contains a missense mutation (E361K) that results in a catalytically inactive Argonaute protein, a vital component of the RNA-induced silencing complex (RISC).[141, 142] This discovery has renewed the interest in harnessing RNAi for antifungal strategies in other *C. albicans* strains to better understand the potential of RNAi as an antifungal or genetic manipulation technique in this organism.

While the preliminary success of photoporation in *S. cerevisiae* has demonstrated its potential, further optimization is necessary to translate this technology to *C. albicans* and other pathogenic fungi. In this study, continued optimization of LAuNP-mediated photoporation in *S. cerevisiae* was accomplished by systematically varying nanoparticle size and concentration, as well as laser wavelength. The culmination of optimized laser parameters (laser fluence, irradiation time, and wavelength) and AuNP properties (size, shape, and concentration) were then used to deliver double-stranded RNA (dsRNA) and small interfering RNA (siRNA) into *C. albicans* strain 90028, a strain capable of RNAi. Successful RNA delivery was validated using flow cytometry and confocal microscopy of *C. albicans* photoporated in the presence of fluorescently-labeled dsRNA. Transcript levels were compared using the new, optimal conditions and conditions most similar to the previous work. This study continues the optimization of the photoporation method developed in the previous chapter through varying laser wavelength, AuNP size, and AuNP concentration. Subsequently, these conditions were used to deliver dsRNA and siRNA into *C. albicans*, resulting in the first delivery of RNA into yeast via photoporation. This insights into fungal gene

silencing and opening the door for AuNP-based photoporation as both a research tool and a potential clinical antifungal strategy.

3.2 Results and Discussion

3.2.1 Effect of Varying AuNP Size and Concentration on Poration Rates in *S. cerevisiae*

The impact of varying AuNP size and concentration on poration rates in *S. cerevisiae* was explored by irradiating *S. cerevisiae* exposed to the cell-impermeable dye 5(6)-carboxyrhodamine 110 hydrochloride (CR) using either 10, 20, or 50 nm AuNPs (**Figure 3.1**). *S. cerevisiae* was again selected as the model organism due to its well-characterized genetics, ease of manipulation, and similarity to other fungal species in terms of cell wall composition[143]. The effect of AuNP concentration was also explored in parallel by testing each AuNP size at one of three concentrations (C_1: $8x10^{10}$ AuNP/mL ; C_2: $4x10^{10}$ AuNP/mL; C_3: $8x10^9$ AuNP/mL). These concentrations were chosen as the concentration used in the previous work (C_1), this concentration halved (C_2), and one order of magnitude lower C_3). Flow cytometry was used to quantify alive, CR-positive cells viable, single cells that were successfully porated. Dead cells were excluded from analysis using the viability exclusion dye 7-actinomyocin D (7-AAD), which exclusively intercalates in GC-rich regions of DNA, resulting in a fluorescence signal at 647 nm. Analysis was done after allowing cells to recover for at least 5 min after photoporation. No 7-AAD should enter live cells as samples were allowed to recover at least 5 min post-irradiation and pores resulting from photoporation close within a few seconds.

Ideal parameters were defined as those that achieved high poration efficiency while minimizing cell viability loss. The only condition resulting in CR delivery significantly higher than the control (cells irradiated with only CR) was 50 nm AuNPs (**Figure 3.2A**). In agreement with previous studies, viability remained $\sim$ 65-100% (**Figure 3.2B**).Surprisingly, while both 10 nm and 20 nm conditions resulted in increased poration rates, these sizes also

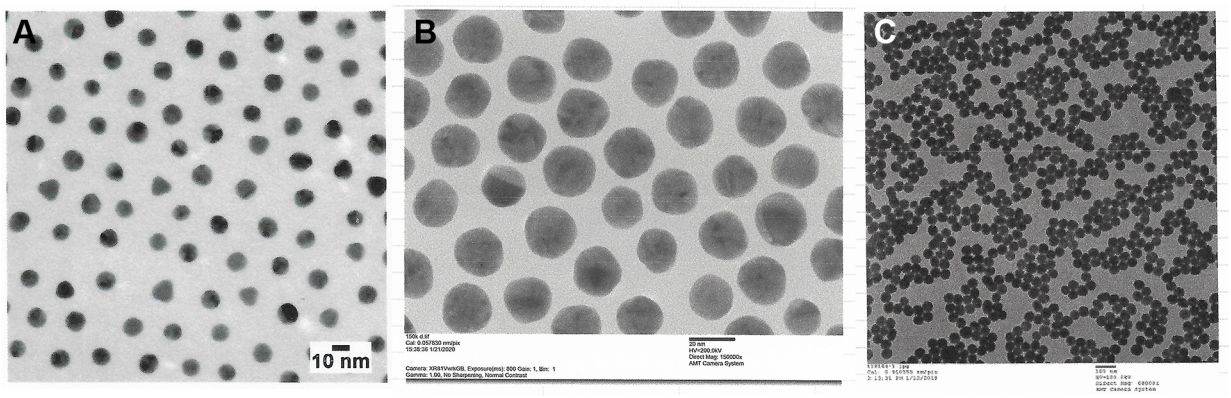

Figure 3.1: TEM micrographs of (A) 10 nm, (B) 20 nm, and (C) 50 nm. Scale bars represent 10 nm, 20 nm, and 100 nm, respectively.

provided inconsistent results, ranging from >5% to 50<% in most conditions. One potential explanation for this is that smaller nanoparticles (10 nm and 20 nm) may not absorb and convert laser energy as efficiently as 50 nm AuNPs, leading to inconsistent pore formation. Additionally, although previous results established only transient interactions are required for poration to occur, the distance between the smaller AuNPs and nearby cells may be too great for effects like cavitation or LIB to impact the cell wall[4]. The initial study utilized heterogeneous AuNPs ranging from 10 - 20 nm (8 x 10^{10} AuNP/mL), thus it is hypothesized that having multiple sizes in close proximity increased the efficiency of smaller sizes. In the 50 nm size group, C_2 resulted in the highest poration rate ($\sim$ 40%), and similar results were seen in the 10 nm size group, however the difference between the three concentrations was small. Interestingly, poration rates in the 20 nm group increased with decreasing AuNP concentration. Of all conditions, photoporation using 4x10^{10} AuNP/mL (C_2) of 50 nm AuNPs resulted in the most significant poration, thus making it the optimal combination of the explored variables.

Confocal microscopy was used to complement flow cytometry quantification, and in agreement with previous works, normal cell morphology and no fluorescent signal was seen in cells irradiated without CR dye (**Figure 3.2C**). Samples irradiated with 8x10^{10} AuNP/mL (C_1) of 10 nm are the most comparable to the previously used photosynthesized AuNPs,

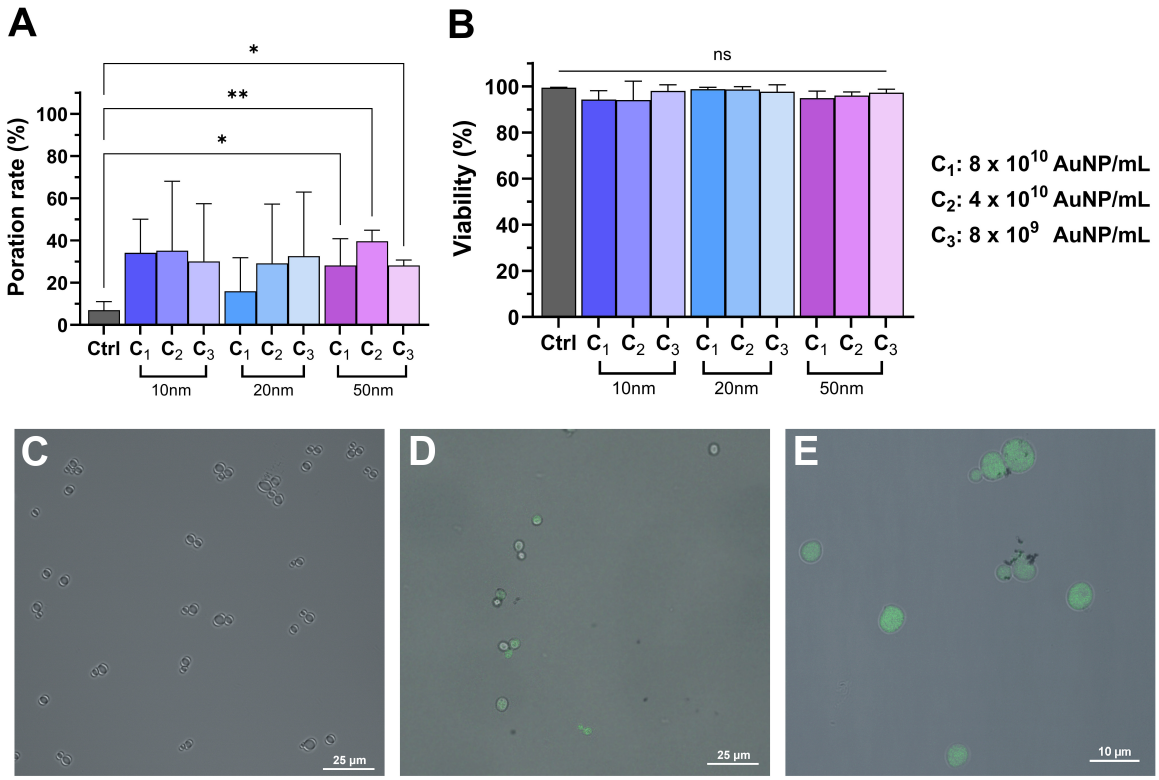

Figure 3.2: Effect of varying AuNP size and concentration on *S. cerevisiae* poration. *S. cerevisiae* (1x10^7 cells/mL) were suspended in PBS in the presence of CR (10 μM) and 10 (purple), 20 (blue), or 50 (pink) nm AuNPs at concentrations of 8x$10^1$0 (C_1), 4x10^{10} (C_2), or 8x10^9 (C_3) and irradiated for 10 min at 3.6 mj/cm^2. (A) Percent of porated live, single cells exposed to AuNPs and CR dye. (B) Viability analysis using the dead cell exclusion dye 7-AAD. (C) Confocal microscopy of *S. cerevisiae* cells irradiated without AuNPs, (D) 10 nm C_1 AuNPs and CR, and (E) 50 nm C_2 AuNPs and CR. Ctrl = Cells irradiated only without AuNPs. Data represent mean values +SD of at least three experiments combined. Statistical significance: (*) $p < 0.033$; (**) $p < 0.002$; (ns) $p > 0.12$ versus control group or as indicated in the bars (ANOVA, Dunnett posttest).

and were used as a comparison for the new condition. Congruent with flow cytometry, *S. cerevisiae* irradiated using C_1 10 nm (**Figure 3.2D**) showed fewer CR-positive cells compared to cells irradiated using C_2 50 nm conditions (**Figure 3.2E**). Of note, however, are the distinct dark clusters both surrounding and on cells in **Figure 3.2**. It is expected that these represent AuNPs or AuNP debris resulting from irradiation, as these clusters are seen in both 20 and 50 nm AuNPs. These sizes sediment with cells during centrifugation, even after numerous PBS washes, indicated by a red to pink tint of the pellet. As prolonged exposure to AuNPs themselves do, the remaining AuNPs likely have no significant impact on down-stream analysis. Lastly, it is also worth considering that 50 nm AuNPs have been documented to be readily internalized by HeLa cells[144]. While viability was not impacted, it underlines the importance of understanding how photoporation parameters impact mammalian cells for any potential clinical applications.

3.2.2 Impact of AuNP Shape on Poration and Viability

In order to understand how AuNP shape affected delivery rates, gold nanorods (AuNR) were also used to photoporate solutions of *S. cerevisiae* exposed to CR dye. Compared to nanospheres, AuNRs differ significantly in their physical and optical properties, largely due to geometry considerations. Nanospheres are generally symmetrical, thus resorting in a single absorbance peak (**Figure 3.4A**), also known as a surface plasmon resonance (SPR) peak, and high local-field enhancement in parallel to the incident wave (**Figure 3.4B**)[120]. In contrast, AuNRs are anisotropic, possessing both a longitudinal (length) and a transverse (diameter) axis, which gives rise to two distinct SPR peaks: one in the visible range (transverse) and another in the near-infrared range (longitudinal) (**Figure 3.4C**). [145] The resulting local field enhancement changes drastically depending which axis the incident electromagnetic wave travels, with the strongest enhancement occurring along the longitudinal axis (**Figure 3.4D**). This tunability allows AuNRs to interact more effectively with NIR light, making

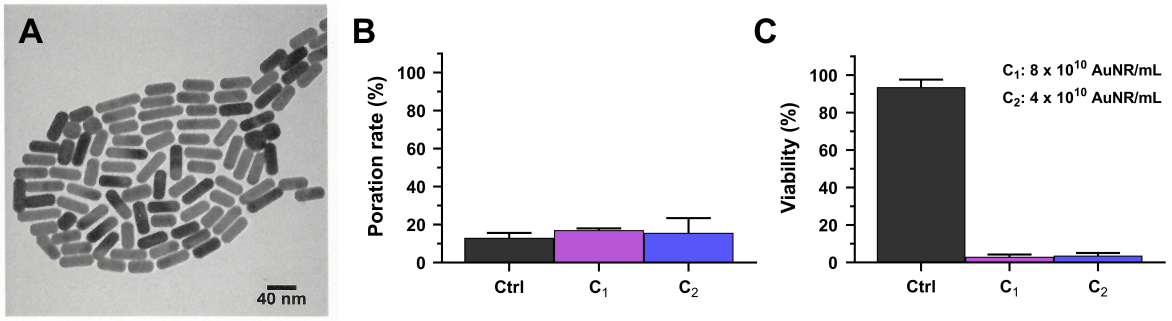

Figure 3.3: Irradiation of *S. cerevisiae* in the presence of 10 μM CR using 40±15 x 15±5 nm AuNRs at concentrations of 8x10^{1}0 (C_1) or 4x10^{10} (C_2) AuNR/mL. (A) TEM micrograph of AuNR. (B) Percent of porated live, single cells exposed to AuNPs and CR dye. (C) Viability analysis using the dead cell exclusion dye 7-AAD. Ctrl = Cells irradiated only without AuNPs. Data represent mean values +SD of at least three experiments combined.

them particularly useful in biomedical applications such as photothermal therapy and deep-tissue imaging.[146, 147, 148] Consequently, altering AuNR dimensions, and thus the aspect ratio (length:diameter), of AuNRs shifts the SPR peaks, creating another avenue for NP customization.

For this experiment, 40±15 x 15±5 nm AuNRs with the primary SPR peak at 660 nm were used (**Figure 3.3A**). AuNRs were added at either the optimal concentration from experiments using nanospheres (4 x 10^{10} AuNR/mL) and the concentration from the initial optimization work (8x10^{10} AuNR/mL) were compared. Both conditions resulted in poration similar to that of controls irradiated without AuNRs (<∼20%) (**Figure 3.3A**). Additionally, cell viability was extremely compromised (**Figure 3.3B**), and solutions post-irradiation were noticeably hot to the touch. The unsymmetrical geometry of AuNRs influences energy absorption and heat generation, with nanorods generally producing stronger localized heating effects than nanospheres under laser irradiation[4]. Combined, these factors clearly indicate that a re-optimization of parameters would be required for use of different AuNP shapes, which, while not the goal of the current study, opens an intriguing new pathway of research into AuNP-mediated photoporation.

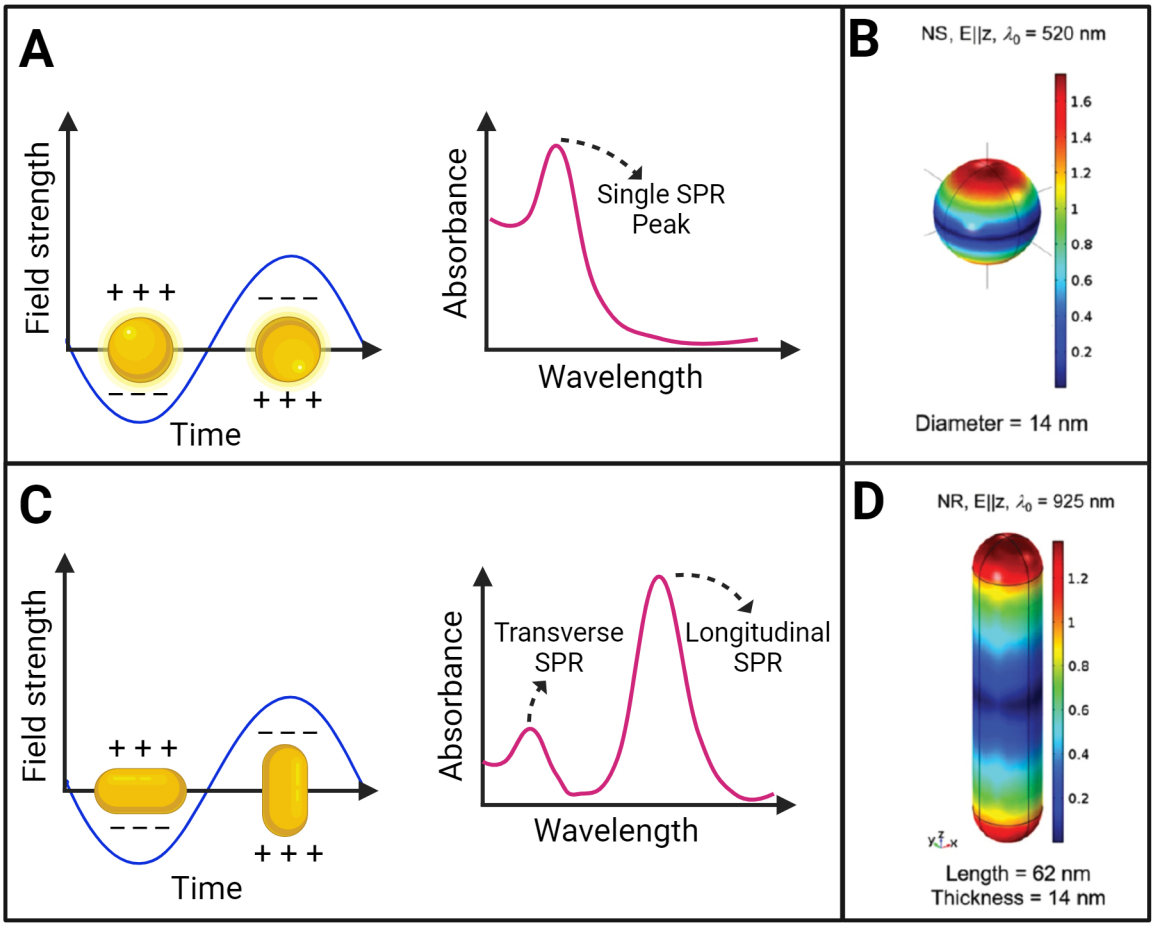

Figure 3.4: (A) Schematic of plasmon oscillation and absorbance spectra of AuNPs interacting with an electromagnetic wave. (B) Example local-field enhancement maps calculated for an Au nanosphere (NS) irradiated with the wavelength of maximum SPR intensity (C) Schematic of plasmon oscillation and absorbance spectra of AuNR and resulting the transverse and longitudinal SPR peaks. (D) Example local-field enhancement maps calculated for Au nanorod (NR) irradiated with the wavelength of maximum SPR intensity. B and D reproduced and adapted with permission from Ref. [4] with permission.

3.2.3 Effect of Frequency Doubling on Poration Rates in *S. cerevisiae*

The effect of irradiating samples with frequency-doubled photons (400 nm) was explored by placing a beta barium borate frequency-doubling crystal in the laser path. This second harmonic generation process resulted in a population of 400 nm photons, which, though comprising only ∼10% of the incident beam, carried sufficient energy to significantly impact delivery efficiency. Cellular exposure to 400 nm light, which lies in the violet to near-ultraviolet spectrum, is known to be biologically hazardous, due to higher photon energy and strong absorption by several biological molecules, potentially causing increased DNA damage, protein oxidation, and membrane disruption[149]. In contrast, 800 nm light, which is in the near-infrared (NIR) region, is considered biologically friendly and is widely used in biomedical applications as NIR light falls within the "optical therapeutic window" (650–1350 nm), where absorption by biomolecules, such as proteins and nucleic acids, is minimized, thus enabling deeper tissue penetration while reducing unwanted phototoxic effects[150, 120]. Thus, while it was expected that irradiation at 400 nm would result in decreased viability, the effect of combining high-energy photons and AuNPs on delivery rates was still of interest.

Control samples containing only *S. cerevisiae* cells and dye (no AuNPs) exhibited a poration rate of $/sim$ 70%, significantly higher than the <20% observed in 800 nm irradiation controls. Similarly, poration rates in AuNP-containing samples were also increased under 400 nm conditions, but no significant difference in poration efficiency was detected between AuNP-treated and no-AuNP control samples (**3.5A**). Despite prior observations that AuNPs enhance membrane permeability at longer wavelengths, their presence under 400 nm irradiation did not lead to additional increases in poration efficiency. This may suggest that LIB, cavitation, or plasmonic resonance effects at this wavelength do not sufficiently enhance local photothermal or photomechanical effects over potential photon-induced membrane damage[151, 149].

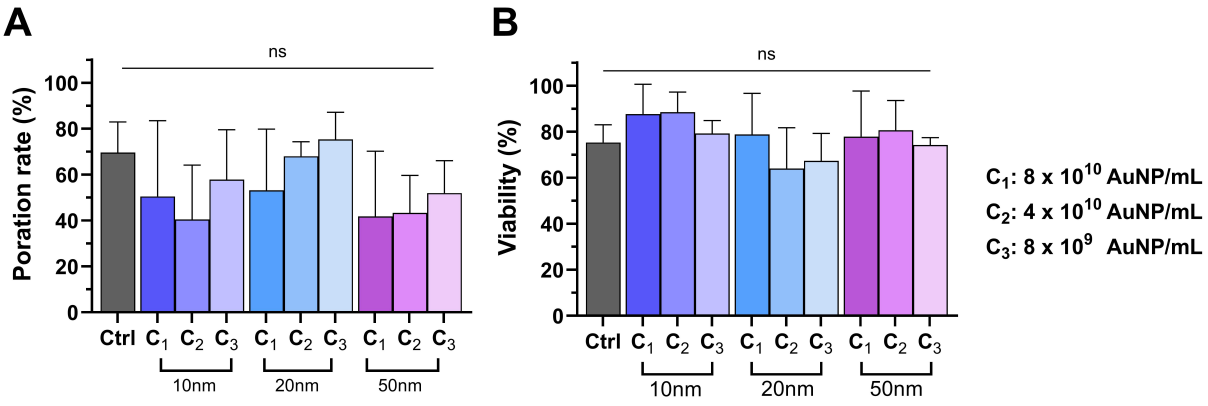

Figure 3.5: Effect of 400 nm photons on poration of *S. cerevisiae*. Solutions of *S. cerevisiae* (1 x 10^7 cells/mL) were suspended in PBS and exposed to 400 nm fs laser pulses resulting from a frequency doubling crystal in the path of an 800 nm fs pulse beam. Either 10 (purple), 20 (blue), or 50 (pink) nm AuNPs were added at one of three concentrations. Ctrl = Cells irradiated only without AuNPs. Data represent mean values +SD of at least three experiments combined. Statistical significance: (ns) $p > 0.12$ versus control group (ANOVA, Dunnett posttest).

Cell viability was $< 80\%$ in control samples and decreased across all conditions exposed to 400 nm photons compared to 800 nm. However, viability levels remained statistically indistinguishable between AuNP-containing and no-AuNP conditions (**3.5B**), suggesting that cell death primarily results from the population of higher-energy 400 nm photons rather than nanoparticle-mediated effects. This observation supports the hypothesis that multiphoton absorption or enhanced photochemical interactions at shorter wavelengths contribute to increased membrane disruption, which may require further investigation to optimize delivery efficiency while minimizing cytotoxicity. Additionally, while 400 nm photons are not suitable for photoporation aimed at a clinical application, the enhanced delivery without AuNPs presents yet another avenue of research for new delivery methods or applications that may require no AuNP component.

3.2.4 Delivery of fluorescent labeled dsRNA and siRNA into *Candida albicans*

After optimizing photoporation parameters, the next major objective of this study was to validate the effectiveness of this delivery system in the clinically relevant fungal pathogen *C. albicans*. Since the initial optimization was performed using a small fluorescent dye, fluorescently labeled siRNA was delivered to: (1) confirm that the method achieved comparable delivery efficiency in *C. albicans* and (2) assess whether RNA, a larger and less stable molecule, could be effectively delivered.

To accomplish this, the 5' ends of siRNA (25 bp) were labeled with ATTO488 maleimide ($\lambda_{abs/em}$ = 500/520 nm) or ATTO550 maleimide ($\lambda_{abs/em}$ = 554/576 nm) for flow cytometry and confocal microscopy analysis, respectively. Photoporation was performed using 10 nm (C_1) (**Figure 3.6 A**) and 50 nm (C_2) AuNPs. Microscopy of photoporated samples showed distinct intracellular fluorescence (**Figure 3.6 B**), confirming successful siRNA internalization, while cell morphology remained unaffected, corroborating previous findings in *S. cerevisiae*. In contrast, control samples photoporated in the presence of ATTO-siRNA but not AuNPs resulted in very little poration, similarly to samples porated with CR dye (**Figure 3.6 C**).

Flow cytometry was used to quantitatively compare siRNA delivery across different AuNP conditions. Photoporation using 10 nm (C_1) or 50 nm (C_2) for siRNA delivery rates averaged ∼56% and ∼96%, respectively, which are both approximately three times higher than the poration rate observed for CR dye (**Figure 3.6 D**). This supports the theory that molecular delivery is concentration-dependent, as 10 μM CR dye (4.7 ng/μL) corresponds to roughly one-third of the siRNA concentration (15 ng/μL). Additionally, viability was decreases in both samples, suggesting *C. albicans* may be more sensitive to poration than *S. cerevisiae* (**Figure A.8**). These findings confirm that photoporation enables efficient, high-yield RNA delivery in *C. albicans*, an important consideration for understanding and potentially troubleshooting gene silencing.

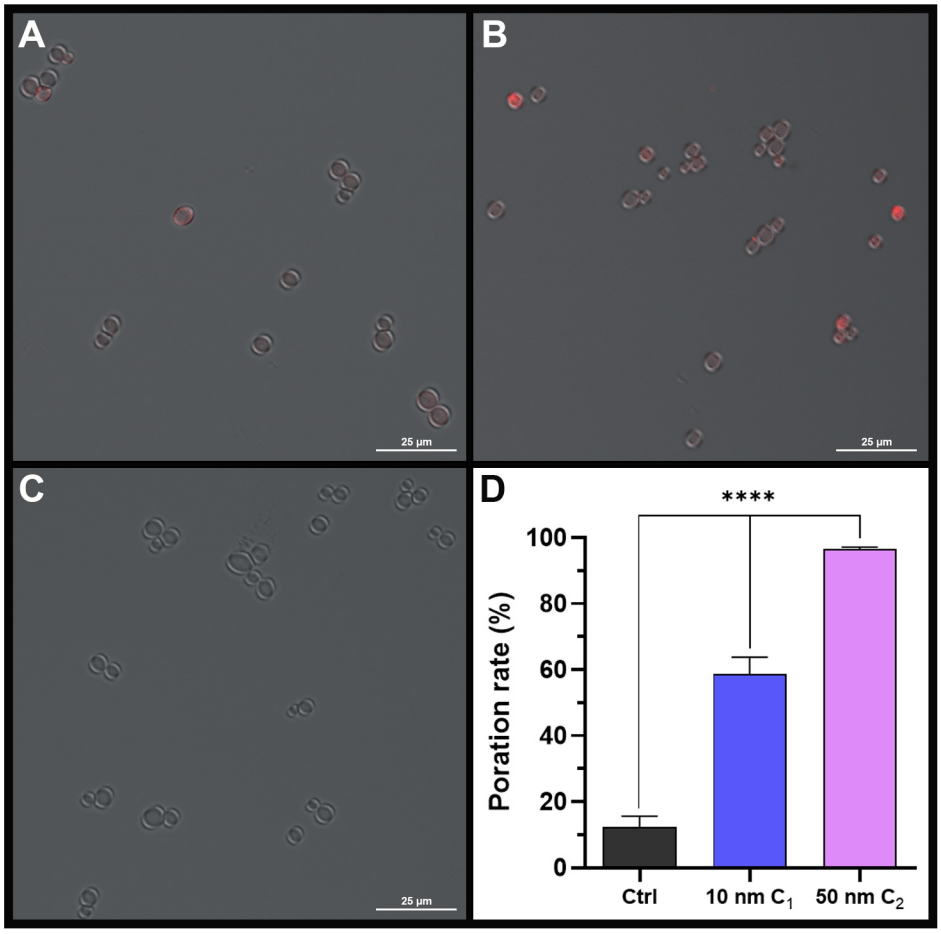

Figure 3.6: Delivery of ATTO-siRNA into *C. albicans*. Solutions of *C. albicans* (1 x 10^7 cells/mL) were suspended in PBS and photoporated in the presence of 15 ng/μL of 25 bp siRNA labeled with ATTO dye on the 5' ends, followed by immediate analysis. Confocal microscopy analysis of samples irradiated with (A) 10 nm (C_1), (B) 50 nm (C_2) AuNPs, or (C) no AuNPs in the presence of ATTO550-siRNA. (D) Flow cytometry quantification of ATTO488-siRNA uptake. Ctrl = cells irradiated without AuNPs. Data represent mean values +SD of three experiments combined. Statistical significance: (****) $p < 0.0001$ versus control group or as indicated in the bars (ANOVA, Dunnett posttest).

3.2.5 Validation of Gene Knockdown in *Candida albicans*

Validation of gene knockdown was assessed through the delivery of siRNA targeting Enhanced Filamentous Growth Factor 1 (EFG1), a key regulator of filamentous growth in *C. albicans*[152]. As previously mentioned, RNA delivery activates the RNAi pathway, a mechanism this work is exploring as a potential antifungal alternative. Until recently, RNAi in *C. albicans* was largely considered ineffective due to a missense mutation (E361K) in AGO1, the gene encoding the Argonaute protein – an essential component of RISC. This mutation is present in strain SC5314, the most commonly used strain for genetic manipulation[142]. This was also observed through the lack of silencing in several initial experiments we performed using this strain. However, recent findings by Iracane et al. revealing this mutation also established that wild-type strains lacking this mutation retain functional RNAi machinery[142]. Thus, to ensure efficient gene silencing, another wild-type strain (ATCC 90028) was selected, and sequence alignment using the NCBI BLAST tool confirmed the absence of the AGO1 E361K mutation.

EFG1 encodes a transcriptional regulator required for the dimorphic transition from yeast to hyphal form, a morphological switch critical for pathogenicity. The hyphal state enhances interactions with host cells, promotes biofilm formation, and facilitates tissue invasion, making EFG1 an attractive target for antifungal intervention[140]. As EFG1 expression is induced under host-like conditions, such as the presence of serum, elevated temperature (37°C), and elevated CO_2, we optimized conditions to activate EFG1 expression prior to gene knockdown analysis[152]. Specifically, cells were cultured in YPD medium supplemented with 50% adult bovine serum at 37 °C, which mimics host conditions, for 12 hours post-irradiation to induce hyphal transition.

To assess RNAi efficiency, real-time quantitative reverse transcription PCR (RT-qPCR) was used to measure the log-fold change in EFG1 mRNA levels relative to non-stimulated logarithmic-phase yeast. ACTB (β-actin) was used as a reference gene for normalization through $\Delta\Delta C_t$ analysis[153]. Photoporation of *C. albicans* exposed to 15 μg dsRNA (15

ng/μl) resulted in a non-significant reduction in EFG1 expression using either 10 or 50 nm AuNPs (**Figure 3.7 A**). In contrast, photoporation using 10 nm (C_1) AuNPs resulted in significant silencing(**Figure 3.7 B**), potential evidence that delivery of siRNA, thus bypassing the cleavage of dsRNA by Dicer, may be more efficient for RNAi applications. Unfortunately, an equipment malfunction occurred prior photoporating *C. albicans* in the presence of siRNA and 50 nm AuNPs, thus this data is unavailable for comparison(**Figure 3.7 B**). Several controls were included to validate these findings, including no-RNA controls, non-irradiated siRNA controls, which showed no EFG1 down-regulation, and electroporated controls (**Figure 3.7**). Our results indicate that photoporation achieved higher gene knockdown efficiency compared to electroporation while maintaining cell viability. The enhanced performance of photoporation is likely attributed to the ability to transiently permeabilization of cellular barriers without inducing excessive mechanical stress[154]. Additionally, photoporation enables delivery without the need for specialized electroporation buffers or enzymatic degradation of the cell wall, reducing osmotic shock and cell loss[71].

These findings provide strong evidence that photoporation is an efficient method for inducing RNAi-mediated gene silencing in *C. albicans*. Also importantly, this study confirms that RNAi is active in strain 90028, marking a crucial step toward expanding RNAi-based approaches for fungal control. By overcoming previous limitations associated with strain SC5314, this work paves the way for further investigations into RNAi as a viable antifungal strategy, including the targeting of additional virulence-associated genes and the development of nanoparticle-based RNA delivery systems.

3.3 Conclusions

This study demonstrates the successful development and optimization of 800 nm AuNP-mediated photoporation as an efficient technique for delivering RNA molecules into yeast such as *S. cerevisiae* and *C. albicans*. Optimized parameters – including AuNP size (50 nm), concentration (4×10^{10} AuNP/mL), and laser wavelength (800 nm) – were established.

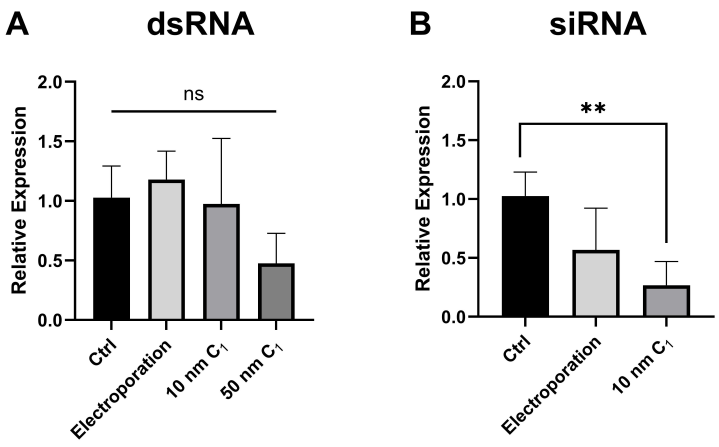

Figure 3.7: Fold-change of EFG1 in photoporated solutions of 1 x 10^7 cells/mL of *C. albicans* in the presence of AuNPs and (A) 15 ng/μL dsRNA or (B) 15 ng/μL siRNA. Ctrl = Non-irradiated cells grown in serum/YPD. Data represent mean values +SD of at least two biological replicates run in technical triplicate. Statistical significance: (**) p ¡ 0.002; (ns) p ¿ 0.12 versus control group (ANOVA, Dunnett posttest).

Additionally, changes in nanoparticle shape significantly altered the energetic dynamics of the system, thus demonstrating the need for a separate optimization process for non-spherical particles.

Compared to traditional methods such as electroporation, photoporation offers a less invasive, more efficient approach to transiently permeabilizing the cell membrane while maintaining higher cell viability. The biocompatibility of 800 nm light, which falls within the optical therapeutic window, minimizes phototoxic effects while enabling precise and controlled biomolecule delivery. In contrast, higher-energy 400 nm light increased cytotoxicity and eliminated the need for AuNP, both underscoring the advantages of NIR wavelengths for photoporation and opening up new potential avenues for developing NP-free photoporation methods. This study also demonstrated that delivery of siRNA occurs at similar, concentration-dependent efficiencies to CR dye, resulting in ¿90% efficiency using optimized photoporation parameters, confirming robust and consistent molecular uptake.

The successful knockdown of EFG1 using siRNA confirms that RNA interference (RNAi) is functional in *C. albicans* strain 90028, addressing prior limitations associated with the

widely used SC5314 strain, which harbors an AGO1 mutation that disrupts RNAi machinery. AuNP-mediated siRNA delivery achieved a nearly 75 % (0.25-fold) reduction in EFG1 expression, demonstrating its potential as a reliable gene-silencing tool. Additionally, photoporation outperformed electroporation in both gene silencing efficiency and cell viability, positioning it as a superior alternative for RNA-based antifungal strategies. The high efficiency of siRNA delivery, coupled with the observed gene silencing, highlights the effectiveness of this method for RNA-based interventions.

These findings mark a significant step toward nanoparticle-assisted RNA delivery systems for controlling fungal pathogens. The ability to effectively silence genes in *C. albicans* using photoporation opens the door for broader applications, including targeting additional virulence-associated genes and expanding RNAi-based gene silencing to other fungal species, such as filamentous fungi. Furthermore, this study underscores the complexity of designing a photoporation system, emphasizing the need for further optimization of AuNRs. Further optimization parameters still remain, including (but not limited to) NP surface coatings (e.g., citrate, different MW PEG, or carboxyl-PEG) and alternative materials such as silver. Future RNAi application studies should explore AuNP-mediated RNA delivery in filamentous fungi, such as *Trichophyton rubrum*, a prevalent dermatophyte responsible for skin infections.

3.4 Acknowledgements

I would like to thank Dr. Jeff Coleman (Auburn University, Department of Entomology and Plant Pathology) and Sabita Gyawali for their help in the design of EFG-1 dsRNA and RT-qPCR. Additionally I would like to thank Dr. Guillaume Laurent for use of his laser system and physics knowledge.

3.5 Materials and Methods

3.5.1 Chemical reagents and cell lines

C. albicans strain 90028 was purchased from American Type Culture Collection (Manassas, VA). *S. cerevisiae* BY4741 was kindly provided by Dr. Paul Cobine, Auburn University, Auburn, Al[127]. Cell culture media and supplements were obtained from Thermo Fisher Scientific (Manassas, VA), with the exception of peptone that was obtained from VWR (Radnor, PA). The cell detachment reagent Accutase was acquired from Corning (Corning, NY), and the 7-AAD dye was from TONBO Biosciences (San Diego, CA). The fluorescent dye 5(6)-carboxyrhodamine 110 hydrochloride was purchased from Biotium (Freemont, CA). All remaining reagents were purchased from Millipore Sigma (St. Louis, MO) unless otherwise indicated. Quartz spectrophotometer cells were from Starna Inc (Atascadero, CA). Gold nanospheres (10 nm + 5 kDa PEG) and nanorods (40±15 x 15±5), both with 5 kDA PEG, were obtained from NanoComposix (San Diego, CA). Both 20 nm and 50 nm gold nanospheres with 5 kDa PEG were purchased from Nanopartz (Loveland, CO).

3.5.2 Cell cultures and growth conditions

Cultures of wild-type *S. cerevisiae* BY4741 or *C. albicans* 90028 were grown in YPD medium (10 g of yeast extract, 5 g of peptone, and 20 g of glucose per liter) at 30 °C. A day before irradiation, an overnight culture of the appropriate strain was inoculated into 3 mL of YPD at 1×10^7 cells/mL and grown at 30 °C with shaking (200 rpm) to an OD600 of 0.6. The cells were harvested at 3000 g for 10 min, and the pellet was resuspended in alkaline PBS at a final concentration of 1×10^7 cells per mL.

3.5.3 Selection of dsRNA for targeted Candida loci

For gene knockdown in *C. albicans*, dsRNA sequences were designed targeting the genes EFG1 and GSC1. The dsRNA targeting EFG1 included bases 841-1,401 of the coding

sequence, and the dsRNA targeting GSC1 (FKS1) corresponded to bases 51-550 of the coding sequence. All dsRNAs were preferentially designed to target sequences towards the 5' end of the mRNA transcript. Both sequences were confirmed to only have sequence similarity to the intended targeted gene by the Basic Alignment Search Tool (NCBI BLAST). All dsRNAs were synthesized by RNA Greentech (Frisco, TX).

3.5.4 Electroporation

Overnight cultures of *C. albicans* were grown in YPD media at 30 °C. Cells were then counted and 1×10^7 cells/mL in cold, sterile diH_2O. Cells were spun down and washed with 1 mL cold, sterile 1 M sorbitol. All centrifugations were done at 2000 xg for 5 minutes. Cells were then resuspended in 0.1 M LiAc buffer (0.8 M sorbitol, 1X TE, 0.1 M LiAc) and incubated at 30 °C for 30 min. Fresh DTT was then added at a final concentration of 10 μM and cells were incubated another 15 minutes. Cells were then spun and resuspended twice, first in 500 μL and finally in 250 μL cold, sterile sorbitol. The cargo (10 μM CR dye, 5 μg siRNA, or 5 μg dsRNA) was then added to the cell solution, followed by a 10 minute incubation on ice. Cells were then loaded into pre-chilled electroporation cuvettes at pulsed at 1.5 kV for 5 ms using an Eppendorf EPorator (now by Calibre Scientiffic; Holland, OH). Cells were immediately recovered in 1 mL fresh YPD and incubated at 30 °C for 1 h before analysis.

3.5.5 ATTO-malemide labeling of EGF1-siRNA

Solutions of siRNA were labeled using a 5' EndTag^{TM} DNA/RNA labeling kit (Vector Labs, Newark, CA) following the provided protocol. Briefly, the amount of siRNA corresponding to 0.6 nmol of 5' ends was calculated through: A/(B+C) where A = ng/μL of siRNA stock, B = average molecular weight per nucleotide (317 μg/μmol) and C = number of base pairs. This solution was then treated with alkaline phosphatase to remove the 5' phosphate, followed by the addition of ATP-γ-S with a polynucleotide kinase. ATTO488 or

ATTO550 malemides (200 nmol) were then added and allowed to react for 30 min at 65 °C. Buffered phenol was then added, and the resulting aqueous layer was transfered to a fresh RNase-free tube. RNA was then precipitated and washed gently with ice-cold 75% EtOH to remove unbound label. Nanodrop was used to quantify concentration, and solutions of 1 μg/μL were aliquotted for delivery.

3.5.6 Cell irradiation

For irradiation optimization experiments, 1×10^7 cells/mL of *S. cerevisiae* were suspended in 1 mL of PBS. To the cell solution, AuNPs of 10, 20, or 50 nm diameter were added at a final concentration of $8x10^{10}$ (C_1, $4x10^{10}$ (C_2), or $8x10^9$ (C_3) AuNPs/mL. Immiediately prior to irradiation, 10 μM of the fluorescent dye 5(6)-carboxyrhodamine was added, and the mixture was transferred to a 10 mm path, quartz spectrophotometer cell. Samples were irradiated at 3.6 mJ/cm^2 for 10 min using an 11 W, 800 nm Ti:Sapphire fs instrument; fluence was controlled by varying the output power of the laser. A 20 cm convergent lens was placed in the beam path before the sample, and the sample itself was placed 10 cm away from focus (Figure A.5). The laser was blocked every $\sim$ 3 min and the solution was mixed using a transfer pipette. After irradiation, the solution was allowed to rest for 5 min at RT, centrifuged at 5000 rpm for 5 min, and then washed with PBS to remove any remaining fluorescent dye from the solution. For the intracellular delivery of siRNA or dsRNA in *C. albicans*, 15 μg of EFG-1 siRNA or dsRNA was added to the suspension. Samples were irradiated at 3.6 mJ/cm^2 for 10 min with mixing, and allowed to rest before centrifugation and washing like was done with the *S. cerevisiae* samples. All controls were subjected to similar conditions except exposure to fs laser pulses or addition of carboxyrhodamine, RNAs, or AuNPs.

3.5.7 Post-delivery induction of EFG-1

After electroporation, photoporation, or other treatment, cells were incubated 12 h in at least 3 mL of YPD containing adult bovine serum at 37 °C without shaking. Cells were then washed twice with PBS, being careful to not disturb the pellet, prior to analysis. All samples were treated with way, with the exception of indicated controls and ATTO-labeled siRNA samples, which were imaged immediately.

3.5.8 Flow cytometry

Upon irradiation, *S. cerevisiae* or *C. albicans* were suspended in PBS. 7-AAD was added to detect/exclude dead cells. A total of 10,000 cells per sample were analyzed using a MACSQuant Analyzer 10, Miltenyi Biotec. For both CR and ATTO488-siRNA, a 490 nm exitation laser was used, and the emitted fluorescence was detected using a 515 nm filter. Cellular fragments and debris were excluded from the analysis by using a side-scatter versus forward-scatter detection procedure, and cellular clumps were excluded by using forward-scatter height versus forward-scatter area detection.

3.5.9 Extraction of total RNA and cDNA synthesis

RNA was extracted from *C. albicans* cells utilizing mechanical cell disruption combined with the Qiagen RNeasy Mini Kit[155]. Cell pellets were resuspended in 600 μL of pre-chilled RLT buffer (Qiagen RNeasy Mini Kit) and mixed thoroughly by vortexing at maximum speed. The cell suspension was transferred to chilled screw-cap tubes containing zirconia beads and acid phenol (pH 4.5). The samples were bead-beaten for 3 minutes at 4 $^{\circ}C$, followed by centrifugation at 16000 xg for 8 minutes at 4 $^{/circ}$C. The aqueous layer was carefully transferred to a new RNase-free 1.5 mL microcentrifuge tube, and an equal volume of 70% ethanol was added. The mixture was inverted six times to ensure thorough mixing. After these steps, RNA extraction was completed following the Qiagen RNeasy Mini Kit protocol, adhering to the manufacturer's instructions. DNA contamination was removed

by in-column DNase I treatment (New England Biolabs). The concentration of total RNA was assessed by Nanodrop, ensuring the ratios were 260/280: 1.8-2.0 and 260/230: 2.0-2.2 and the integrity was assessed using gel electrophoresis. Samples were immediately frozen at -80 °C for storage before downstream use if needed. One μg of total RNA was reverse transcribed using the QuantiTect Reverse Transcription Kit (Qiagen) following the manufacturer's instructions. All synthesized cDNA samples were stored at -20 °C.

3.5.10 Gene expression analysis by RT-qPCR

The transcript expression of the targeted genes was determined by quantitative reverse transcription PCR (RT-qPCR) using a Bio-Rad CFX96 instrument and the PrimeTime Gene Expression Master Mix (Integrated DNA Technologies). For the analysis, primers and probes were designed together (**Table A.1**) (Integrated DNA Technologies), with FAM as the reporter dye for the housekeeping gene β-actin and CY5 for the gene of interest, EFG1. The cycling conditions were set to an initial denaturation at 95 °C for 5 min, followed by 40 cycles of denaturation at 95 °C for 10 seconds, and annealing/extension at 60 °C for 35 seconds. The efficiency of each primer-probe pair was assessed by conducting five series of a 10-fold serial dilution RT-qPCR assay, and the melt curve peaks were analyzed to verify the specificity of the amplification. The relative gene fold change for each target gene for each treatment was calculated using the $\Delta\Delta$Ct method, with the β-actin gene serving as a normalization reference.[153] Each gene expression analysis was performed in triplicate, with three technical replicates for each sample to ensure reproducibility. The primers and probes used to amplify the target gene (EFG1) and the housekeeping gene (β-actin) are listed in **Table** .

3.5.11 Software and statistical analyses

Flow cytometry data were analyzed using Flowlogic (Miltenyi Biotec) software. Statistics were performed using GraphPad Prism 5 software (GraphPad Software, La Jolla, CA).

A minimum of three replicates was performed for all conditions. Figures were created using Adobe Photoshop CC 2019.

Chapter 4

Insight into Cellular Uptake and Transcytosis of Peptide Nanoparticles in *Spodoptera frugiperda* Cells and Isolated Midgut

4.1 Introduction

Nanoparticle (NP)-mediated double-stranded RNA (dsRNA) delivery through feeding has become a promising approach for sustainable pest management[23, 24]. Cellular processing of dsRNA causes the silencing of vital genes, thus resulting in selective killing of targeted insect species[156]. Association of dsRNA with NPs protects the dsRNA from nucleases, harsh gut environment conditions, and also promotes translocation of dsRNA across the cell membrane[24]. Hence, NPs are able to enhance the silencing effects triggered by dsRNA. However, specifics of how NP-dsRNA complexes are internalized by gut cells and their subsequent path through the midgut tissue remains a mystery. Our research team developed peptide NPs called branched amphipathic peptide capsules (BAPCs)[79]. These unique peptide nanovesicles, or peptosomes, have been used successfully as delivery system of dsRNA and DNA in a variety of cell lines, including insect cells[24, 87, 59]. BAPCs form through the spontaneous assembly of two branched amphipathic peptides, bis(Ac-FLIVI)-K-K_4-$CONH_2$ and bis(Ac-FLIVIGSII)-K-K_4-$CONH_2$, in water. The association of BAPCs with nucleic acids, such as dsRNA, occurs mainly through electrostatic interactions between the cationic ϵ-amino groups on the poly-lysine tails and the anionic phosphates on the dsRNA backbone[157].

Our published studies demonstrated that feeding BAPC-dsRNA complexes successfully targeted essential genes in the red flour beetle (*Tribolium castaneum*) and the pea aphid (*Acyrthosiphon pisum*), leading to high mortality rates[59]. In both species, BiP and Armet, genes involved in the unfolded protein response (UPR) were suppressed, resulting in lethality[158, 159]. For *A. pisum*, ingestion of <10 ng of BiP-dsRNA associated with BAPCs led to the premature death of 75% of the subjects (n = 60) by day 5. The life span of *A. pisum* adult is about 20 - 30 days. *T. castaneum* larvae were effectively killed by ingestion using a combination of BiP-dsRNA and Armet-dsRNA complexed with BAPCs. By day 40, 75% of the subjects (n = 30) died as larvae or during eclosion. The life span of *T.castaneum* adult is around 2 years. Food supplemented exclusively with BAPCs did not affect survival rates. These results confirmed that complexation of dsRNA with BAPCs enhanced the oral delivery of dsRNA over dsRNA alone[59].

The sole purpose of the present article is to gain insight into the cellular uptake mechanisms, endosomal escape, cytotoxicity, and transport across the insect midgut epithelium of the BAPC-dsRNA complexes. As reported previously, BAPC-dsRNA complexes were able to cause knockdown in the *T. castaneum* vermilion gene that encodes a protein required for the development of normal eye color[59, 160]. Generally, effects of dsRNA are restricted to the delivery location (gut epithelium), but the absence of vermilion transcripts proved the ability of BAPC-dsRNA complexes to target genes outside of the gut[161]. To elucidate if transcytosis (a special type of vesicle-mediated transport) was involved in the translocation of the BAPC-dsRNA complexes through insect midguts, we mimicked ingestion of BAPCs in sixth instar *Spodoptera frugiperda* larvae. Isolated midgut tissues were carefully mounted into an Ussing chamber, along with biological buffers and rhodamine-labeled BAPCs (Rh-BAPCs)[162]. Ussing chambers utilize special buffers that mimic in vivo conditions and are divided into chambers separated by the harvested midgut tissue to create an *ex vivo* setting

that allows for the study of BAPC transcytosis[163]. Our findings indicated that transcytosis is involved in the transport of BAPCs and BAPC-dsRNA complexes across *S.frugiperda* midgut tissue.

Additionally, we explored the specific endocytic routes involved in the cellular internalization of BAPCs with and without dsRNA in the Sf9 cell line[164]. Cellular internalization processes can be broadly classified as clathrin-dependent or clathrin-independent. The clathrin-independent pathways can be more specifically classified as caveolae-dependent endocytosis, clathrin- and caveolae-independent endocytosis, and macropinocytosis[165]. To date, the best documented endocytic pathway in insects is the clathrin-dependent pathway[166, 56]. Although endocytosis of dsRNA associated with nanoparticles has been studied extensively in mammalian cells, details of those particular pathways in insect cells remains largely unknown[56, 67]. To probe the dependency of BAPC nanoparticles on different endocytic routes, we exposed Sf9 cells to BAPCs or BAPC-dsRNA complexes in the presence of selective endocytic inhibitors[167]. Confocal analysis demonstrated that clathrin-dependent endocytosis and macropinocytosis are the predominant uptake pathways used by BAPC-dsRNA complexes to access the cytosol of Sf9 cells.

Lysosome colocalization experiments were also performed to evaluate the fraction of BAPC-dsRNA complexes trapped within this degradative organelle. Increased presence of complexes within lysosomes may result in degradation of the dsRNA, thus reducing possible systemic delivery of dsRNA and silencing effects[168]. Results show that BAPCs only minimally colocalize within lysosomes. Production of reactive oxygen (ROS) and nitric oxide (NOS) species was also analyzed to ensure that the BAPC-dsRNA complexes did not generate oxidative stress in cells, which could affect off-target species. No significant production of ROS or NOS was found when Sf9 cells were exposed to BAPCs or BAPC-dsRNA complexes.

4.2 Results and Discussion

4.2.1 Biophysical Characterization of BAPC-dsRNA Complexes.

In this section, we sought to analyze the size and shape of the BAPCs associated with a 252 bp dsRNA (CYP450). Transmission electron microscopy (TEM) analysis revealed that, similar to previous atomic force microscopy (AFM) studies performed with a 390 bp dsRNA (BiP), BAPCs can act as cationic nucleation centers around which the negatively charged phosphate backbone winds, generating protecting dsRNA against nucleases (**Figure 4.1A,B,C**). The electrostatic association of dsRNA with BAPCs hinders nuclease binding sites, as we confirmed experimentally in previous studies[169]. The tangible silencing effects observed on *T. castaneum* and *A. pisum* also supports the protective role provided by BAPCs against nucleases and other potential degradation agents in the insect gut[59].

To further expand the biophysical analysis of the BAPC-dsRNA complexes, we also performed a DLS analysis[170]. This technique is used to determine the hydrodynamic diameter of nanoparticles dispersed in a liquid medium by measuring changes in the intensity of the scattered light.[56] The hydrodynamic diameter will depend not only on the size of the particle "core" but also ions present on the surface. In general, particles with a larger hydrodynamic diameter scatter much more light than small particles[171]. Different BAPCs and dsRNA formulations were analyzed by DLS by keeping the amount of dsRNA constant (1 μg) and varying the BAPCs concentration (**Figures 4.1D** and **B.1**). The BAPCs-dsRNA complexes displayed larger hydrodynamic diameters than the bare BAPCs, suggesting the association of dsRNA increases the size of the BAPCs or causes BAPCs to cluster together, which agrees with the TEM results. Additionally, the increase in size after association with dsRNA also indicates that the complexes are tightly bound as they do not readily dissociate upon dilution.

Finally, we analyzed the zeta potential (ZP) of BAPCs and the BAPC-dsRNA complexes (**Figure 4.1E**). ZP is a measure of the magnitude of the electrostatic charge or

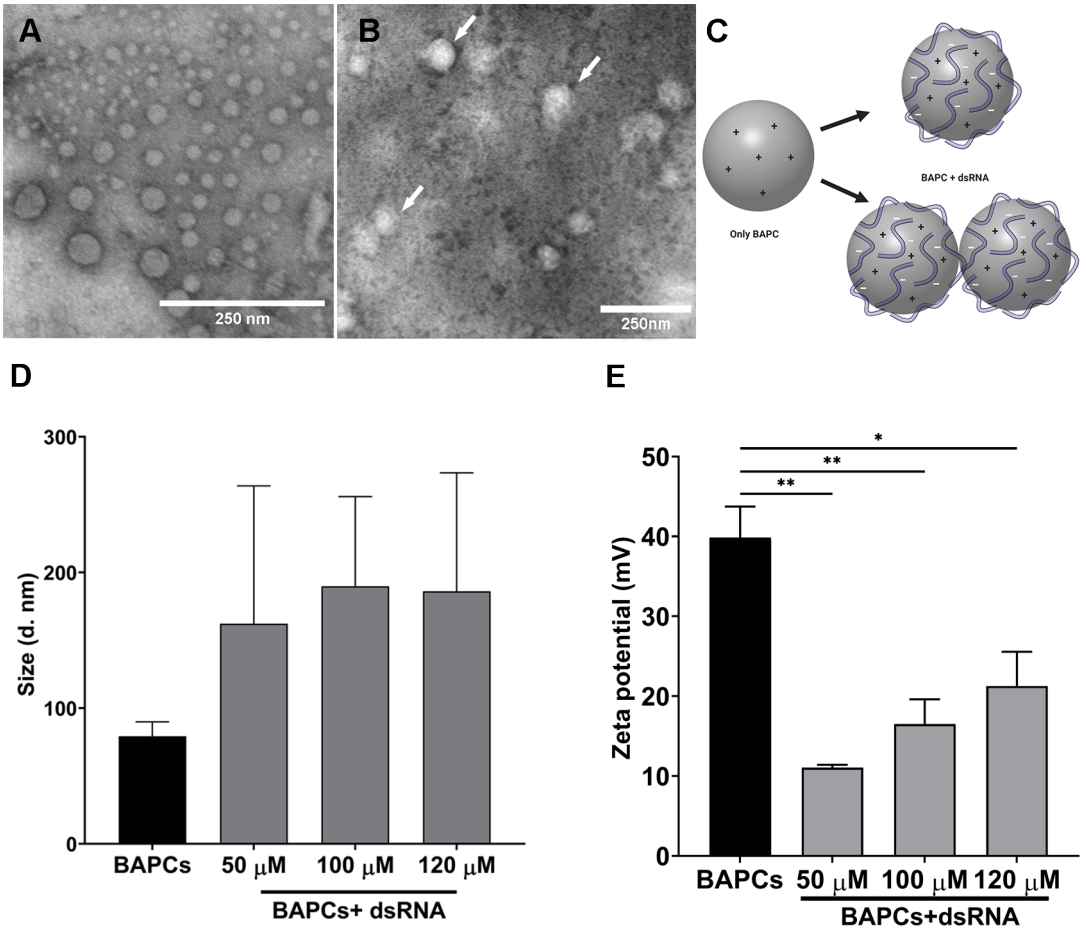

Figure 4.1: Biophysical characterization of BAPCs and BAPC–dsRNA complexes. (A) TEM analysis of bare BAPCs (50 μM) and (B) TEM analysis of BAPCs (50 μM) associated with dsRNA (1 μg). (C) Schematic representation of the BAPC-dsRNA complexes. (D) DLS and (E) ZP analysis of BAPC-dsRNA complexes at different concentrations associated with dsRNA (1 μg) . Statistical significance: (*) $p < 0.033$; (***) $p < 0.001$; (ns) $p > 0.12$ versus 50 μM BAPCs without dsRNA.(ANOVA, Tukey posttest).

repulsion/attraction between particles and is one of the fundamental parameters known to affect stability[112]. Positive ZP values might enhance electrostatic interactions with the negatively charged cell membranes[87, 167]. However, values above 45 mV can trigger high levels of toxicity[172, 74]. To investigate the ZP values of BAPCs and the BAPC-dsRNA complexes, different concentrations of BAPCs were analyzed both alone and complexed with 1 μg of dsRNA. BAPCs showed ZP values of $\sim$ 40 mV, and this value decreased to $\sim$10-20 mV after association with dsRNA, confirming TEM analysis results that the dsRNA surrounds the peptide nanocapsules, thus altering the surface charge. Despite varying BAPC

concentrations, the overall surface charge of the BAPC-dsRNA complexes remained positive, which facilitates interaction with negatively charged cell membranes.

4.2.2 Cellular Uptake Mechanisms and Lysosome Colocalization of BAPCs and BAPC-dsRNA complexes.

Studies conducted in mouse macrophages and rat intestinal epithelial cells demonstrated that macropinocytosis, clathrin-, and caveolae-dependent endocytosis are the prominent endocytic modalities for BAPC internalization in animal cells[173]. In this article, we seek to elucidate the internalization pathway of BAPCs and the BAPC-dsRNA complexes in insect cells. To accomplish this goal, we incubated Sf9 cells with fluorescent labeled BAPCs (Rh-BAPCs) in the presence of selective endocytic inhibitors[174]. Subsequently, cellular internalization was monitored qualitatively using confocal microscopy.

To inhibit clathrin-mediated endocytosis, we used CPZ and dynasore. Dynasore inhibits dynamin, and CPZ sequesters adaptor proteins and clathrin, thus depleting it from the plasma membrane[175, 176]. M-β-CD and nystatin were used to inhibit caveolae-dependent endocytosis[175]. M-β-CD and nystatin inhibit caveolae-dependent endocytosis by binding plasma membrane cholesterol which in turn perturbs fluidity of lipid rafts[175, 176]. To prevent macropinocytosis, we treated cells with cytochalasin D, which is specifically inhibits macropinocytosis and phagocytosis by inducing depolymerization of actin filaments which are essential for coating the macropinosomes[177]. A list of all inhibitors used and their mode of action is listed in **Table 4.1**.

Our results indicate that clathrin-mediated and macropinocytosis are the major endocytic routes employed by BAPCs to access the cytosol of Sf9 cells (**Figures 4.2** and **B.2**). Notably, for the BAPC-dsRNA complexes, the caveolae/lipid raft dependent endocytosis seemed to also play a role in the cellular internalization process. Several nanomaterials that have shown successful delivery use macropinocytosis since it forms a large leaky vesicle that

Pathway	Inhibitor	Mode of Inhibition	Ref
clathrin-mediated	chlorpromazine	sequesters clathrin and AP2 from the cell membrane	[175, 176]
clathrin-mediated	dynasore	inhibits dynamin and actin polymerization	[175, 176]
caveolae-mediated	methyl-β-cyclodextrin	extracts cholesterol from plasma membrane	[176]
caveolae-mediated	nystatin	extracts cholesterol from plasma membrane	[176]
macropinocytosis	cytochalasin D	caps and prevents assembly of actin	[175, 176, 177]

Table 4.1: Endocytosis pathway inhibitors and their modes of inhibition.

can enclose several nanoparticles[178]. Therefore, it was expected that this pathway was involved in the uptake of BAPCs in Sf9 cells. Review of literature suggests that one cell type can endocytose the same nanoparticle using multiple pathways, as nanoparticle formulations are often made up of a group of heterogeneous particles with different sizes, which makes the uptake process more diverse[73]. Clathrin-mediated endocytosis, macropinocytosis, and caveolae-mediated endocytosis have been documented before in insect cells, including Sf9 cells for the uptake of dsRNA, viruses, proteins and lipoproteins[179, 65, 180, 181, 182]. Nonetheless, this is the first study that demonstrates the implication of these pathways in the internalization of dsRNA and dsRNA associated with peptide nanoparticles.

After cellular entry, internalized nanoparticles are delivered to the early endosome. Subsequently, the early endosomes undergo a maturation process that ultimately results in the formation of the endolysosome, a temporary hybrid organelle resulting from fusion of late endosomes and lysosomes (**Figure 4.3A**)[67]. Lysosomes are regularly the final destination for external macromolecules and nanoparticles[183]. The lysosomal lumen has an acidic pH close to 4.5 and contains approximately 60 different soluble hydrolytic enzymes; thus, macromolecules and nanoparticles trapped within these organelles are often degraded[184]. Success in gene silencing through dsRNA is often hindered by the entrapment and subsequent degradation within this acidic organelle. This degradation process contributes to what is known

as dsRNA resistance, and it has been a barrier for the development of broader applications of dsRNA-based technology in insects[56].

To evaluate the entrapment of the BAPC-dsRNA complexes within the lysosomes; Rh-BAPCs complexed with dsRNA were incubated with Sf9 cells for 1 h, then lysosomes were stained using Cell Navigator. As shown in **Figure 4.3**, Rh-BAPC-dsRNA complex (**Figure 4.3B**) and the stained lysosomes (**Figure 4.3C**) are visualized in the Sf9 cells. Upon merging with bright field (**Figure 4.3D**), the two images show only a small fraction of the labeled BAPCs-dsRNA appeared to be colocalized within the lysosome, appearing as yellow spots indicated by white arrows (**Figure 4.3E**). These results suggest that BAPC-dsRNA complexes are processed by the endosomal route, yet rapidly escape the early or late endosomes. Most likely, the poly(L-lysine) tails of BAPC peptides trigger the rupture of the endosomes by osmotic pressure caused by a "proton sponge effect"[185].

The proton sponge effect is a proposed mechanism for nanoparticle endosomal escape[186, 187, 66]. In the case of BAPCs, the amine groups in the lysine tails act as proton sponges in acidic environments, thus creating a buffering system[188]. Protonation of the peptide causes an increase in pH, which in turn triggers an influx of protons in attempt to restore the acidic pH. Subsequently, water and other ions, such as chloride flood the vesicles, resulting in osmotic swelling. Osmotic swelling and pressure from electrostatic repulsions between similarly charged ions ultimately results in rupture of the lysosomal membrane. Once ruptured, the complexes are released into the cytosol, thus avoiding lysosomal entrapment and degradation – a previously identified source of failure of dsRNA in lepidopterans[184, 189]. Future studies in the escape of BAPC-dsRNA complexes will include the modification of the peptide sequences to include histidine residues, which exhibit increased proton sponge effects[190]. Similarly to lysine amine groups, the histidine imidazole ring prevents endosome acidification by capturing protons. This in turn triggers ATPase proton pumps to continue to transport protons into the endosome, followed by the influx of water and ions, ultimately resulting in rupture[23].

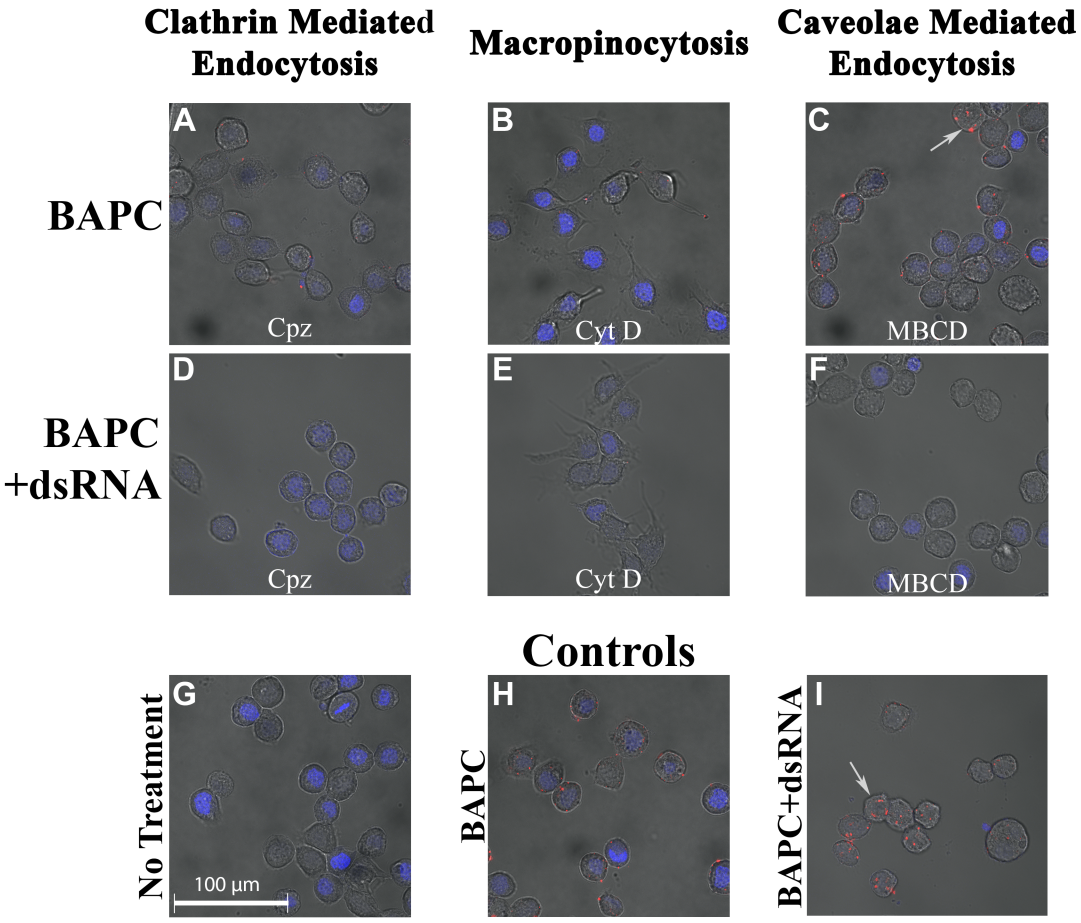

Figure 4.2: Endocytosis inhibition assay of BAPC and BAPC-dsRNA complexes in Sf9 cells. BAPCs were labeled with rhodamine B (red). Panels A-C correspond to uptake of BAPCs in the presence of inhibitors. Panels D-F correspond to uptake of BAPC-dsRNA complexes in the presence of inhibitors. Panel G are untreated Sf9 cells, and panels H and I are cells treated with BAPCs and BAPC-dsRNA complexes but without inhibitors.

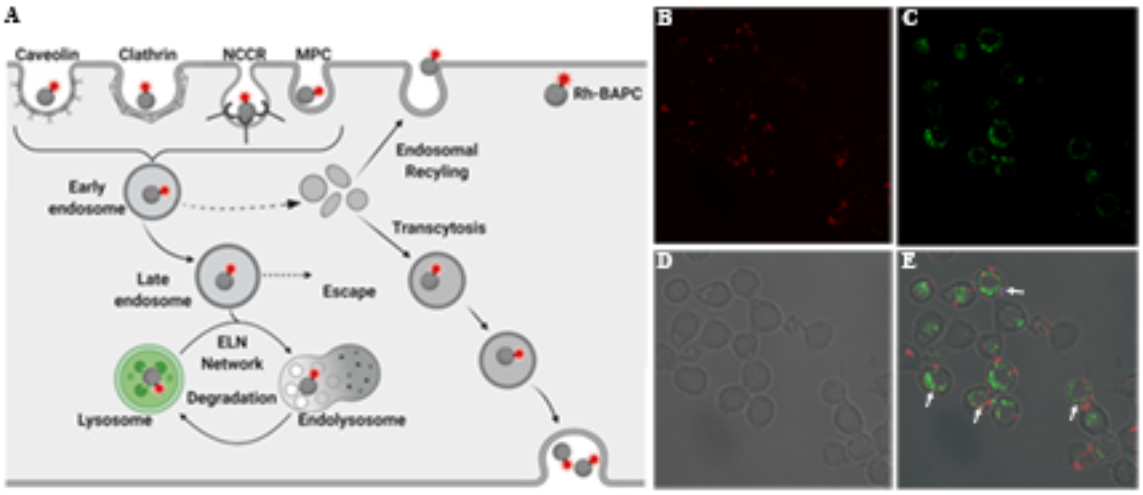

Figure 4.3: Colocalization of BAPCs with dsRNA in lysosomes. 2.5 μg of dsRNA was complexed with 50 μM of BAPCs and incubated with Sf9 cells for 1 h. Lysosomes were stained with Cell Navigator. Confocal microscopy was used to check for colocalization of complexes in lysosomes. (A) Schematic representation of endocytic pathways and endosome maturation process. (B) Rh-BAPCs (red), (C) lysosomes (green), (D) bright field, and (E) merge image showing colocalization of BAPCs and the lysosomes (yellow).

4.2.3 BAPC-dsRNA Uptake and Transport Across the Midgut Epithelium.

Silencing effects in insects induced by ingestion of dsRNA are generally localized in the delivery site (midgut cells), thus effects are transient and gene targets limited. Systemic delivery is more desirable since allows targeting genes from the whole insect (not just gut-specific)[161]. A better understanding of how these macromolecules cross the insect midgut will help to improve the oral delivery of dsRNA-based insecticides[24]. In some insect species, SID-1 like (SIL) channel proteins play a role in the uptake and midgut translocation of dsRNA[191, 192, 193, 194]. However, these channel proteins are not present in all insect species, implying that alternative transport mechanisms contribute to the translocation of dsRNA and NPs through the gut. Transcytosis is an active trans-cell transportation process used by multicellular organisms to selectively move material between two environments without altering the unique compositions of those environments[195]. In animal cells, it was

discovered that NPs are transported across biological barriers, such as the blood-brain barrier (BBB) through transcytosis[195]. In insects, the ability of viruses to transcytose across the gut epithelium and infect cells within the insect hemocoel has been well studied[162].

To elucidate if transcytosis was involved in the translocation of BAPCs through midgut epithelium cells, midguts of sixth instar *S. frugiperda* larvae were exposed to Rh-BAPCs and Rh-BAPC-dsRNA complexes for over a period of 60 min in an Ussing chamber (Figure 4A). *S. frugiperda* was selected as a model due to the previously reported occurrence of viral transcytosis and the availability of adherent epithelial cell lines (Sf21 and Sf9) to provide comparable in vitro data[162, 196].

Brefeldin-A (BFA) was used to study the potential role of transcytosis from the midgut lumen to the hemolymph. BFA is a selective transcytosis inhibitor that impacts the regulation and creation of Golgi transport vesicles[197]. Rh-BAPCs in the absence of BFA showed evident transcytosis (**Figure B.3**). Nanoparticles were added into the lumenal side, and over time, Rh-BAPC moved into the hemolymph compartment, thus increasing the relative fluorescence of that compartment. If active transport was not involved, the nanoparticles would have either remained within the tissue, thus causing no increase to the relative fluorescence of the hemolymph buffer, or diffusion of the buffers would have resulted in an equilibrium of fluorescence in both compartments. The relative fluorescence seen in the hemolymph increased after a period of 1 h, supports the occurrence of transcytosis (**Figure 4.4C**). Transcytosis of Rh-BAPCs associated with dsRNA showed a similar luminal uptake pattern. Nonetheless, the relative fluorescence detected in the hemolymph compartment was only slightly affected by the BFA inhibitor, suggesting that in the presence of dsRNA, alternative intracellular transport pathways are present. (**Figures 4.4B,C** and **B.3**).

To explore the involvement of clathrin in transcytosis, we also exposed midgut tissues to the inhibitor chlorpromazine (CPZ), which affects the assembly and disassembly of the clathrin lattice found on clathrin-coated pits.[198] The availability of clathrin to form lattices around vesicles is required for both clathrin-mediated endocytosis and transcytosis[199].

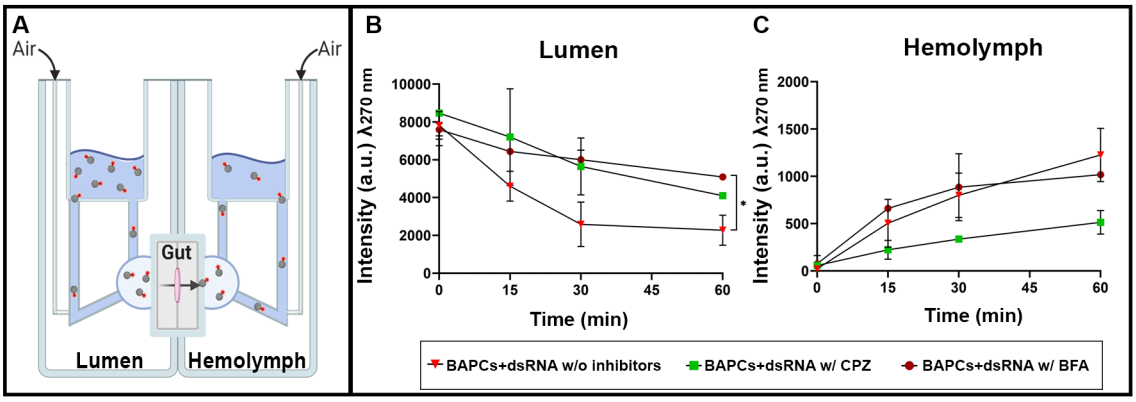

Figure 4.4: Transcytosis of Rh–BAPCs through *S. frugiperda* midgut in the presence of transcytosis and endocytosis inhibitors. (A) Scheme showing the movement of material through midgut tissue in an Ussing chamber. (B) Relative fluorescence of lumenal buffer or (C) hemolymph buffer over 1 h. Data represent mean values + SD of two experiments combined. Statistical significance: (*) $p < 0.033$; (***) $p < 0.001$; (ns) $p > 0.12$ versus Rh-BAPC + dsRNA control (no inhibitors) (ANOVA, Dunnett posttest).

According to **Figure 4.4B**, the addition of CPZ did reduce the degree of Rh-BAPC-dsRNA complex uptake from the lumen, thus resulting in much lower fluorescence in the hemolymph (**Figure 4.4C**). This has two implications: (1) the inhibition of clathrinmediated endocytosis reduces transcytosis since there are fewer BAPC-dsRNA complexes available to traffic across the cell and (2) BAPC-dsRNA complexes internalized via macropinocytosis (alternative uptake route for BAPCs) are unable to be transported through the epithelium access the hemolymph.

4.2.4 Cytotoxicity of BAPCs and BAPC-dsRNA Complexes in Insect Cells.

To ensure potential field applications of dsRNA-based technology, it is essential to understand the potential cytotoxic effects of the peptide nanoparticles and dsRNA in non-target organisms. By using Sf9 cells and the nonspecific dsRNA targeting *P. japonica*, we evaluated the generation of reactive oxygen species (ROS) by cells in response to BAPCs and BAPC-dsRNA complexes. Production of ROS is a potent early marker for nanoparticle toxicity.[200, 201] Although ROS toxicity is more commonly observed with metallic nanoparticles, measuring ROS production resulting from BAPC delivery in Sf9 cells gives

us a better picture of potential downstream effects from a cytotoxicity perspective. One key factor involved in nanoparticle-induced ROS is the presence of prooxidant functional groups on the reactive surface of nanoparticles[200]. Production of ROS can disrupt mitochondrial activity, cause damage to DNA, and cause lipid peroxidation. This in turn destabilizes the cell membrane, making it more susceptible to oxidation[202]. ROS was detected using the CellROX Deep Red fluorescence assay[86]. The membrane permeable CellROX reagent is nonfluorescent until oxidized, and release of reactive oxygen species causes fluorescence at a maxima of 665 nm. According with the results (**Figure 4.5A**), BAPCs and the BAPC-dsRNA complexes did not cause a significant increase in the ROS when compared with untreated cells.

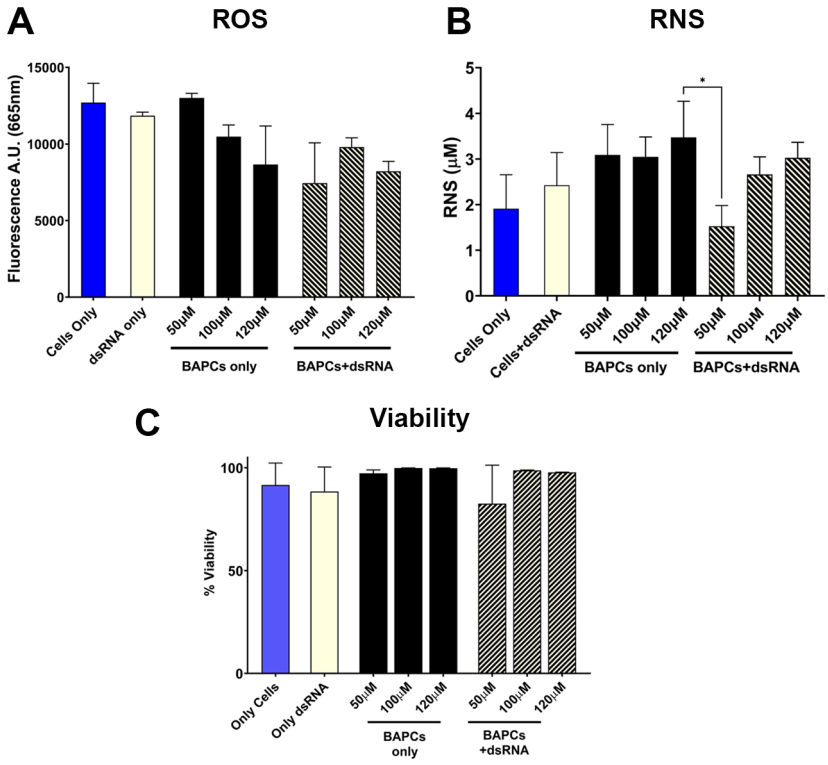

Figure 4.5: Effect of BAPC-dsRNA complexes on cell viability and oxidative stress. (A) Relative production of ROS based on treatment group. (B) Relative production of RNS based on treatment group. (C) How cell membrane integrity is affected by the different treatment groups using the dead cell exclusion dye 7-AAD. Data represent mean values + SD of two experiments combined. Statistical significance: (*) $p < 0.033$; (***) $p < 0.001$; (ns) $p > 0.12$ versus groups indicated in the bars (ANOVA, Dunnett posttest).

Similar to ROS, reactive nitrogen species (RNS) are naturally occurring within living systems. At low levels they are used by organisms for signaling purposes[203]. However, higher levels of RNS can be detrimental to the cells ultimately leading to cell death. In the instance that ROS and RNS production are both increased, there becomes the danger of creating peroxinitrite, which is a potent oxidative agent that can damage DNA[203, 204]. The production of RNS in Sf9 cells was quantified using Griess Reagent alongside a standard curve. As shown in **Figure 4.5B**, there is no significant difference between the control groups (untreated cells) and both BAPCs and BAPC-dsRNA complexes.

Cytotoxicity was evaluated by flow cytometry as well (**Figure 4.5C**). This is a rapid and reliable method commonly used to quantify cell viability[25]. Dead cells can be identified by using fluorescence probes that intercalate into DNA of cells with compromised cell membrane, such as 7-AAD. The viability of Sf9 cells treated with 50, 100, and 120 mM of BAPCs with or without dsRNA was minimally affected (<15% cell mortality), but according with the statistical analysis ($p > 0.12$), no significant difference was found when compared with untreated cells. We also analyzed viability in the presence of the endocytosis inhibitors, to ensure that this cell viability was preserved during the treatments. None of the inhibitors caused a decrease in cell viability or increase of oxidative stress, thus avoiding false-positive uptake results produced by damaged cell membranes (Figure B.4). Altogether these results indicate that BAPCs neither induce cell death nor oxidative stress in insect cells. Moreover, studies conducted in mammalian cell lines and animal models also indicated that BAPCs do not induce acute toxicity and are not immunogenic, making them a suitable candidate for field applications for dsRNA delivery.[87]

4.3 Conclusions

The present study demonstrated that BAPCs and BAPC-dsRNA complexes are able to transverse the gut of *S. frugiperda* via an active transport process called transcytosis. Using a physiological chamber that mimics in vivo conditions, midguts of sixth instar *S.*

frugiperda larvae were exposed to fluorescent BAPC complexes. Over an hour, fluorescence levels decreased in the lumenal compartment and increased in the hemolymph in a time-dependent manner, indicating the movement of the complexes from the lumen compartment to the hemolymph compartment. Upon the addition of BFA, a specific transcytosis inhibitor, decrease in fluorescence in the hemolymph was observed after 60 min compared to trials without inhibitors[197]. This is the first report that demonstrates the involvement of transcytosis in the translocation of dsRNA and nanoparticles through the midgut in lepidopterans. The ability of BAPCs to move within tissues via transcytosis is highly desirable for pest management, since it will allow for more widespread silencing effects[162].

We also studied the endocytic uptake routes of the BAPC-dsRNA in Sf9 cells. Specific endocytosis inhibitors were used to individually target macropinocytosis, clathrin-mediated endocytosis, and caveolae-mediated endocytosis[174, 175]. Confocal analysis indicated that macropinocytosis and clathrin-mediated endocytosis are the major uptake routes involved in BAPC-dsRNA complex internalization. Additionally, our results showed that once internalized, BAPC-dsRNA complexes are only minimally colocalized within lysosomes. This means they are able escape the endosomal pathway, possibly due to a phenomenon called the proton sponge effect. In this process, the endosomal membrane is destabilized by osmotic pressure because of a rapid influx of protons and solvated ions[184]. Endosomal escape is an important feature to consider toward the development of efficient dsRNA-biopesticides[205].

Finally, exposure to BAPCs or BAPC-dsRNA complexes did not result in increased production of cytotoxic reactive nitrogen or oxygen species in Sf9 cells. Excess of either of these cellular stress markers can indicate mitochondrial dysfunction, peroxisome activity, DNA damage, or cause lipid peroxidation and result in unwanted cell death to other off-target species[200, 203]. The integrity of the cell membrane, which is essential for normal cell function was also maintained after exposing cells to BAPCs and the BAPC-dsRNA complexes. These findings are particularly relevant to ensure that BAPCs-based technology will not harm off-target species.

4.4 Materials and Methods

4.4.1 Chemical Reagents and Cell Lines.

Sf9 insect cells (Novagen, St. Louis, MO, USA), sixth instar *S. frugiperda* (Benzon Research, Carlisle, PA, USA), 2,2,2-trifluoroethanol (TFE) (Thermo Fisher, USA), 6-well treated tissue culture plates (Corning Inc. Corning, NY, USA), 5(6)-carboxytetramethylrhodamine N-succinimidyl ester (Sigma-Aldrich, St. Louis, MO, USA), Grace's Insect Medium 1× supplemented (Thermo Fisher, USA), fetal bovine serum (FBS) (CPS Serum, Parkville, MO, USA), chlorpromazine (CPZ) (SigmaAldrich, St. Louis, MO, USA), dynasore and nystatin (SigmaAldrich, St. Louis, MO, USA), methyl-β-cyclodextrin (M-β-CD) (Millipore Sigma, USA), cytochalasin D (Cyt D) (Tocris Biosciences, MN, USA), brefeldin A (BFA) (Sigma-Aldrich, St. Louis, MO, USA), 7-aminoactinomycin D (7-AAD) (Tonbo, San Diego, CA), paraformaldehyde (Sigma-Aldrich, St. Louis, MO, USA), CYP450 dsRNA (RNA Greentech, USA), Griess reagent kit for nitrite quantification (Invitrogen, USA), CellROX Deep Red (Invitrogen, USA), and Cell Navigatior Lysosome Staining Kit – Green Fluorescence (AAT Bioquest, Sunnyvale, CA).

4.4.2 Synthesis of BAPCs.

The peptides bis(Ac-FLIVI)-K-K_4-$CONH_2$ and bis(Ac-FLIVIGSII)-K-K_4-$CONH_2$ were synthesized as previously described[79]. To determine each peptide's concentration, they were separately dissolved in TFE and the absorbance of phenylalanine (two per sequence) at 257.5 nm was measured. In TFE, both peptides are helical and monomeric, thereby ensuring complete mixing when combined. After calculating concentrations, the peptides were then mixed at equimolar ratios to generate a stock with a calculated final concentration of 1 mM in the final volumes and then dried in vacuo. BAPCs were formed by hydrating dried peptides at 25 °C and allowed to stand for 10 min before solution was cooled and incubated

at 4 °C for 1 h[87]. After 1 h, the peptide sample was returned to 25 °C for 30 min before drying for long-term storage or mixing with the dsRNA.

4.4.3 Preparation of Rhodamine-Labeled BAPCs (Rh-BAPCs).

Rh-BAPCs were prepared similarly to the normal BAPCs, with slight variation. The bis(Ac-FLIVI)-K-K_4-$CONH_2$ component of the mixture was modified by the incorporation of N-hydroxysuccinimide ester of rhodamine B, and combined 1:1 with the unlabeled peptide (**Method B.1** and **Figure B.5**) Thus, the final peptide mixture consisted of equimolar concentrations of bis(Ac-FLIVIGSII)-K-K_4-$CONH_2$ and bis(Ac-FLIVI)-K-K_4-$CONH_2$, with half of the latter being rhodamine labeled (25% Rh-labeled peptide and 75% unlabeled peptide). Work with Rh-BAPCs was performed protected from light to avoid quenching of the fluorophore. As previously described, the peptide mixture was then dissolved in nuclease-free water and incubated at room temperature for 10 min, then kept at 4 °C for 1 h. After 1 h, the peptide sample was returned to 25 °C for 30 min before drying for long-term storage or mixing with dsRNA. The biophysical characterization of the Rh-BAPCs was included in **Figure B.6** and **Table B.1**.

4.4.4 Synthesis of Rhodamine-labeled bis(Ac-FLIVI)-K-K_4-$CONH_2$

Rhodamine-labeled bis(Ac-FLIVI)-K-K_4-$CONH_2$ was synthesized using solid phase peptide synthesis chemistry on Rink Amide Resin (Rink resin SS, 100-200 mesh, 1% DVB; Advanced ChemTech; Louisville, KY, USA). After coupling the first residue (Nα-Fmoc-Nϵ-Dde-L-Lysine), the resin was treated with 2% hydrazine for 10 minutes on a Burrell Model 75 wrist action shaker (Burrell Scientific; Carlisle, PA, USA) to remove the Dde (N-(1-(4,4-dimethyl-2,6-dioxocyclohexylidene)ethyl)) protecting group and expose the lysyl ϵ amine. This residue was then manually reacted with one equivalent of the N-Hydroxysuccinimidyl ester of Rhodamine B (Sigma-Aldrich Corp.; St. Louis, MO, USA) in the presence of N-N-Diisopropylethylamine on the shaker for 2 h to generate the label on the C-terminal lysine.

The rest of the synthesis was carried out as previously described [79]. Rd-BAPCs were formed by combining equimolar amounts of bis(Ac-FLIVIGSII)-K-K_4-$CONH_2$ and bis(Ac-FLIVI)-K-K_4-$CONH_2$, with half of the latter being composed of bis(Ac-FLIVI)-$KK_3K(\epsilon$-Rd)$CONH_2$. The overall yield of the synthesis was 52%. This value was calculated from the theoretical value (100%) using 500 mg of the resin (loading capacity = 0.5 mmol/g) and the theoretical yield: 659.3 mg.

4.4.5 4.4. Synthesis of dsRNA.

The dsRNA sequences targeting the CYP-450 gene in *Popillia japonica* and *Spodoptera exigua* were designed and obtained from RNA Greentech LLC, Texas, USA. First, the mRNA sequence of CYP-450 (*P. japonica* GARJ01000597 and *S. exigua* KX443442.1) were obtained from NCBI nucleotide database. The selected gene sequences were further screened through GenScript siRNA target finder tool to predict siRNA sequences. The sequence region with highest predicted siRNAs was selected for dsRNA synthesis. Sequences from *S. frugiperda* were not selected for dsRNA design to allow testing for off-target effects. Nonetheless, the *S. exigua* CYP-450 sequence overlaps ∼90% with *S. frugiperda*. At least indicated, all experiments were carried out with the CYP-450 *P. japonica* gene.

4.4.6 Preparation of BAPC-dsRNA Complexes.

To form the BAPC-dsRNA complexes, CYP-450 dsRNA (1 μg) suspended in nuclease-free water was added dropwise to aqueous solutions containing 50, 100, or 120 μM BAPCs or Rh-BAPCs. Solutions were then mixed carefully by pipet and allow to stand for 10 min before adding $CaCl_2$ (2.0 mM). The final solution was incubated another 30 min then used promptly for cellular uptake and transcytosis experiments. The biophysical characterization of the Rh-BAPC-dsRNA complexes was included in **Figure B.6** and **Table B.1**.

4.4.7 Dynamic Light Scattering (DLS), Zeta Potential (ZP), and Transmission Electron Microscopy (TEM) Analysis.

BAPC-dsRNA complexes were prepared following the protocol previously described. Particle sizes and zeta potentials of BAPCs and BAPC-dsRNA complexes were determined using a Zetasizer Nano ZS (Malvern Instruments Ltd., Westborough, MA). Samples were analyzed in nucleasefree water and all measurements were performed in triplicates. For TEM analysis, 50 μM of BAPCs mixed with or without 1 μg dsRNA were added directly onto individual grids (FCF 300-Cu, Formvar carbon film on a 300-mesh copper grid, Electron Microscopy Sciences, Hatfield, PA, USA) and allowed to dry for 2 h at room temperature. Next, samples were negatively stained using phosphotungstic acid and allowed to dry for additional 1 h. TEM imaging was performed at 60 kV on a Zeiss EM10.

4.4.8 Sf9 Cell Cultures and Growth Conditions.

Sf9 cells were grown in supplemented Grace's Insect Media supplemented with 10% fetal bovine serum with no addition of antibiotics. Cell cultures were grown at 28 °C and ambient CO_2. Adherent cultures were passaged every fourth to fifth day by pipetting media gently across the growth surface until cells were homogeneously in solution. Cells were then transferred to a new T25 flask at 1×10^6 cells/mL. The media was replaced every 48 h or as needed.

4.4.9 Endocytosis Inhibition Study.

Sf9 cells were seeded in 6-well plates containing glass coverslips at a concentration of 1×10^6 cells/mL and incubated for 36 h at 28 °C. Subsequently, media was removed, cells were washed with PBS and inhibitors of endocytosis were added in fresh media at their respective concentrations. Concentrations of inhibitors were as follows: M-β-CD at 5 mM, CPZ at 10 μM, dynasore at 80 μM, cytochalasin D at 4 μM, and nystatin at 50 μM. This inhibitor pretreatment was carried out for 30 min at 28 °C. After inhibitor pretreatment, Rh-BAPCs

were added to the wells at a concentration of 50 μM and incubated for 1 h at 28 °C. Cells were washed once with PBS and then fixed for 15 min with 4% paraformaldehyde, followed by one more PBS wash. Coverslips were removed from the 6-well plates and mounted to microscope slides using ProLong Diamond Antifade Mountant. Fluorescent imaging was carried out using the Nikon A1R MP Confocal Microscope. The same protocol was used for endocytic analysis of BAPC-dsRNA complexes with Rh-BAPCs being conjugated with dsRNA.

4.4.10 Determination of Reactive Nitrogen Species (RNS) and Reactive Oxygen Species (ROS).

Reactive nitrogen (nitric oxide) species were detected using the Griess Reagent Kit for Nitrite Determination from Invitrogen. Cells were seeded in 96-well plates at a concentration of 1×10^6 and incubated for 48 h at 28 °C. Cell media was removed, and cells were washed with PBS. After inhibitor pretreatment, BAPCs or BAPC-dsRNA complexes were added to the wells at a concentration of 50, 100, and 120 μM and incubated for 1 h at 28 °C. Cells were then treated with the Griess reagent as per kit instructions. A standard curve was created by diluting the provided nitrite solutions to final concentrations of 0, 1, 5, 10, 20, 30, 40, and 50 μM. Absorbance at 548 nm was read using automatic plate reader BioTek Cytation3.

The presence of ROS was detected using CellROX Deep Red Reagent. Cells were seeded in 96-well plates containing glass coverslips at a concentration of 1×10^6 and incubated for 48 h at 28 °C. Media was removed, cells were washed with PBS, and inhibitors of endocytosis were added in fresh media at their respective concentrations, listed previously. Inhibitor pretreatment was carried out for 30 min at 28 °C. After inhibitor pretreatment, BAPCs or BAPC-dsRNA complexes were added to the wells at a concentration of 50, 100, and 120 μM and incubated for 1 h at 28 °C. Subsequently, cells were incubated with CellROX Deep Red

Reagent (640/655 nm) at a final concentration of 5 μM and protected from light for 30 min at 28 °C. Fluorescence was read at 655 nm.

4.4.11 Cytotoxicity Experiment Using Flow Cytometry.

Sf9 cells were seeded in 12-well plates at a concentration of 1×10^6 cells/mL and incubated for 36 h at 28 °C. Cell media was then removed, and media with BAPCs or BAPC-dsRNA complexes at 50, 100, or 120 μM were added into the appropriate wells at the concentration previously listed. Same protocol was followed for the endocytosis inhibitors, using the concentrations previously listed. The plates were then incubated for 30 min at 28 °C. Cells were incubated an additional hour; then, they were washed with PBS and detached from the wells by pipetting. After centrifugation at 1700 rpm for 5 min, cells were resuspended in PBS and 7-AAD was added to detect and exclude dead cells. A total of 10,000 events per sample were analyzed using a MACSQuant Analyzer 10, Miltenyi Biotec. Side scatter vs forward scatter gating method was used to eliminate debris and cell clumps. A full gating strategy is shown in **Figure B.7**. Data was analyzed using FlowLogic (Miltenyi Biotec) software.

4.4.12 Lysosome Colocalization.

Cells were seeded in a 6-well plate containing sterile glass coverslips at 1×10^6 cells/mL and incubated for 36 h at 28 °C. Cell media was removed, and cells were washed with PBS. The working solution of Cell Navigator was prepared as according to kit instructions. A 1:1 ratio of cell media to Cell Navigator solution was added to the wells, and cells were incubated 2 h at 28 °C. Rh-BAPCs (50 μM) complexed with dsRNA (1 μg) were added into the wells 30 min before the Cell Navigator solution was removed. Cells were, then, washed with PBS twice, and coverslips were mounted using ProLong Diamond Antifade Mountant (Thermo) and allowed to dry overnight protected from light overnight. Slides were then imaged using the Nikon A1R Confocal Microscope.

4.4.13 Insect Rearing.

S. frugiperda (fall armyworm) eggs placed in individual growth containers were obtained from Benzon Research (Carlisle, PA, USA). Larvae were reared on a provided wheat germ and soy flour-based artificial diet in a growth chamber at 29 °C with a 12:12 (L:D) photoperiod. Larvae were grown until reaching sixth instar and then were selected for Ussing chamber experiments.

4.4.14 Midgut Isolation.

Larvae were selected after reaching sixth instar but before pupation for dissection. Dissections were performed in insect physiological solution (47 mmol/L KCl, 20.5 mmol/L $MgCl_2$, 20 mmol/L $MgSO_4$, 1 mmol/L $CaCl_2$, 88 mmol/L sucrose, 4.3 mmol/L K_2HPO_4, 1.1 mmol/L KH_2PO_4, adjusted to pH 7.5) at room temperature.12 The midgut was exposed by creating a longitudinal incision on the ventrolateral side. The midgut was isolated and stabilized between two pins before opening it longitudinally. The procedure was done carefully to avoid puncturing, as perforation of the midgut will result in diffusion of particles between chambers rather than active transport. Once opened, the gut was rinsed with insect physiological solution to remove debris then immediately mounted on a modified 0.1 cm^2 slider (Figure B.8A) with great care to conserve lumenal and hemolymphatic orientation.

4.4.15 Ex Vivo Transcytosis Experiments.

Midguts mounted in sliders were inserted into an Ussing chamber (Physiologic Instruments, San Diego, CA, USA; Model P2300) (Figure B.8B). The tissue was perfused with 2-3 mL lumenal buffer (5 mmol/L $CaCl_2$, 24 mmol/L $MgSO_4$, 20 mmol/L potassium gluconate, 190 mmol/L sucrose, 5 mmol/L CAPS, pH 10.0) on the lumen side of the midgut, and 2-3 mL of hemolymph buffer (5 mmol/L $CaCl_2$, 24 mmol/L $MgSO_4$, 20 mmol/L potassium gluconate, 190 mmol/L sucrose, 5 mmol/L Tris, pH 7.0) on the hemolymphatic side. Air was bubbled gently to each side of the tissue using a Tetra Whisper Air Pump (30-60

gallons; Tetra, Blacksburg, VA, USA). Air flow rate used was 2.6L/min. Experiments were run at 25 °C protected from light. Rh-BAPCs (50 μM) and Rh-BAPC-dsRNA (50 μM+1 μg dsRNA) complexes were added to the lumenal buffer and 100 μL samples were taken at 0, 15, 30, and 60 min from both sides. Transcytosis-specific inhibitor BFA (10 μM) and endocytosis inhibitor CPZ (10 μM) was added 30 min prior to adding BAPCs or complexes. Samples were loaded in a dark-sided 96-well plate and analyzed using a BioTek Cytation 3 plate reader (excitation 544 nm, emission 576 nm). Change in relative fluorescence over time was plotted to visualize the subsequent fluctuation of relative fluorescence because of transcytosis. dsRNA-CYP-450 (*S. exigua*) was used for this set of experiments.

4.4.16 Confocal Laser Scanning Microscopy.

Images were obtained using a Nikon A1R MP confocal microscope (Carl Zeiss, Gottingen, Germany).

4.4.17 Software and Statistical Analyses.

Statistics were performed using GraphPad Prism 5 software (GraphPad Software, La Jolla, CA). A minimum of two replicates were performed for all conditions. Figures were created using biorender.com and Adobe Photoshop CC 2019.

4.5 Acknowledgements

This project was supported by the Alabama Agricultural Experiment Station and the Hatch program of the National Institute of Food and Agriculture, U.S. Department of Agriculture. We would also like to thank the lab of Dr. John Tomich at Kansas State University for supplying the rhodamine labeled peptide used in this work.

Chapter 5

Oral delivery of Branched Amphipathic Peptide Capsules complexed with dsRNA resulting in RNA interference of V-ATPase subunits in *Spodoptera frugiperda* larvae

5.1 Introduction

The fall armyworm (*Spodoptera frugiperda*) is a highly destructive agricultural pest that poses a major threat to global food security[17, 6]. Populations of *S. frugiperda* in several countries have evolved resistance to multiple classes of insecticides, including pyrethroids, organophosphates, and *Bacillus thuringiensis* (Bt) toxins, making alternative control methods a critical priority.[6] RNA interference (RNAi), a highly conserved cellular mechanism that regulates gene expression by degrading mRNA transcripts in a sequence-specific manner, has emerged as a promising approach for targeted pest control that could reduce reliance on traditional pesticides[23, 206, 24]. However, successful RNAi application in lepidopteran insects is often hindered by dsRNA instability in the insect gut and inefficient cellular uptake[189, 166].

In insects, RNAi can by triggered by the delivery of exogenous double-stranded RNA (dsRNA), which is processed into small interfering RNAs (siRNAs) by the enzyme Dicer[207]. These siRNAs are then incorporated into the RNA-induced silencing complex (RISC), where they guide the degradation of complementary mRNA, effectively knocking down target gene expression. This pathway is a known anti-viral response in insects, and studies using baculovirus to deliver dsRNA have shown promising results[2]. The dsRNAs to be delivered can be designed such that they are sequence-specific to the target organism, thus lowering off-target mortality of beneficial insects like pollinators[24, 208]. The ability to silence genes essential for insect survival, development, or reproduction make RNAi a versatile alternative to the use of traditional chemical pesticides[24].

Despite its promise, RNAi efficiency varies across insect orders[156, 209]. For example, coleopteran insects such as the red flour beetle (*Tribolium castaneum*), efficient RNAi has been well documented, while in lepidopteran insects, such as *S. frugiperda*, RNAi has been less reliable due to dsRNA degradation by gut nucleases, limited cellular uptake, and inefficient systemic spread.[210, 209] Therefore, developing improved delivery methods to enhance dsRNA stability and uptake is crucial for achieving effective gene silencing in lepidopteran pests.

The potential of nanoparticle-mediated nucleic acid delivery systems to enhance RNAi efficiency in insects has recently become an active field of study[211]. Nanoparticles are well-known for being able to help protect and stabilize RNA, making them an attractive platform for RNA delivery. The previous chapter demonstrated the ability of branched amphiphilic peptide capsules (BAPCs) to be internalized by Sf9 cells, avoid lysosomal degradation, and transcytose through gut tissue, suggesting they may have promise as a more consistent dsRNA delivery system in lepidopteran organisms. BAPCs are cationic, self-assembling nanoparticles composed of equimolar concentrations of the peptides $(Ac\text{-}FLIVI)_2$-K-K_4-$CONH_2$ and $(Ac\text{-}FLIVIGSII)_2$-K-K_4-$CONH_2$. BAPCs have been well documented as being capable of complexing with nucleic acids via electrostatic interactions between the nucleic acid backbone and the positively charged BAPC surface which helps protect them from nuclease degradation and facilitates cellular uptake by midgut cells[169, 212]. Previous studies in red flour beetles and aphids (*Acyrthosiphon pisum*) have demonstrated that BAPC-dsRNA complexes effectively induce gene silencing in BiP and Armet, two essential genes, resulting in significant mortality[59]. In this study, we continue to investigate the use of BAPCs as a nanocarrier for dsRNA in the lepidopteran *S. frugiperda*.

As a proof of concept, we targeted transcripts encoding Vacuolar ATPase (V-ATPase) subunits A, B, and D. V-ATPase is a highly conserved, multi-subunit enzyme complex responsible for proton transport across membranes, playing a crucial role in maintaining pH

homeostasis, ion transport, and membrane trafficking in eukaryotic cells[213, 214]. It is composed of two major domains: V_1 and V_o. The V_1 domain, which is primarily responsible for ATP hydrolysis, is located in the cytoplasm, and consists of eight subunits (A-H). Subunits A and B form a globular hexamer consisting of 3 copies of each subunit, where subunit A catalyzes ATP hydrolysis and subunit B binds ATP[215]. Subunit D is part of the central rotor mechanism that transmits rotational energy generated by ATP hydrolysis and connects the V_1 domain to the membrane-embedded V_o domain, thus giving it a critical structural and functional role.[215]. The hydrophobic V_o domain (subunits subunits a, c, c', c", and d) lies within membrane and is responsible for proton translocation. **Figure 5.1** describes this process in more detail. V-ATPase is also essential for acidification of endosomes, lysosomes, and Golgi-derived vesicles, which are essential for regulating processes such as protein degradation. In insects, V-ATPase plays a critical role in gut alkalization, which is essential for digestion and nutrient absorption[213, 214, 216]. Given its essential function, V-ATPase has been identified as a promising RNAi target for pest control, as its disruption can lead to physiological failure and mortality in insects[2].

This work continued exploring BAPC-dsRNA complexes as an alternative bio-pesticide by evaluating the effect of feeding BAPCs and BAPC-dsRNA complexes in the fall armyworm. This was accomplished by adding solutions containing BAPCs or BAPCs complexed with dsRNA against V-ATPase subunits A, B, or D to the diet of second to third instar larvae. We assessed several factors including the effect of BAPC concentration on feeding behavior, the survival of larvae fed BAPC-dsRNA complexes, and the effect dsRNA feeding had on transcript levels. Additionally, this study compared the effect of targeting different V-ATPase subunits. Given the need for novel, eco-friendly pest control strategies to combat pesticide resistance, results provides valuable insights into nanoparticle-assisted RNAi as a potential biological alternative to chemical insecticides for sustainable insect pest management. Additionally, this is the first study exploring their use in a lepidopteran species, and

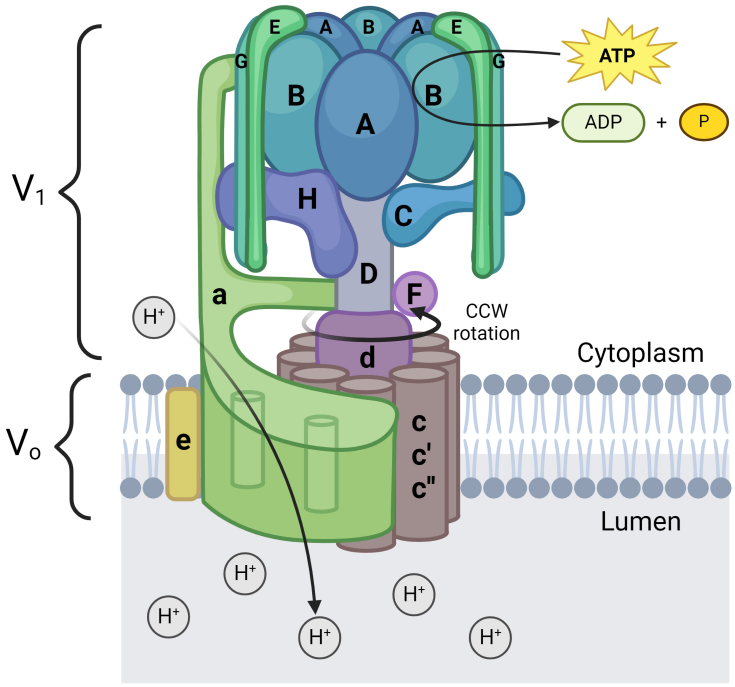

Figure 5.1: Structure of vacuolar-type ATPase (V-ATPase). Fully-assembled, functional V-ATPase is composed of the V_1 domain, located in the cytosol of the cell, and V_o, which is anchored in the membrane. As ATP hydrolysis occus within the A_3B_3 hexamer, resistance is applied from three EG stalks, C, H, and A subunits. The central stalk (D, F, d and c/c'/c" proteolipid ring) then rotates. Proteolipid ring rotation relative to subunit a causes proton transport through the hemichannels via cascading protonation and deprotonation of glutamate residues in the ring and arginine residues in subunit a.

build a strong foundation for continued investigation of feeding BAPC-dsRNA complexes as a potential pest control strategy for voracious *S. frugiperda* larvae.

5.2 Results and Discussion

5.2.1 Effect of Increasing BAPC concentration on *S. frugiperda* larval feeding behavior

We first explored if supplementing larval diets with BAPC solutions resulted in any change in feeding behavior resulting in changes to larval growth. In addition to physiological resistance mechanisms such as enhanced detoxification and target site mutations, insects can develop behavioral adaptations that allow them to detect and avoid toxic substances before exposure occurs, thus reducing the effectiveness of control strategies. The aversion of pesticide-treated areas is a behavioral pattern that is often overlooked as a mechanism contributing to pesticide resistance[21]. This aversion can be mediated by visual stimuli and chemosensory mechanisms, where gustatory and olfactory receptors detect harmful compounds, triggering avoidance behaviors[217, 218, 219, 220]. If BAPCs trigger these chemosensory or gustatory mechanisms, larvae may decrease consumption or relocate to untreated areas. Over time, these avoidant populations may become naturally selected, resulting in an increased frequency of individuals avoidant to or capable of chemosensory detection of BAPCs, ultimately leaving BAPCs in the same resistance cycle as current pesticides. Thus, including behavioral avoidance in addition to molecular resistance mechanisms is crucial for developing pest management strategies and underscores the need for enhancing treatment palatability and/or identifying detection thresholds.

To elucidate how *S. frugiperda* larvae respond to consuming BAPCs (without dsRNA), second instar larvae were fed daily with a range of BAPC concentrations. For 7 days, larvae were weighed and fed fresh diet supplemented with BAPC solutions ranging from 20 - 200 μM, while the control group was only supplemented with water. Larvae fed BAPC concentrations $\leq$ 40 μM showed no significant reduction in overall weight gain compared

control subjects (**Figure 5.2**). However, aversion to higher concentrations began as early as day 3 for 200 μM BAPCs and continued to accumulate throughout the study, ultimately resulting in a highly significant reduction in body mass compared to larvae not fed BAPCs (**Figure B.8**). Lower BAPC concentrations ($<$ 100 μM) did not strongly impact larval growth, with only moderate significance seen in 60 and 80 μM, and no body mass difference in 40 μM groups. Thus, 40 μM BAPCs was determined to be the aversion threshold, and thus the most suitable condition for feeding of BAPC-dsRNA complexes. Pilot studies using BAPC-dsRNA complexes to silence genes in red flour beetles and aphids also utilized 40 μM BAPCs, potentially indicating similar detection thresholds across insect orders[59]. These are the first results to show that a detection threshold at which larva are able to detect BAPCs exists, likely $\geq$ 100 μM, suggesting BAPCs may activate some chemosensory or gustatory stimuli at higher concentrations.

5.2.2 Survival of *S. frugiperda* larvae fed BAPCs complexed with dsRNA targeting V-ATPase subunits

To evaluate the effectiveness of BAPC-dsRNA complexes to cause lethal RNAi, *S. frugiperda* larvae were fed BAPCs complexed with 1μg of dsRNA against one of V-ATPase subunit A (V_A-dsRNA, 387 bp), B (V_B-dsRNA, 408 bp), or D (V_D-dsRNA, 204 bp) (sequences listed in **Table B.3**). V-ATPase subunits A and B were recently established by Bai et al. as effective RNAi targets[2]. This study utilized the most effective sequences from their work, which target the central region of mRNA transcripts. Additionally, a similarly designed sequence targeting subunit D was used. No research has currently been done on the silencing of this subunit in *S. frugiperda*. Additionally, Bai et al. utilized baculovirus injections to deliver the dsRNA[2]. While this method may be efficient for bench-top experiments, injections are not a realistic method for field studies, and concerns such as unintended spread, viral mutation, and antiviral immune responses create a need for non-viral delivery methods.

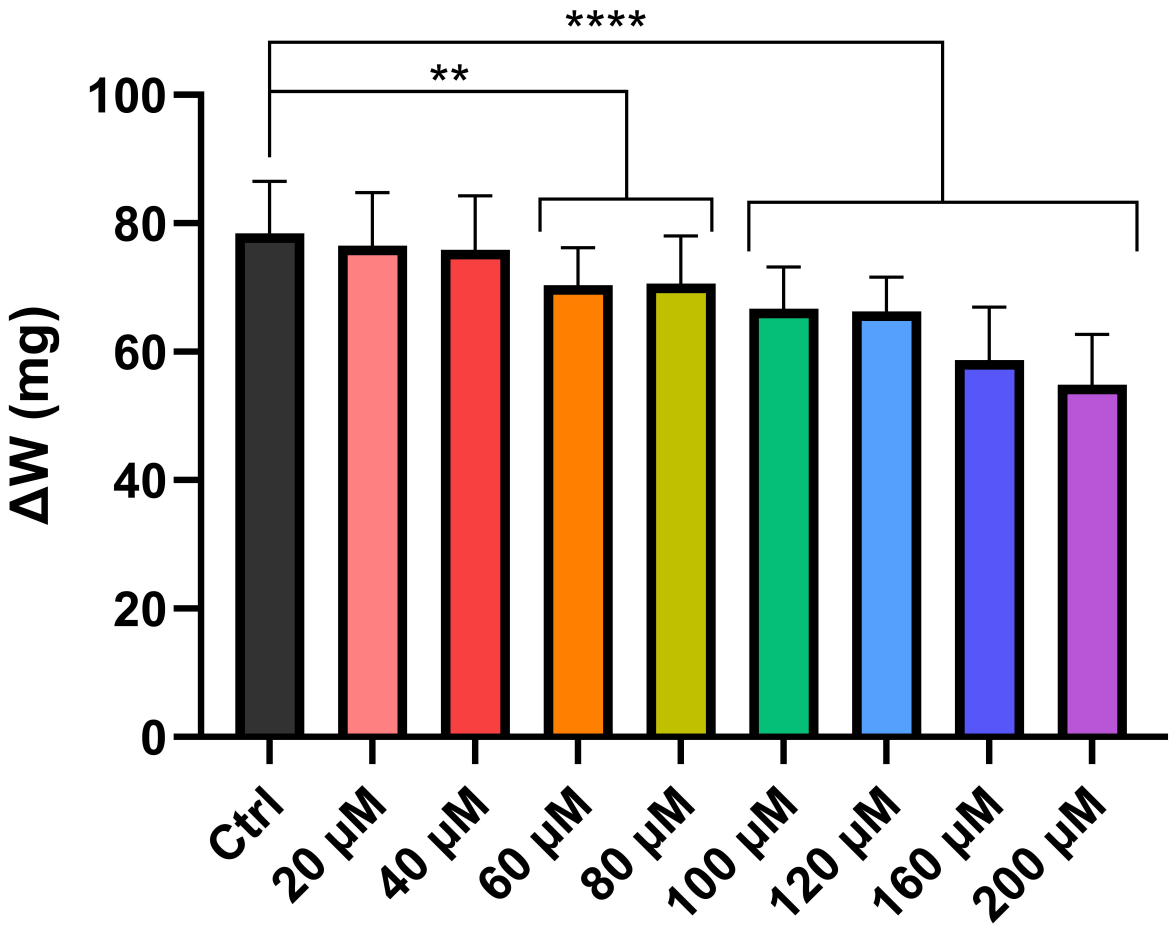

Figure 5.2: Overall change in larval weight resulting from BAPCs consumption over one week. *S. frugiperda* larvae beginning at third instar (n = 20) were fed 50-100 mg of gelled wheat/soy protein diet supplemented with BAPCs (0, 20, 40, 60, 80, 100, 120, 160, or 200 μM) and weighed each day for 6 days. Ctrl = diet supplemented with deionized H_2O. Data represent mean values +SD. Statistical significance: (**) $p < 0.002$; (****) $p < 0.0001$; (ns) $p > 0.12$ versus control group or as indicated in the bars (ANOVA, Dunnett posttest).

Kaplan-Meier survival analysis of third instar *S. frugiperda* larvae fed BAPC-dsRNA complexes (**Figure 5.3**) clearly demonstrates that larvae feeding BAPC-dsRNA complexes targeting V-ATPase subunits exhibited significantly reduced survival rates compared to diet treated with water, free V-ATPase-dsRNA, or non-specific dsRNA against *Candida albicans* EFG-1 (NS-dsRNA or NS+BAPCs). While control groups (H_2O, BAPCs alone, NS-dsRNA, and NS+BAPCs) maintained nearly 100% survival throughout the experiment, larvae fed with BAPC-dsRNA targeting V-ATPase subunits, particularly V_B and V_D, experienced a marked reduction in survival (55% and 62.5% survival, respectively). The observed difference in lethalities resulting from the BAPC+V_A and BAPC+V_B groups contrasts the results of baculovirus-mediated delivery, where similar lethalities were seen in these groups. However, studies in *Tuta absoluta*, another lepidotperan pest, demonstrated that silencing of V_B though feeding of 500 bp dsRNA added to tomato leaves resulted in increased mortality compared to V_A, showing that silencing efficacy may be highly dependent on specific dsRNA delivery method or sequence[221, 222].

The V_1 domain A_3B_3 hexamer contains ATP binding sites at the interface of each AB pair. Hydrolysis provides energy that results in counterclockwise rotation, thus converting chemical energy to physical potential. Sequence and structural analysis subunits in yeast revealed that subunit A is responsible for nearly all catalytic activity, while subunit B primarily contains nucleotide binding sites, and thus plays a non-catalytic, regulatory role[223, 224]. The variable mortality rates resulting from RNAi of V_A and V_B may be indicative that delivery mechanisms play an essential role in silencing. For example, while Bai et al. saw nearly equivalent results after injection of dsRNA-containing baculovirus, this work and Ramkumar observed increased mortality in V_B groups via oral delivery. A clear difference between the two is exposure to the alkaline gut environment, where secondary structures created by V_A sequences may create areas of vulnerability, even when complexed to BAPCs.

Unsurprisingly, feeding of free dsRNA resulted in non-significant mortality ($\leq$15%) for all sequences. The generally non-lethal result of feeding free dsRNA demonstrates why

carriers, such as BAPCs are crucial for efficient RNA delivery[206]. When complexed with BAPCs, all groups experienced significant mortality, thus exemplifying the effectiveness of nanoparticle-mediated delivery systems in overcoming these barriers associated with oral RNAi. The results both corroborate previous findings in red flour beetles, aphids, and even pilot studies in cockroaches, thus providing strong evidence that BAPC-dsRNA formulations could serve as a promising RNAi-based bio-pesticide strategy against the fall armyworm and a variety of other pests[59, 225].

To understand impact of diet composition on survival rates, this was repeated with changes in diet. Instead, *S. frugiperda* larvae (n = 20) were also fed corn leaf disks and filter paper discs until either all subjects had perished or pupated. Interestingly, larvae fed with BAPC-dsRNA complexes on corn leaf discs exhibited reduced but similar survival trends to those fed on the gel diet, confirming the feasibility of this approach under more natural feeding conditions (**Figure 5.5, top**). Furthermore, when provided with filter paper treated with BAPC-dsRNA complexes, larvae exhibited rapid mortality, likely due to starvation rather than dsRNA toxicity (**Figure 5.5, bottom**). This suggests that nutritional composition plays a critical role in studying RNAi efficacy, as larvae may reject non-preferred food substrates, reducing ingestion of the dsRNA treatment. Future studies should explore alternative delivery methods, such as soaking of plant tissue or editing BAPC formulation to act as a feeding stimulant. Importantly, to improve species specificity (thus potentially efficiency) and minimize unintended ecological consequences resulting from off-target delivery, future research should identify and target *S. frugiperda*-specific genes essential for survival or development.

Changes in larval physiology were also observed in groups fed BAPC-dsRNA complexes. Mortality was first observed in larva treated with BAPC-V_B and BAPC-V_D complexes on day 5, followed by BAPC-V_A complexes on Day 6. After death, some larvae were collected and photographed due to their unique appearance. **Figure 5.4A shows two larvae from each BAPC-dsRNA complex group that died next to an alive, control group**

larva. Most notably, death resulting from BAPC-V_B (middle group) appears to have occurred during molting, as evidenced by the molt, which the dark coloration seen only on the bottom half of the larva, also shown in Figure 5.4B (right). Though no accounts could be found documenting this in Lepidoptera, this effect has been noted in the cockroach *Periplaneta fuliginosa*[225]. The first larva shown in the group fed BAPC-V_A complexes appears to be swollen Figure 5.4B (left), while the second **Figure 5.4B (middle)** appears similar to both larva in the group fed BAPC-V_D complexes. This also suggests mortality occurs during molting as it was observed that prior to molting, larvae will swell their bodies which may be to loosen the cuticle to prepare for shedding. Additionally, effects from pupation were largely seen in larvae fed BAPC-V_B complexes, where several pupa were malformed**Figure 5.4C**. These observations were only noticed within a small number of pupa, and a large majority hatched into seemingly healthy adults, however, a systematic study of this is required for any definitive conclusions.

5.2.3 Validation of gene Knockdown in *S. frugiperda* larvae

Analysis of V-ATPase B transcript levels in larvae fed either BAPCs, free V_B-dsRNA, or BAPC-V_B complexes was done using larva fed for either 24 h (one feeding), 48 h (two feedings), or 72 h (three feedings) (**Figure B.9**. Four biological replicates of 4 insects each (total 16 insects used per treatment) were analyzed using 2-step RT-qPCR. At 24 h, both free dsRNA and BAPC-V_B complexes showed a small but significant degree of down-regulation, indicating successful RNAi (**Figure 5.6, left**). However, by 48 h (two feedings), transcript levels returned to near-basal levels, which would generally indicate only transient silencing(**Figure 5.6, middle**). However feeding of BAPC-V_B complexes for 72 h (three feedings) resulted in large up-regulation of V_B transcript levels (**Figure 5.6, right**). This may imply that when subjected to long-term exposure to dsRNA, alternative pathways may become activated and result in a "rebound" effect which causes up-regulation above

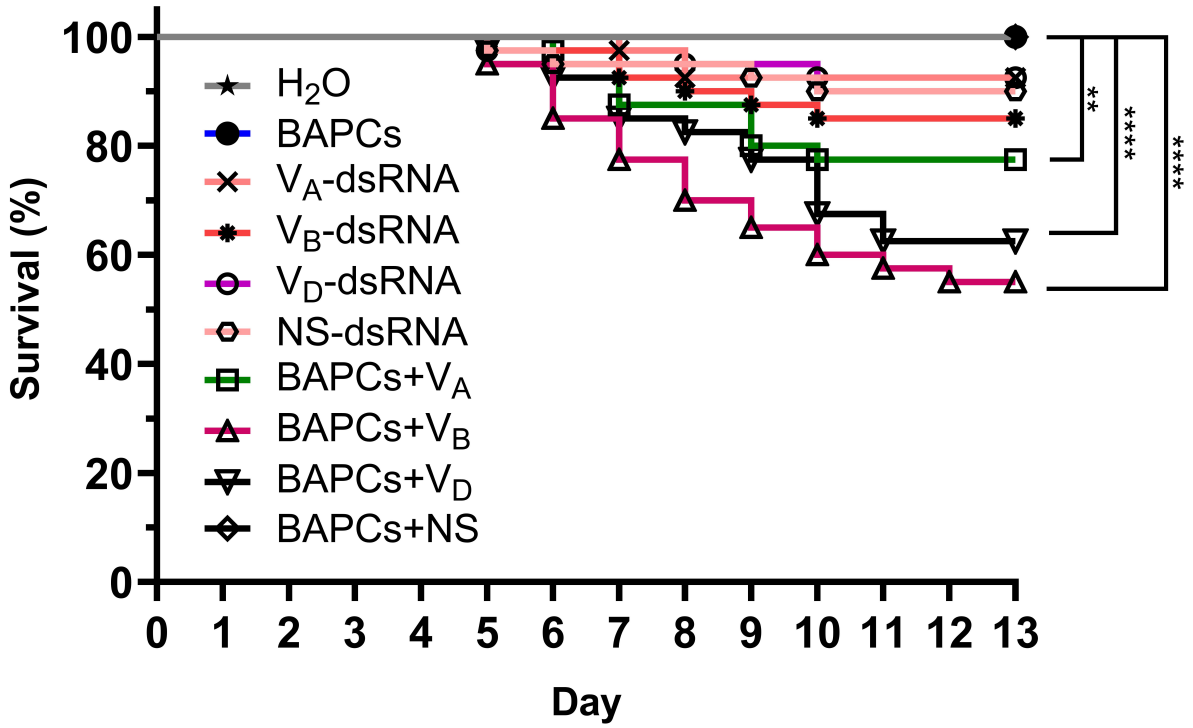

Figure 5.3: Survival analysis of *S. frugiperda* fed BAPC-dsRNA complexes on a standard laboratory gelled weat and soy protein diet. Diets of third instar *S. frugiperda* larvae (n = 40) were supplemented with H_2O, 1μg free dsRNA, or 40 μM BAPCs complexed with 1 μg dsRNA. Observations ended following the pupation and/or mortality of all subjects. Data represent mean values +SD. NS = non-specific dsRNA. Statistics: (**) $p < 0.002$; (****) $p < 0.0001$; (ns) $p > 0.12$ versus control group (H_2O) (ANOVA, Dunnett posttest).

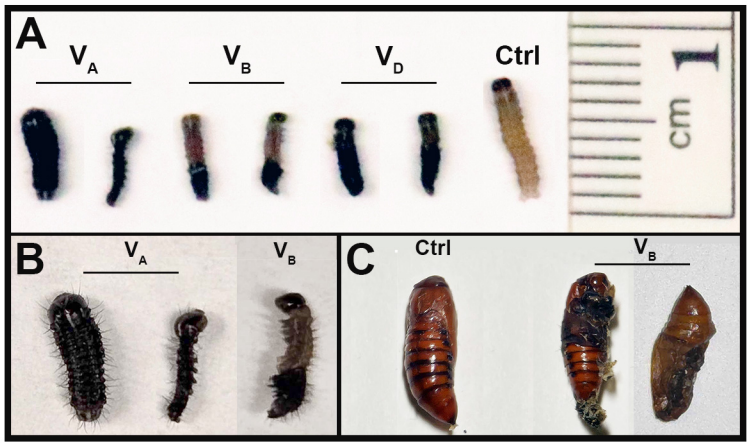

Figure 5.4: Physical differences seen in larvae successfully killed via feeding of BAPCs complexed with dsRNA against the A, B, or D subunits of V-ATPase. (A) Two larvae from each BAPC-dsRNA group compared to a control larvae on day 6 of feeding (1 cm ruler for scale). (B) Close-up comparison of larvae fed BAPC-V_A and BAPC-V_B. (C) Observed pupa malformation in larvae fed BAPC-V_B complexes.

normal levels. A similar effect has also been observed in similar preliminary studies in the American cockroach. These results, combining with the significant mortality resulting from the feeding study, suggests that the over-expression of V-ATPase B transcripts. Research on the effect of silencing the constituents of the A_3B_3 hexamer are incredibly limited, though two main mechanisms this rebound effect are hypothesized. First, the initial silencing of V_B, as seen at 24 h, kick-starts an alternative pathway which results in the over production of V_B transcripts. The overabundance of this transcript may result in increased production of the V_B subunit proteins, which may 1) create an imbalance in A:B availability for the V_1 A_3B_3 hexamer formation, or 2) overburden protein synthesis machinery, thus reducing the availability of ribosomal subunits to bind V_A transcripts.

5.3 Conclusions

This work showcases the first demonstration of BAPCs complexed with dsRNA as a potential bio-pesticide in *S. frugiperda*, or the fall armyworm. Our findings show that BAPCs fed at concentrations over 100 μM result in feeding aversion, thus establishing a potential

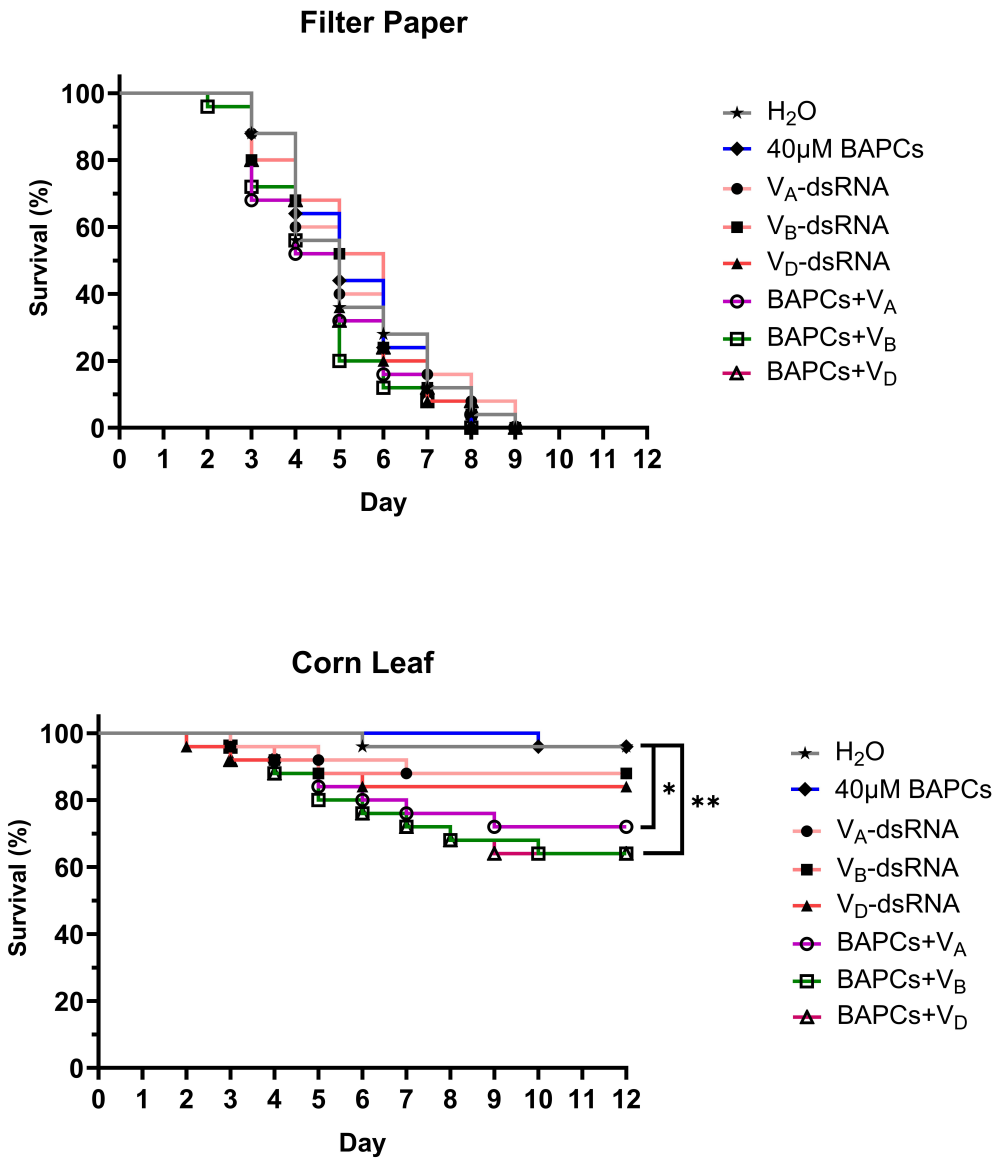

Figure 5.5: Survival analysis of *S. frugiperda* fed BAPC-dsRNA complexes on corn or filter paper. Third instar *S. frugiperda* larvae (n = 20) were fed either fresh corn leaf discs (top) or filter paper discs (bottom) supplemented with H_2O, 1μg free dsRNA, or 40 μM BAPCs complexed with 1 μg dsRNA. Observations ended following the pupation and/or mortality of all subjects. NS = non-specific dsRNA. Data represent mean values +SD. Statistics: (*) $p < 0.033$; (**) $p < 0.002$; (ns) $p > 0.12$ versus control group or as indicated in the bars (ANOVA, Dunnett posttest).

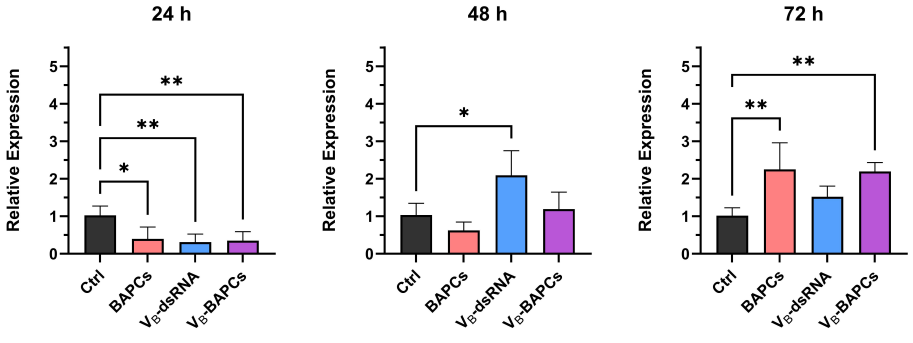

Figure 5.6: qPCR analysis of V-ATPase B (V_B) expression in *S. frugiperda* larvae at 24, 48, and 72 h post-treatment with V_B-dsRNA and V_B-BAPCs, thus receiving one, two, and three feedings, respectively. Control subjects were treated with water. Data represent mean values +SD of four biological replicates containing four subjects each run in technical triplicate. Actin was used as the reference gene. Statistical significance: (*) $p < 0.033$; (**) $p < 0.002$; (ns) $p > 0.12$ versus control group (ANOVA, Dunnett posttest).

treatment threshold, with 40 μM showing no affect on feeding behavior. Larvae fed BAPCs complexed with dsRNA against V-type ATPase subunits A, B, and D all exhibited significantly reduced survival compared to control groups, confirming that nanoparticle-mediated RNAi enhances gene silencing efficacy. Specifically, targeting V-ATPase B and V-ATPase D subunits led to the most pronounced mortality effects, highlighting their essential role in larval survival. However, despite the initial success in gene knockdown observed at 24 hours post-treatment, gene expression levels rebounded by 48 and 72 hours, suggesting either a transient silencing effect or compensatory gene regulation mechanisms.

Furthermore, feeding experiments conducted on corn leaves yielded similar results to the gel diet, supporting the feasibility of deploying BAPC-dsRNA complexes in field applications. However, when larvae were presented with dsRNA on filter paper, rapid mortality occurred, likely due to aversion and starvation rather than RNAi effects, underscoring the importance of both diet formulation and delivery methods in effective pest control strategies. These observations suggest that while RNAi-based approaches hold promise, enhancing palatability and delivery within an agricultural context is a crucial consideration.

Given the highly conserved nature of V-ATPase across species, future studies should explore targeting more organism-specific genes to minimize off-target effects, such as mortality of non-target insects and beneficial species. Additionally, refining nanoparticle formulations to prolong RNAi effects and investigating potential resistance mechanisms will be crucial in advancing BAPC-dsRNA complexes as a viable bio-pesticide. This study provides a foundation for the development of next-generation RNAi-based pest control solutions, with implications for sustainable management of *S. frugiperda* and other insect pests.

5.4 Acknowledgments

I would like to thank Amelia Williams and Jake Tatum from Dr. Kate Buckley's lab for their guidance and knowledge of qPCR. Additionally, I would like to thank Chad Finkenbinder from Benzon Insects for his continued support and knowledge of *S. frugiperda* rearing and development. Finally I would like to thank Collin Wall for his help in peptide synthesis and purification necessary for BAPC formation.

5.5 Materials and Methods

5.5.1 Insect rearing

S. frugiperda (fall armyworm) eggs placed in individual growth containers or communal cups were obtained from Benzon Research (Carlisle, PA, USA). Larvae were reared on a provided gel wheat germ and soy flour-based artificial diet in a growth chamber at room temperatures ($\sim$ 22 °C) with a 12:12 (L:D) photoperiod. Larvae were grown until reaching second instar transferred into a 60 mL cup and fed with 50 mg pieces of gelled diet. This was done to prevent excessive loss of treatment which would be a likely result of adding it to large quantities of diet.

5.5.2 Synthesis of BAPCs and formation of BAPC-dsRNA complexes

The peptides (Ac-FLIVI)$_2$-K-K$_4$-CONH$_2$ and (Ac-FLIVIGSII)$_2$-K-K$-$4-CONH$_2$ were synthesized using solid-phase peptide synthesis Fmoc chemistry. Finished peptides were then purified via ether precipitation and high-pressure liquid chromatography (HPLC). Briefly, 10-40 mg of crude peptide were loaded into a Zorbax C18 semipreparative RP-HPLC column. A linear AB gradient (1% ACN/min for 30 min, followed by 0.1% ACN/min for 150 min, followed by 1% ACN/min for 30 min) at a flow rate of 2 mL/min at room temperature, where eluent A is 0.76% aqueous TFA, pH 2, and eluent B is 0.76% TFA in ACN. Samples eluted during the 0.1% gradient and confirmed via MALDI-TOF mass spectrometry. Peptide concentration was determined by dissolving each separately in 2'2'2'-trifluoro-ethanol (TFE) and measuring phenylalanine absorbance (257.5 nm). Absorbance was divided by two, as each sequence contains two residues. The peptides are monomeric in TFE, ensuring thorough mixing when combined. Stock solutions of 100 μM in 1 mL were created by mixing equimolar ratios of each peptide in a 1:1:1 solution of acetonirile:TFE:H_2O and then lyophilized via centrifugal evaporation. Nuclease-free water was then added to rehydrate the peptides, spurring self-assembly of the nanocapsules driven by hydrophobic interactions. Solutions were incubated at RT for 10 min, then placed at 4 °C for at least 1 h to lock BAPC conformation and prevent continued growth.

5.5.3 Formation of BAPC-dsRNA complexes

To create the BAPC-dsRNA complexes that were fed to insects, working solutions of 40 $/mu$M (20 μL final volume) were created from the 100 μM stock. Next, 1 μg of dsRNA targeting V-ATPase subunits A, B, or D suspended in duplex buffer (Integrated DNA Technologies), and complexes were incubated at RT for at least 30 min, after which they were promptly added to insect diet. Fresh complexes were created each feeding day.

5.5.4 *S. frugiperda* RNA extraction and cDNA synthesis

Total RNA was extracted from 100 mg of *S. frugiperda* larvae at sixth instar for dsRNA synthesis or at the indicated time point for qPCR analysis using TRIzol (Invitrogen; Carlsbad, CA, USA). RNA was quantified via NanoDrop and analyzed by electrophoresis in 1% denaturing agarose gels in TAE buffer. Around 1 μg of total RNA was treated with RQ1 RNase-free DNase (Promega) according to manufacturer's instructions (37 °C for 30 min, with the reaction stopped by adding RQ1 Stop Solution and heating to 65 °C for 10 min). One to 1.5 μg of DNase-treated RNA samples was then reversed transcribed following manufacurer protocol in a total reaction volume of 20 μL (500 μM of each dNTP, 2.5 μM oligo dT, 5 mM DTT and 200 U SuperScript II (Invitrogen)).

5.5.5 dsRNA synthesis

Sequences for V-ATPase subunits A and B were used from the work of Bai et al (**Tables B.2 and B.3**).[2] The sequence targeting subunit D was designed by first obtaining the mRNA sequence NCBI nucleotide database (MT707617.1). This was further screened through GenScript siRNA target finder tool to predict siRNA sequences, with preference given to sequences most in the middle of the transcript, which was selected for dsRNA synthesis.Primers

5.5.6 Feeding of BAPCs, free dsRNA, or BAPC-dsRNA complexes

For all feeding studies, food was withheld overnight prior to the beginning of each feeding experiment, and every subsequent day, any remaining diet was removed and a fresh 50 mg portion of diet was added to each larval cell. For aversion assays, each subject (n = 20) was first weighed, then 20 μL of 20, 40, 60, 80, 100, 120, 160, or 200 μM BAPCs without dsRNA were added to the surface of the diet portion. For gene silencing assays (n = 40), 20 μL of 40 μM BAPCs + 1 μg dsRNA against V-ATPase A, B, or D was added to the surface of the diet portion. The same protocol was followed for experiments using corn

leaf discs (n = 20) and filter paper discs (n = 20). Observations continued for all subjects until either death or pupation, and five organisms from each feeding group were observed until eclosion. For RT-qPCR, 16 total larvae (4 insects per replicate, 4 replicates) for each treatment were fed for either 1, 2 or 3 days, corresponding to 1, 2, or 3 feedings, respectively (see **Figure B.9**). Each group was harvested on the appropriate day for RNA extraction and cDNA synthesis. All feeding experiments used water as the no treatment control, and 500 bp targeting *Candida albicans EFG1* was used as the non-specific dsRNA in gene silencing assays.

5.5.7 Quantitative amplification of reverse transcribed V-ATPase B transcripts (RT-qPCR)

Once larvae were harvested at the appropriate time point, RNA extraction and cDNA synthesis were performed as just described, with the exception that the amount of total RNA used for cDNA synthesis was normalized to 1.5 μg. The resulting cDNA was diluted 1:30 with nuclease-free water so that RT-qPCR reactions contained 25 mg in 5 μL cDNA, 10 μL PerfeCTa SYBRGreen SuperMix (QuantaBio) and 0.5 μM each of gene-specific primer. Cycling was done starting at 50 ∘C for 2 min, then held for 10 min at 95 ∘C, folloed by 40 two-step cycles of 95 °C for 15 s and 60 °C for 1 min in an Applied Biosystems 7500 Real Time PCR System machine. Reactions for each biological replicate was run in technical triplicate. β-actin was used at the reference gene, and fold-changes were calculated using the$\Delta\Delta C_T$ method.

5.5.8 Statistics and software

Statistics were performed using GraphPad Prism 5 software (GraphPad Software, La Jolla, CA). Figures were created using biorender.com and Adobe Photoshop CC 2025.

Chapter 6

Conclusions

This dissertation presents the development and optimization of two distinct nanoparticle-mediated RNA delivery systems designed to overcome biological resistance mechanisms in both fungal and insect species. By leveraging gold nanoparticle (AuNP)-mediated photoporation in yeast and branched amphiphilic peptide capsules (BAPC)-mediated dsRNA delivery in the fall armyworm (Spodoptera frugiperda), this work contributes to the advancement of RNA interference (RNAi)-based strategies as potential alternatives to traditional antifungal and insecticidal treatments.

To explore RNAi as an alternative antifungal, the first AuNP-mediated photoporation method was developed and extensively optimized for delivery into yeast organism. Initial optimization was performed in the model organism *Saccharomyces cerevisiae*. A Ti:Sapphire 800 nm laser (35 fs pulse) was used to photoporate cells, and results showed the use of 800 nm photons, which fall in the near infrared spectrum enable efficient delivery without compromising yeast cell viability.[154] To understand how AuNP-mediated photoporation affected more delicate, mammalian cells, Chinese Hamster Ovary cells were used. Conditions were chosen that took into account the viability loss of CHO cells while maximizing delivery into yeast. Since this was the first AuNP-mediated photoporation method to deliver molecules into fungal cells, several key parameters of both the laser and AuNPS needed to be optimized. Laser parameters of wavelength, fluence, and irradiation time were explored, and AuNP parameters primarily focused on AuNP size and concentration. Unlike other traditional physical delivery methods such as electroporation, the transient nature of the pores formed during photoporation preserve cell viability. After determining optimal irradaiton conditions set optimal concentrations to be irradiation at3.6 mJ/cm^2 for 10 min using 4 x 10^{10} AuNP/mL of 50 nm AuNPs, however a test of these conditions ustilizing nanorods instead of nanospheres clearly demonstrated that changing AuNP shape would

require re-optimization. Using gold nanospheres at the optimal conditions, *Candida albicans* was photoporated in the presence of siRNA targeting the virulence gene *EFG1*, an essential regulator of hyphal transition and virulence ,representing the first work to attempt fungal RNAi with photoporation. The successful delivery of fluorescently labeled siRNA with ¿90% efficiency demonstrated the method's capability to introduce large, biologically active molecules into fungal cells. Excitingly, functional validation of *EFG1* knockdown was quantified through RT-qPCR was achieved in *C. albicans*, thereby confirming the effectiveness of photoporation for RNAi-based antifungal applications. This study represents the first instance of AuNP-mediated photoporation optimized for yeast, offering a foundation for future research on nanoparticle-assisted RNA delivery in fungal pathogens.

The use of BAPC-dsRNA complexes as a potential alternative to chemical pesticides was originally established by Avila et al. in previous studies using *Tribolium castaneum* (red flour beetle) and *Acyrthosiphon pisum* (pea aphid).[59] However the efficacy of RNAi varies strongly across insect orders, and this study only established proof-of-concept groundwork. This study is the first to study BAPC-dsRNA complexes in Lepidoptera, namely *Spodoptera frugiperda* (fall armyworm). *In vitro* studies in Sf9 cells revealed uptake primarily occurs through clathrin-mediated endocytosis or macropinocytosis. Surprisingly, BAPCs were not found highly localized in lysosomes, suggesting an escape mechanism or direct cytosolic delivery. Additionally, the potential involvement of transcytosis in the uptake and systemic spread of BAPC-dsRNA complexes out of the gut was suggested, highlighting an important mechanistic factor in the success of oral RNAi treatments. To visualize these effects *in vivo*, an oral RNAi approach was developed to feed BAPCs or BAPC-dsRNA complexes to second instar *S. frugiperda* larvae. Observing how increasing BAPC concentration impacted larval feeding behavior lead to the first discovery of a potential threshold ($\geq$100 μM) at which BAPC concentration adversely affects feeding behavior and thus larval growth, a phenomenon that should also be explored in other insect orders. Additionally, feeding BAPC-dsRNA complexes targeting V-ATPase subunits A, B, and D resulted in significant larval

mortality but was most prominent when targeting subunit B. However, quantitative analysis of transcript levels unexpectedly revealed an initial down-regulation after 24 h of feeding, followed by a sharp up-regulation after 48 - 72 h. This may indicate *S. frugiperda* experience a compensatory up-regulation after silencing, which results in lethality if prolonged, however the mechanisms of this remain a mystery. Given the increasing resistance of *S. frugiperda* to conventional chemical pesticides, these findings reinforce the promise of BAPC-mediated RNAi as an effective pest management tool and underline versatility of BAPCs as a pest management strategy in variety of potential insect pest targets.

Despite these successes, this study also highlights several challenges associated with nanoparticle-mediated RNA delivery. The structural and physiological differences between fungi and insects necessitate distinct delivery strategies, as demonstrated by the need for a physical delivery method (AuNP-mediated photoporation using fs laser pulses) in yeast, versus a chemical delivery method (oral delivery of BAPC-dsRNA complexes) in insects. Additionally, factors such as RNA stability, cellular uptake mechanisms, and delivery consistency present significant hurdles that must be addressed to fully realize the potential of RNAi-based interventions in real-world applications.

Ultimately, this research provides valuable insights into the development of nanoparticle-assisted RNAi delivery platforms, bridging the gap between laboratory-based gene silencing techniques and practical applications in both medicine and agriculture. Future studies should focus on refining delivery efficiency, stability, and scalability of these methods, with an emphasis on targeting additional virulence or resistance-associated genes. By advancing RNAi-based strategies through optimized nanoparticle carriers, this work contributes to the ongoing effort to develop sustainable, next-generation solutions for combating biological resistance in pathogens and pests.

Appendices

Appendix A

Supplementary Information for AuNP-mediated Photoporation Development and RNAi in Fungal Cells

EFG-1	
Seq. 1	CTGCTTTGGCTCCATCTTCTA
Seq. 2	ATGGACCAGATTCGTCGTATTC
Seq. 3	/56-Fam/TGTCTGGAT/Zen/TGGTGGTTCTATCTTGGC/3IABkFQ/
Actin	
Seq. 1	GGTCAGTATAATGCTCCTGGTAAG
Seq. 2	CAGCACCACCCTGGTAATAAT
Seq. 3	/Cy5/ACACCTGCATCACAACCAGGTTCT/3IAbRQSp

Table A.1: Primer probes used for qPCR analysis of *EFG-1* transcript levels and Actin as the housekeeping gene.

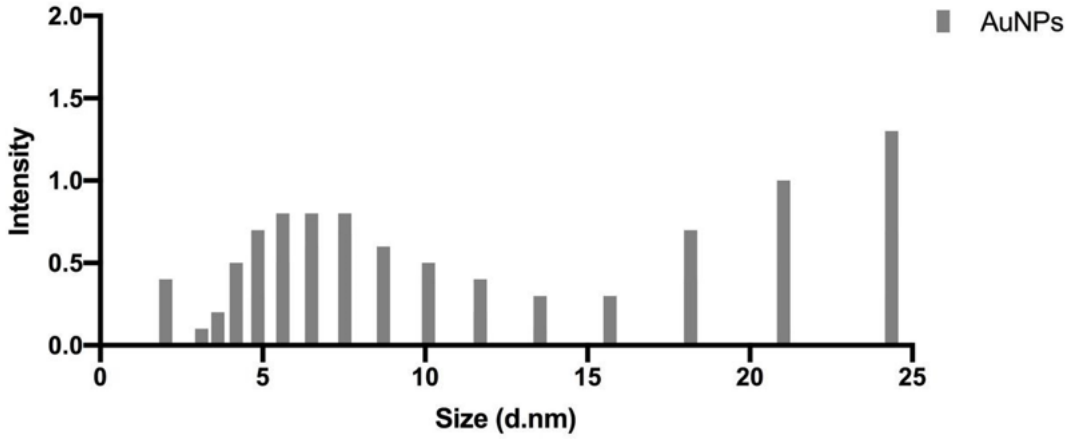

Figure A.1: Dynamic Light Scattering (DLS) analysis of AuNPs. DLS was performed in 10 mm path length cuvettes, and AuNPs were diluted 1:3 in distilled water to obtain better resolution.

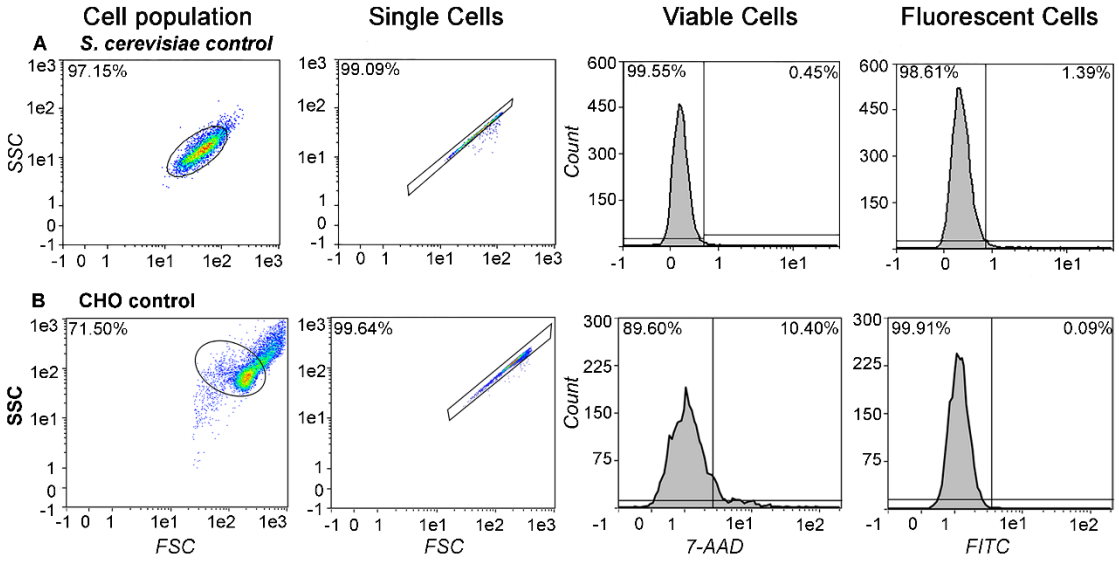

Figure A.2: Flow cytometry gating strategy for untreated S. cerevisiae and CHO cells. For this experiment, 1 x 10^7 *S. cerevisiae* cells/mL and 1 x 10^6 CHO cells/mL, were suspended in phosphate-buffered saline solution. Cells were expose to AuNPs (14 μM) and calcein (10 μM) but not to fs laser pulses. A) Flow cytometry gating strategy for *S. cerevisiae*. In the first step, selection of cell size by plotting SSC vs FSC, then exclusion of cell clumps and doublets by applying FSC-height vs FSC-area. Last two plots represent histograms to evaluate dead cells (7-AAD positive) and FITC auto-fluorescence. B) Same strategy applied to CHO cells.

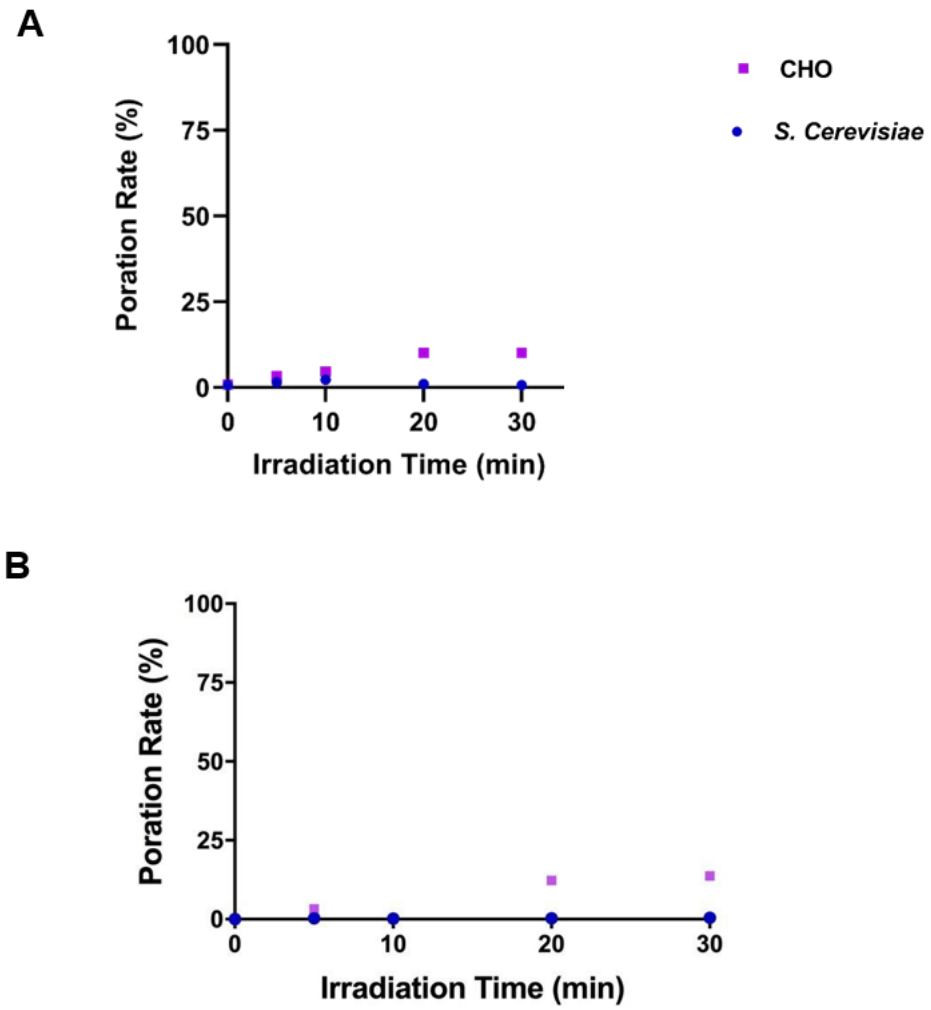

Figure A.3: Non-irradiated *S. cerevisiae* and CHO cells. A) *S. cerevisiae* (1 x 10^7 cells/mL) or CHO (1 x 10^6 cells/mL) were suspended in phosphate-buffered saline solution in the presence of AuNPs (14 μM) and calcein (10 μM) and incubated at room temperature for different times. B) *S. cerevisiae* (1 x 10^7 cells/mL) or CHO (1 x 10^6 cells/mL) were suspended in phosphate-buffered saline solution in the presence of calcein (10 μM) and incubated at room temperature for different times. Flow cytometry analysis was used to evaluate green fluorescence in both cases (calcein positives).

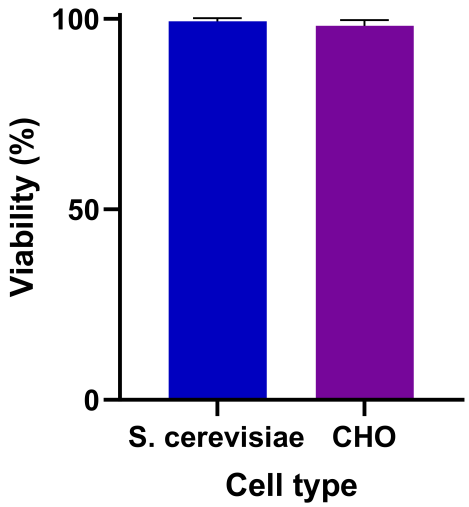

Figure A.4: Viability of non-irradiated *S. cerevisiae* and CHO cells. *S. cerevisiae* (1 x 10^7 cells/mL) or CHO (1 x 10^6 cells/mL) were suspended in phosphate-buffered saline solution in the presence of AuNPs (14 μM) and calcein (10 μM) and incubated at room temperature for 15 minutes. Flow cytometry analysis was used to evaluate viability using 7-AAD dye.

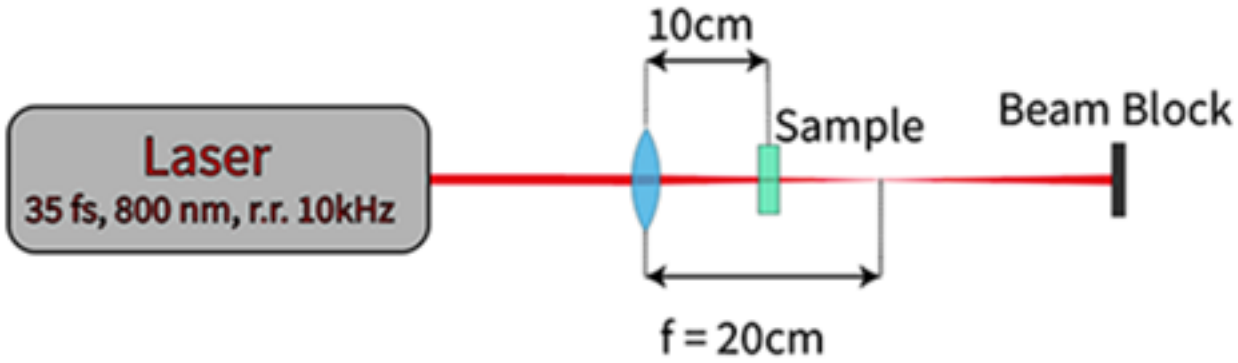

Figure A.5: Schematic of experimental setup for the irradiation of all samples. The sample cuvette was place in line with the 800 nm NIR laser with a pulse duration of 35 fs and repetition rate (r.r.) of 10 kHz. The cuvette was placed midway between the focusing lens, which was set to a maximum focal length of 20 cm, and the focal point

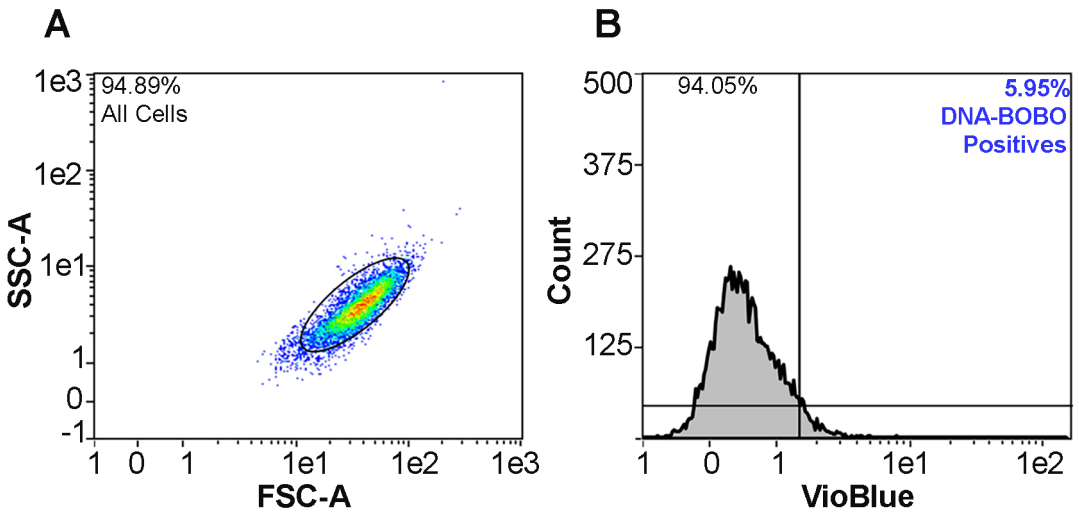

Figure A.6: Flow cytometry controls for non-irradiated *S. cerevisiae* exposed to DNA-BOBO and AuNPs. For this experiment, 1x 10^7 *S. cerevisiae* cells/mL were suspended in a phosphate-buffered saline solution. Cells were exposed to AuNPs (14 μM) and pDNA-BOBO™-3 Iodide (10 μg) but not to fs laser pulses. Cells were incubated for 10 minutes at room temperature. A) Flow cytometry gating of cell population by plotting SSC vs FSC. B) Fluorescence of non-irradiated cells after 10 minute incubation.

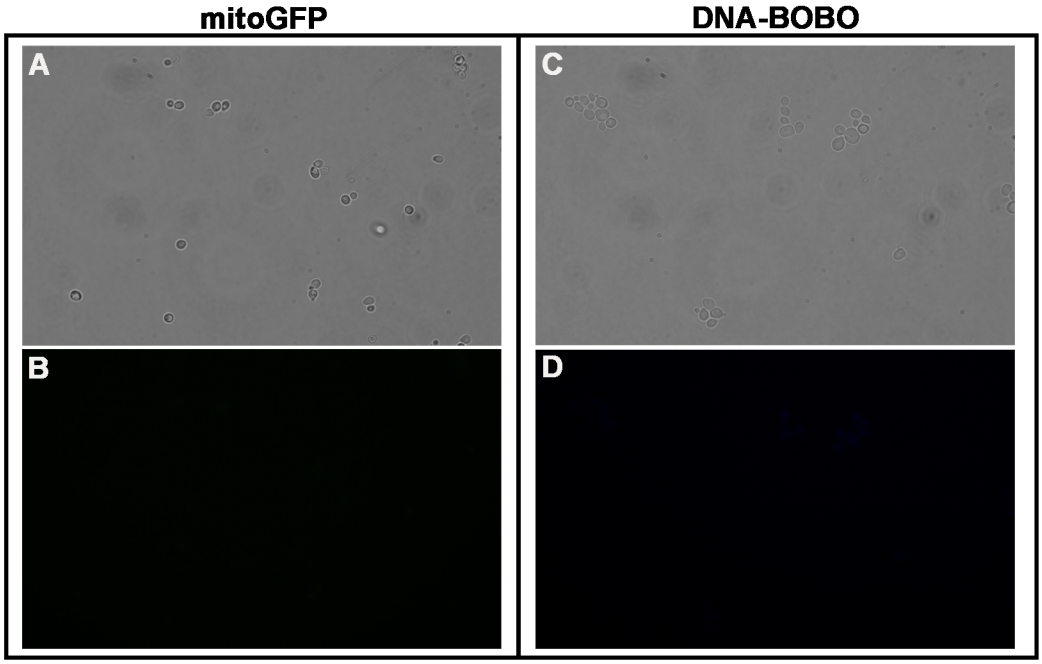

Figure A.7: Negative controls of plasmids tested in *S. cerevisiae S. cerevisiae* (1 x 10^7 cells/mL) were suspended in phosphate-buffered saline solution in the presence of AuNPs (14 μM) and mitoGFP plasmid or pDNA- BOBO™-3 Iodide and incubated at room temperature for 15 minutes (no exposure to fs laser pulses). A) Bright field micrograph to demonstrate integrity of the cells treated with mtGFP. B) Absence of mtGFP expression in *S. cerevisiae* subjected to fluorescence and phase contrast microscopy, FITC filter and C) Bright field micrograph to demonstrate integrity of the cells treated with pDNA-BOBO™-3 Iodide. D) Fluorescence micrograph showing no uptake of pDNA-BOBO™-3 Iodide.

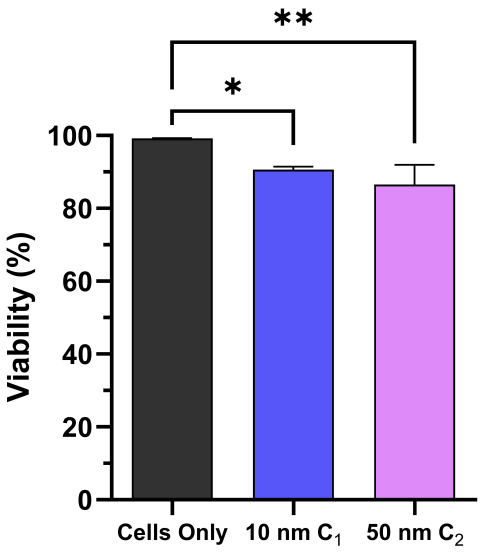

Figure A.8: Viability of *C. albicans* (1 x 10^7 cells/mL) photoporated with either 10 nm (8 x 10 ^{10}) AuNPs/mL or 50 nm (8 x 10 ^{10}) and 15 ng/μL ATTO550-siRNA. Ctrl = cells irradiated without AuNPs. Data represent mean values +SD of at least three experiments combined. Statistical significance: (*) p ¡ 0.0332; (**) p ¡ 0.0021 versus control group (ANOVA, Dunnett posttest).

Appendix B

Supplementary information for RNAi in *S. frugiperda* cells, tissue, and larvae.

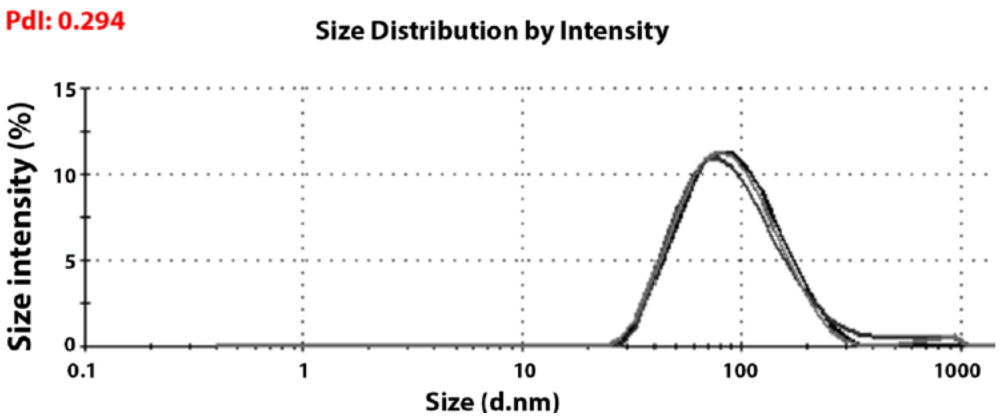

Figure B.1: DLS of BAPC-dsRNA complexes. Example size distribution of BAPCs (50 μM) associated with dsRNA (1 μg). Average size: 86.23 nm, and polydispersity index: 0.294.

Table B.1: Z-average hydrodynamic diameter and zeta potential (ZP) values obtained for Rh- BAPCs (50 μM) and Rh-BAPCs-dsRNA complexes (50 μM + 1 μg dsRNA). Values are presented in average ± standard deviation (n = 3).

Sample	Z-Average (nm)	ZP (mV)
Rh-BAPCs	86.5 ± 16.8	34.8 ± 1.3
Rh-BAPCs-dsRNA	97.4 ± 1.5	26.9 ± 5.4

Primers Sequence (5'-3')

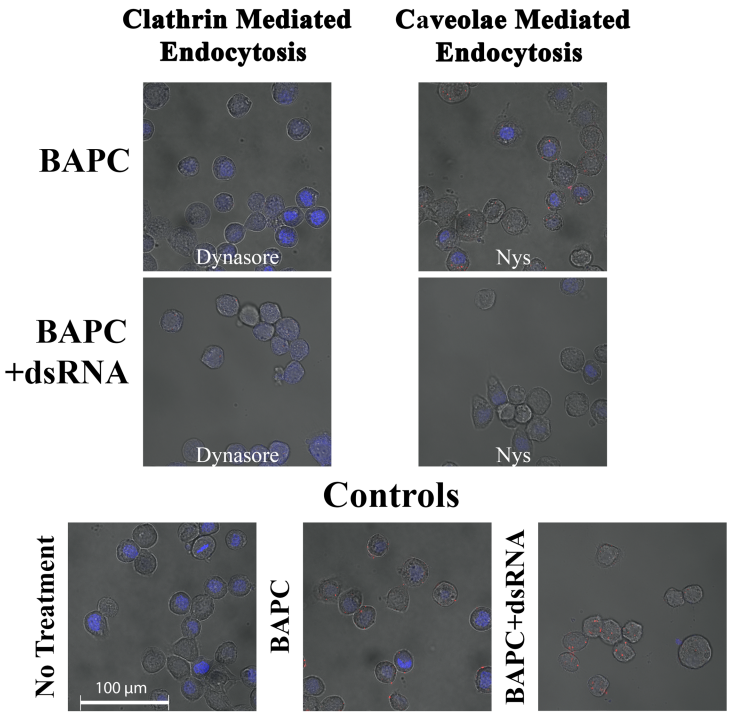

Figure B.2: Additional inhibitors used in the inhibition assay of BAPCs and BAPC-dsRNA complexes in Sf9 cells. Additional inhibitors were used to study uptake via clathrin- and caveolae-mediated endocytosis pathways. BAPCs were labeled with rhodamine B(red) and DAPI (blue). Each endocytosis inhibitor is shown in the presence of only BAPCs (upper panel) and BAPCs + dsRNA (lower panel). Results are comparable to results presented in the main text.

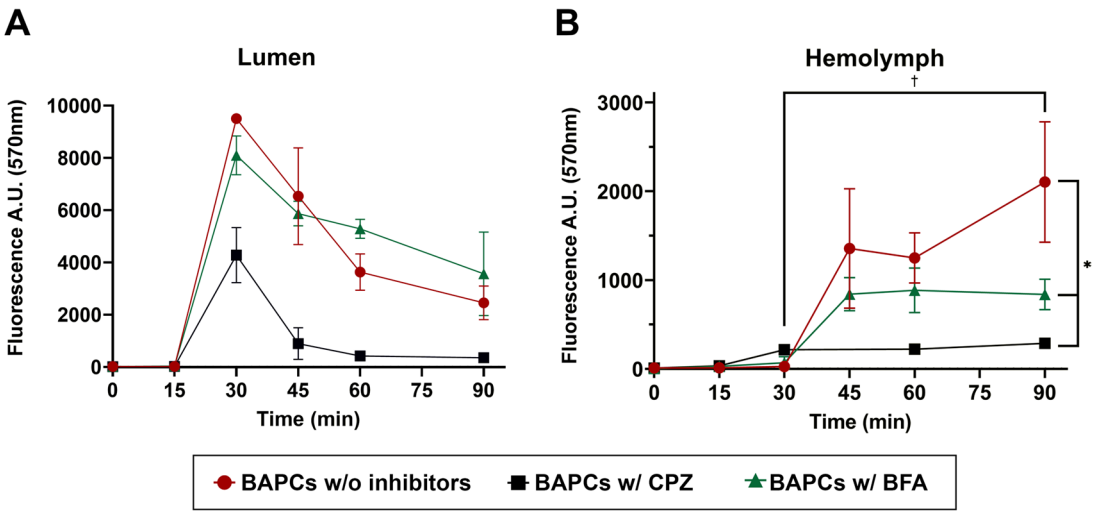

Figure B.3: Transcytosis of Rh-BAPCs through *S. frugiperda* midgut in the presence of transcytosis and endocytosis inhibitors. Tissues were equilibrated to the buffers for the first 15 minutes, then Rh-BAPCs were added. A) Relative fluorescence of lumenal buffer or B) hemolymph buffer over 1 hour. Data represent mean values +SD of two experiments combined. Statistical significance: (*) $p < 0.033$; (***) $p < 0.001$; (ns) $p > 0.12$ versus Rh-BAPC control (no inhibitors) or as indicated in the bars (ANOVA, Dunnett posttest). (†) $p < 0.033$; versus controls with no inhibitors (ANOVA, Tukey posttest).

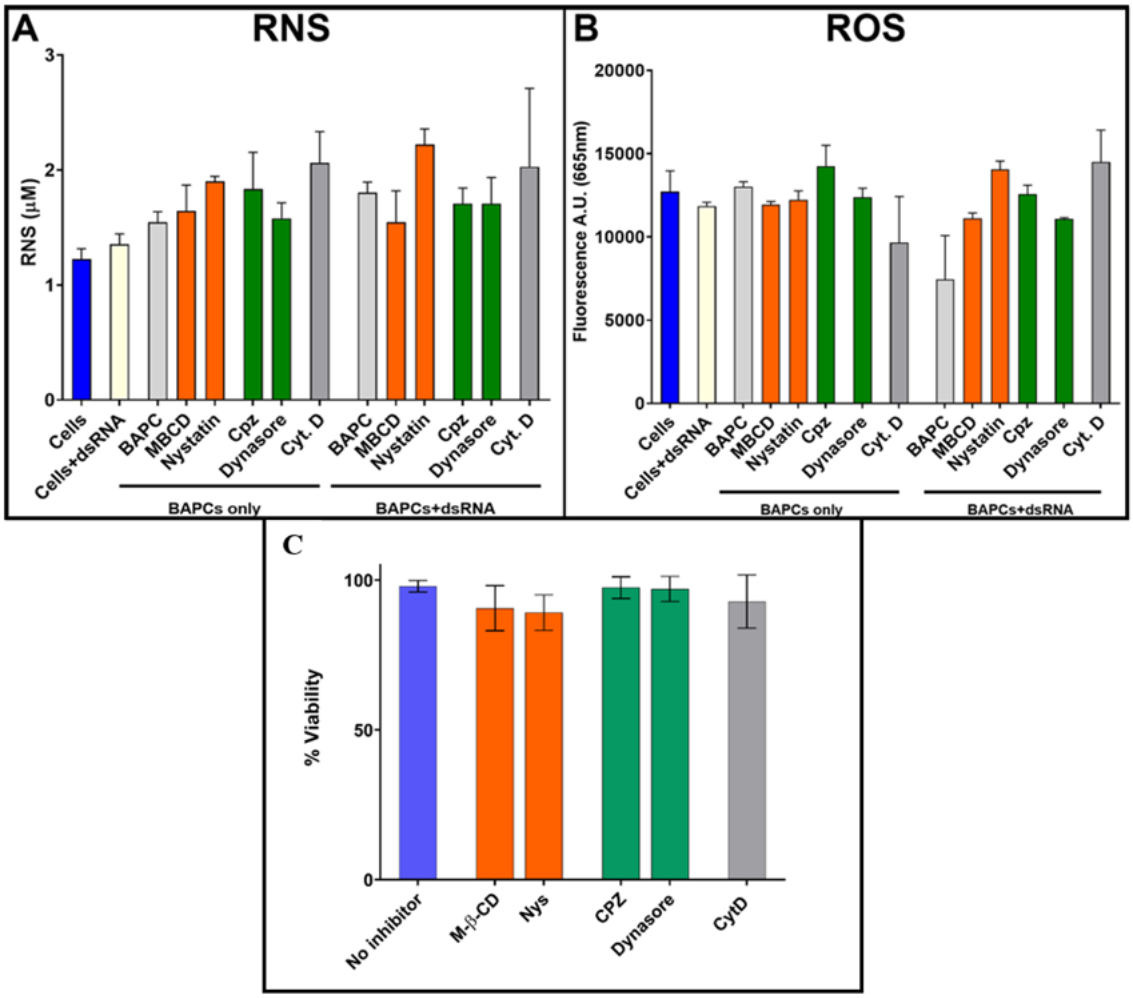

Figure B.4: SF9 cell viability assay with different endocytosis inhibitors. (A) and (B) The effect of endocytosis inhibitors on the production of reactive species. (C) Viability of SF9 cells using 7-AAD viability dye treated with endocytosis inhibitors. Concentrations tested: 5 mM M-β-CD, 50 μM Nystatin, 10 μg/mL CPZ, 80 μM Dynasore, or 4 μM Cytochalasin D and 50 μM BAPCs complexed with 1 μg dsRNA for 30 min.

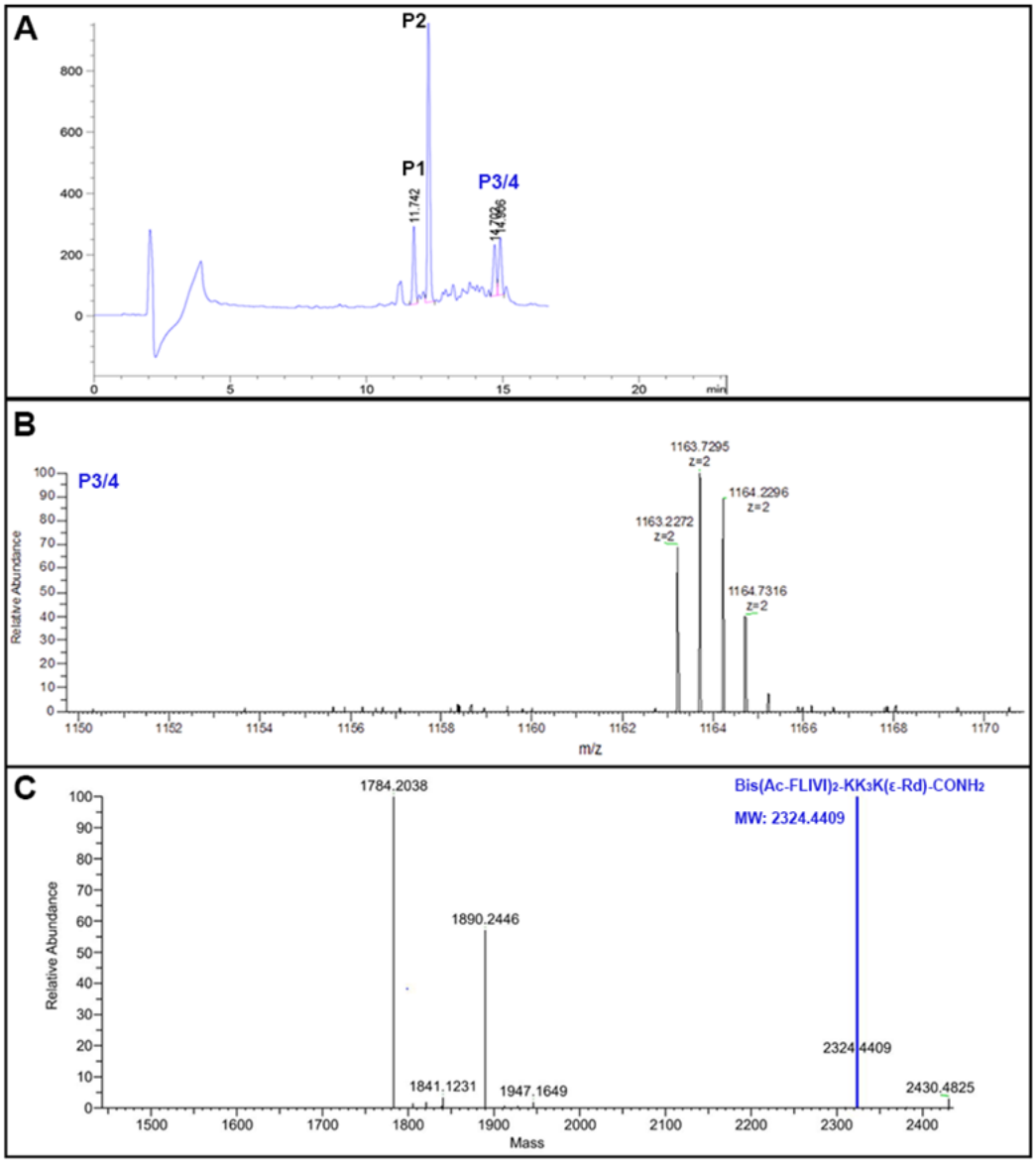

Figure B.5: RP-HPLC and MS analysis of the Rhodamine labeled peptide bis(Ac-FLIVI)2-KK4-CONH2. (A) RP-HPLC analysis of bis(Ac-FLIVI)$_2$-KK$_3$K(ϵ-Rd)CONH$_2$. The analysis was conducted using an analytical C18 column (Xterra, Sheild, 5 μm, 4.6 x 150 mm, 125 Å) and a gradient elution consisting of 0.1% formic acid in water (eluent A) and 0.1% formic acid in acetonitrile (eluent B). The flow rate was 1 mL/min, and absorbance was detected at λ = 220 nm. (B) Electrospray spectra of P3/4 (C) Deconvolution of the $[M+2H]^{2+}$ peak containing the expected mass for bis(Ac-FLIVI)2-KK3K(e-Rd)CONH2. Peptides were analyzed on a quadrupole orbitrap mass spectrometer P3/4 S9 (Orbitrap Explorus 120) and the peptide isotope patterns were deconvoluted with the Xtract Deconvolution algorithm in FreeStyle 1.8 software (Thermo Fisher).

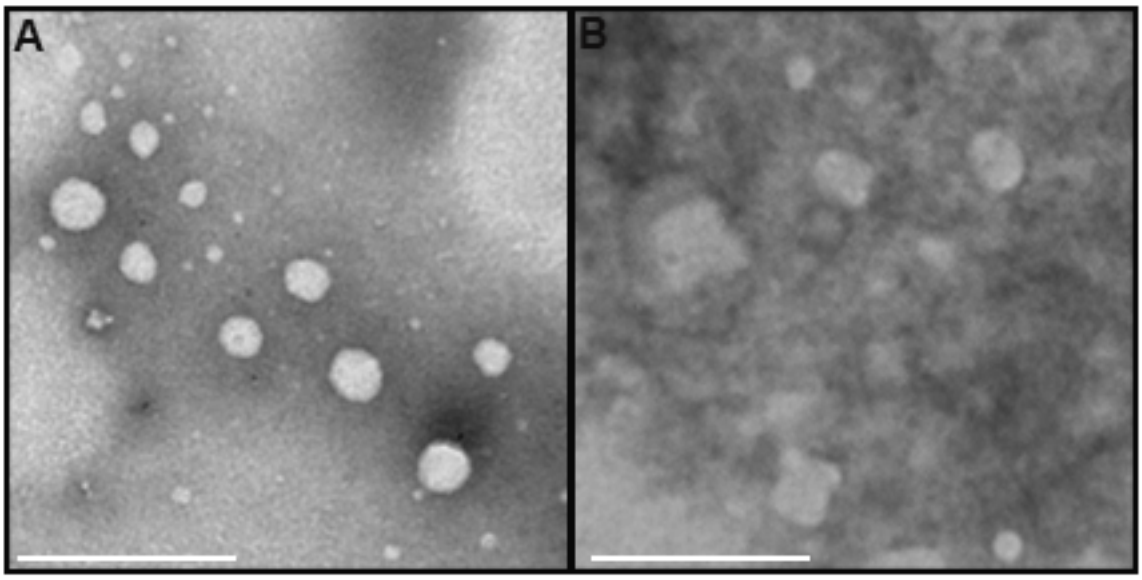

Figure B.6: Upon treatments, Sf9 cells were washed and stained with 7-AAD dye and analyzed using flow cytometry. First, cells were selected based on size by plotting SSC vs FSC, then selection of singlet cells by applying FSC-height vs FSC-area and lastly, viable cells were quantified using 7-AAD (negative).

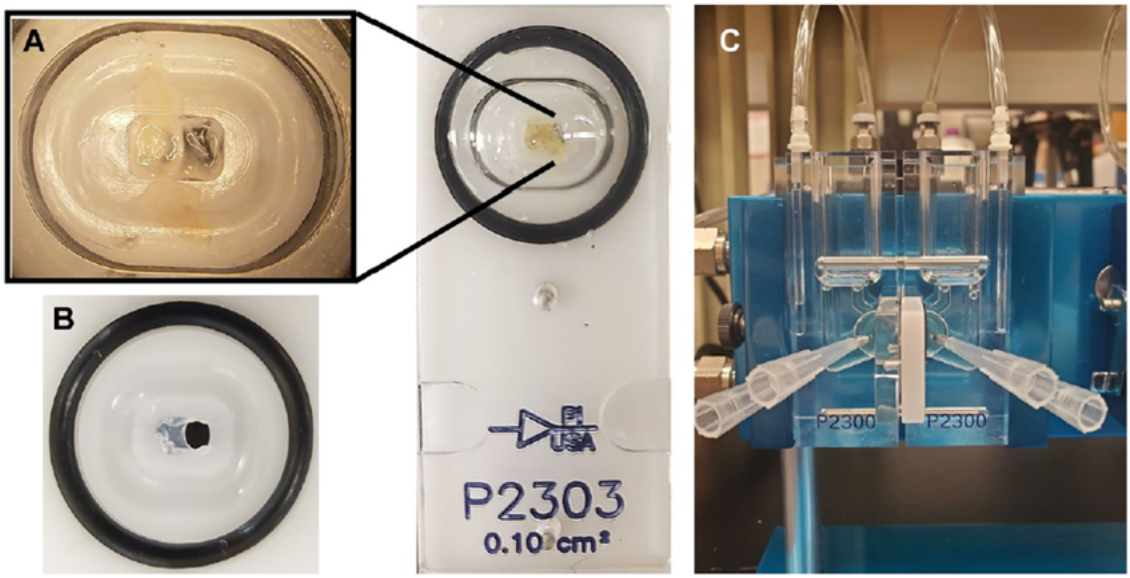

Figure B.7: Ussing chamber set-up. (A) Tissues were mounted on modified 0.1cm^2 slide. (B) Sliders were modified by coating approximately half of the area with a clear enamel. (C) Full final set-up of Ussing chamber.

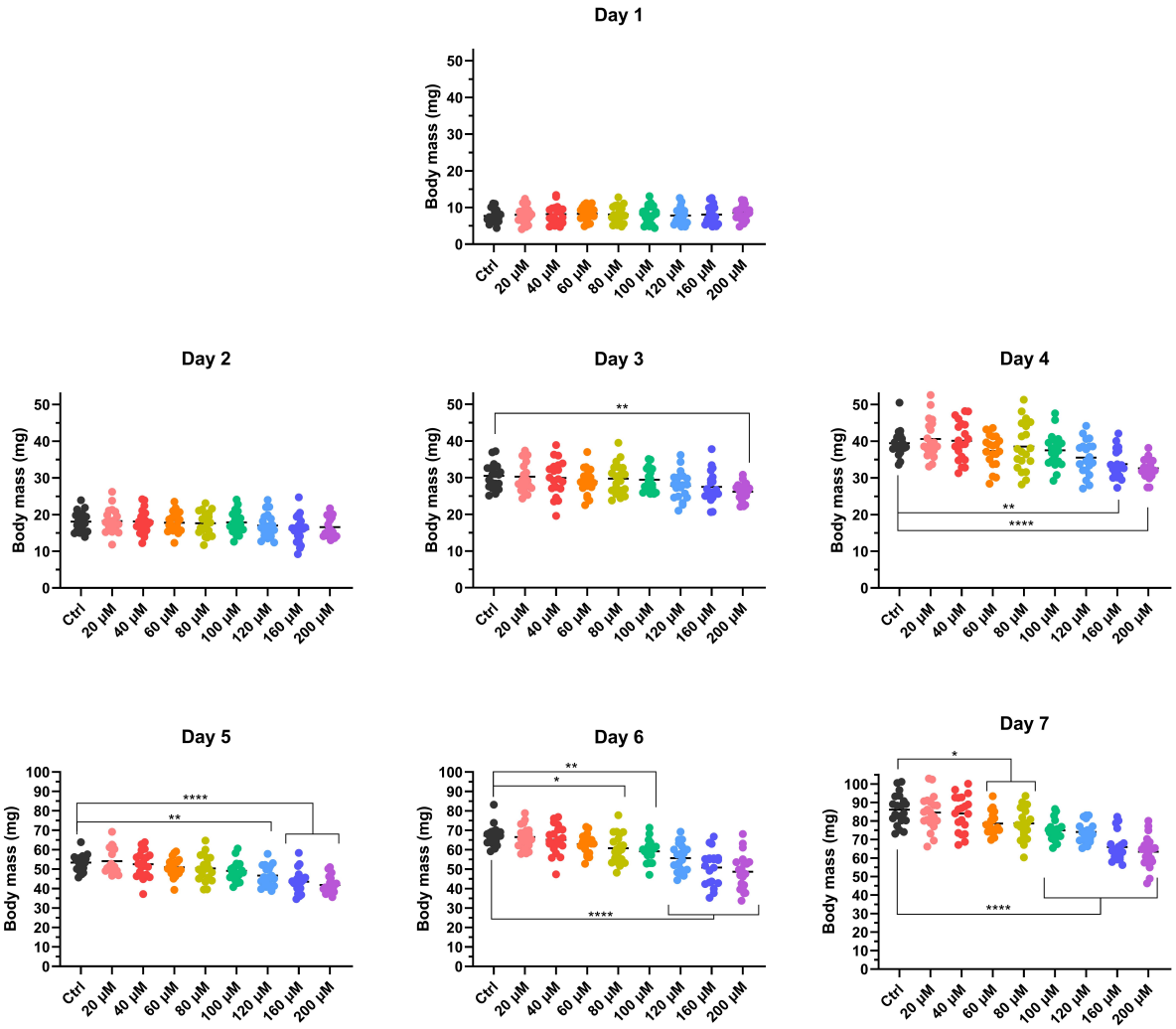

Figure B.8: Daily changes in larval weight resulting from BAPCs consumption. Day 1 represents larval body mass before the first feed, and each subsequent day is 24 h following the previous feed. BAPCs (0, 20, 40, 60, 80, 100, 120, 160, or 200 μM) were added to 50-100 mg of gelled wheat/soy protein diet. Third instar *S. frugiperda* larvae (n = 20) were fed fresh diet with BAPCs and weighed each day for 6 days. Ctrl = diet supplemented with deionized H_2O. Statistical significance: (*) $p < 0.033$; (**) $p < 0.002$; (***) $p < 0.0002$; (****) $p < 0.0001$; (ns) $p > 0.12$ versus control group or as indicated in the bars (ANOVA, Dunnett posttest).

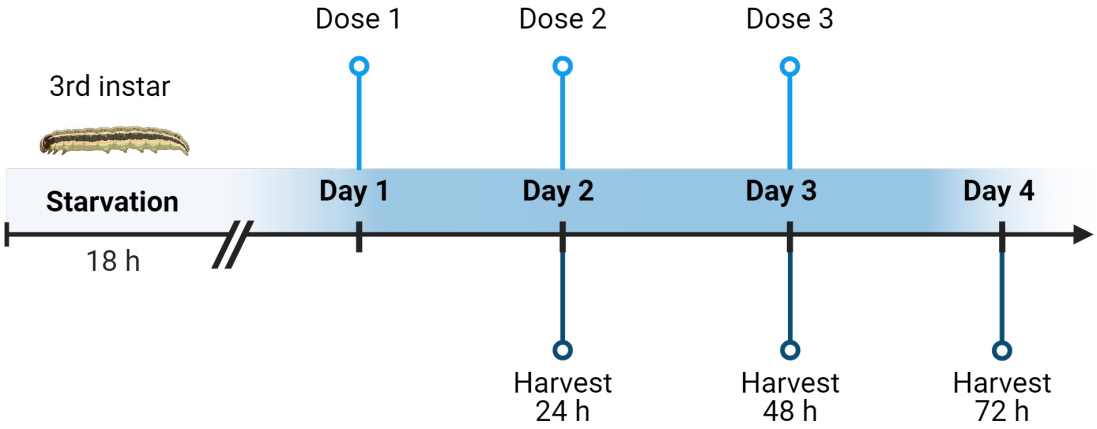

Figure B.9: Schematic showing experimental timeline of feedings and larval harvesting for RT-qPCR analysis of *S. frugiperda* larvae. Food was withheld overnight ($\sim$ 18 h) prior to the first treatment. Each day for three days, larvae were supplied with fresh food containing control (water) or treatment (BAPCS, V_B-dsRNA, or BAPC-V_B complexes), and 24 h after each feeding, larvae were sacrificed for total RNA extraction.

Primers	**Sequence (5'-3')**
dsRNA synthesis	
dsV-ATPase A-F1	taatacgactcactatagggAAAGCTTGCAGTCGGTCACCAGGGCT
dsV-ATPase A-R1	ACGGGCTCCCGAGTGAGCGG
dsV-ATPase A-F2	AAGACTGTCGTCTCACAGCGCT
dsV-ATPase A-R2	taatacgactcactatagggATAATCGCCCGGAGGGTTGTAC
dsV-ATPase B-F1	taatacgactcactatagggAACCGTTGCAGGTGCGCAGC
dsV-ATPase B-R1	CTCACGGGGCGGGTACCCTC
dsV-ATPase B-F2	AACTCACCGAACCAGTGCTCAG
dsV-ATPase B-R2	taatacgactcactatagggCAGCGACTTAATGCCCAAGTGTC
dsSV-ATPase D-F1	taatacgactcactatagggACTGGCGAATCGGTGCCCGC
dsV-ATPase D-R1	CTTGTTAGGCGCGTTCGCGCC
dsV-ATPase D-F2	GGTGCAGACTGCCGTGCTGCTAC
dsV-ATPase D-R2	taatacgactcactatagggCACGCGGGTGCACAGTGCCGC
RT-qPCR analysis	
SfV-ATPase A-F	AGTCACCATCAGAGCAATGACCG
SfV-ATPase A-R	CACGTGTTCAACCCTGAGCTCACG
SfV-ATPase B-F	ATCGCTTGAGGGAAGGTTGTCAAGC
SfV-ATPase B-R	GGTGCTACACACTCAAGATCTTTC
SfV-ATPase D-F	CACGCACACATGTCGACTACTTTC
SfV-ATPase D-R	ACCACGAGCTGCTGAAGGTTGAAC
β-Actin-F	TCTCTCAGCACCTTGAGAGGTTG
β-Actin-R	GTGATCTCCTCTGACTTCGTGGT

Table B.2: Primer sequences for dsRNA synthesis and RT-qPCR analysis. Primers for SfV-ATPase A and SfV-ATPase B reproduced from Reference [2]

Target	**Sequence 5'-3'**	Size (bp)
SfV-ATPase A	AAGACTGTCGTCTCACAGGCTCTGTCCAAG TACTCCAACTCTGACGTCATCATCTACGTC GGATGCGGTGAACGTGGTAACGAGATGTCT GAGGTACTGCGTGACTTCCCCGAGCTGACG GTGGAGATCGAGGGCATGACCGAGTCCATC ATGAAGCGTACCGCGCTCGTCGCCAACACC TCCAACATGCCTGTAGCCGCCCGAGAGGCT TCCATCTACACCGGTATCACCCTCTCCGAG TACTTCCGTGACATGGGTTACAACGTGTCC ATGATGGCTGACTCCACCTCTCGTTGGGCC GAGGCTCTTCGTGAGATCTCAGGTCGTCTG GCTGAGATGCCTGCCGACTCCGGTTACCCC GCCTACCTGGGAGCCCGT	387
SfV-ATPase B	AACTCCATCGCTCGTGGTCAGAAGATCCCC ATCTTCTCCGCTGCTGGTCTGCCCCACAAC GAAATTGCCGCCCAGATCGTAGACAGGCCG GTCTTGTCAAGATCCCCGGCAAATCAGTGT TGGATGACCACGAGGACAACTTCGCCATCG TGTTCGCCGCTATGGGTGTGAACATGGAAA CCGCCCGGTTCTTCAAACAGGACTTCGAAG AGAACGGTTCCATGGAGAACGTGTGCCTGT TCTTGAACTTGGCCAACGACCCTACCATTG AGAGAATTATCACACCCCGTCTGGCTCTTA CTGCCGCCGAGTTCTTGGCCTACCAGTGCG AGAAACACGTGTTGGTCATCTTGACTGACA TGTCCTCATACGCCGAGGCTCTGCGTGAG GTATCCGCCGCCCGTGAG	408
SfV-ATPase D	GGTCGAGTTGGCTTCGCTGCAGACTTCTTT CGTGACCCTCGATGAGGTCATCAAGATCAC CAACAGACGTGTCAATGCTATTGAGCATGT AATCATTCCCCGACTGGAGCGTACCCTCGC TTACATCATCTCCGAGCTGGATGAGTTGGA ACGTGAGGAGTTCTACCGGCTGAAGAAGAT CCAGGACAAGAAGAAGCAAGAAGAAGATCA TCAAGGAGAAGGCGG	204

Table B.3: dsRNA sequences targeting V-ATPase subunits in *S. frugiperda*. Sequences for SfV-ATPase A and SfV-ATPase B reproduced from Reference [2]

Bibliography

[1] Benedict, K, Whitham, H. K, & Jackson, B. R. (2022) Economic Burden of Fungal Diseases in the United States. *Open Forum Infectious Diseases* **9**, ofac097.

[2] Bai, S, Jin, D, Jiang, Y, Chen, F, Cheng, W, & Qi, Z. (2023) Development of a recombinant baculovirus with dual effects to mediate V-ATPase interference by RNA in the fall armyworm Spodoptera frugiperda. *Journal of Pest Science* **96**, 1667–1681.

[3] Bradshaw, C. J, Leroy, B, Bellard, C, Roiz, D, Albert, C, Fournier, A, Barbet-Massin, M, Salles, J. M, Simard, F, & Courchamp, F. (2016) Massive yet grossly underestimated global costs of invasive insects. *Nature Communications 2016 7:1* **7**, 1–8.

[4] Amendola, V, Pilot, R, Frasconi, M, Maragò, O. M, & Iatì, M. A. (2017) Surface plasmon resonance in gold nanoparticles: A review. *Journal of Physics Condensed Matter* **29**, 203002.

[5] Arich, S, Assaid, N, Weill, M, Tmimi, F. Z, Taki, H, Sarih, M, & Labbé, P. (2024) Human activities and densities shape insecticide resistance distribution and dynamics in the virus-vector Culex pipiens mosquitoes from Morocco. *Parasites and Vectors* **17**, 1–12.

[6] Chen, H. L, Hasnain, A, Cheng, Q. H, Xia, L. J, Cai, Y. H, Hu, R, Gong, C. W, Liu, X. M, Pu, J, Zhang, L, & Wang, X. G. (2023) Resistance monitoring and mechanism in the fall armyworm Spodoptera frugiperda (Lepidoptera: Noctuidae) for chlorantraniliprole from Sichuan Province, China. *Frontiers in Physiology* **14**, 1180655.

[7] Ahmady, L, Gothwal, M, Mukkoli, M. M, & Bari, V. K. (2024) Antifungal drug resistance in Candida: a special emphasis on amphotericin B. *APMIS* **132**, 291–316.

[8] Bongomin, F, Gago, S, Oladele, R. O, & Denning, D. W. (2017) Global and Multi-National Prevalence of Fungal Diseases—Estimate Precision. *Journal of Fungi* **3**, 57.

[9] Roemer, T & Krysan, D. J. (2014) Antifungal drug development: challenges, unmet clinical needs, and new approaches.

[10] Hoenigl, M, Sprute, R, Egger, M, Arastehfar, A, Cornely, O. A, Krause, R, Lass-Flörl, C, Prattes, J, Spec, A, Thompson, G. R, Wiederhold, N, & Jenks, J. D. (2021) The Antifungal Pipeline: Fosmanogepix, Ibrexafungerp, Olorofim, Opelconazole, and Rezafungin. *Drugs 2021 81:15* **81**, 1703–1729.

[11] World Health Organization. (2022) WHO fungal priority pathogens list to guide research, development and public health action., (World Health Organization, Geneva), Technical report.

[12] Costa-de oliveira, S & Rodrigues, A. G. (2020) Candida albicans antifungal resistance and tolerance in bloodstream infections: The triad yeast-host-antifungal.

[13] Forsberg, K, Woodworth, K, Walters, M, Berkow, E. L, Jackson, B, Chiller, T, & Vallabhaneni, S. (2019) Candida auris: The recent emergence of a multidrug-resistant fungal pathogen. *Medical Mycology* **57**, 1–12.

[14] Pappas, P. G, Lionakis, M. S, Arendrup, M. C, Ostrosky-Zeichner, L, & Kullberg, B. J. (2018) Invasive candidiasis. *Nature Reviews Disease Primers* **4**, 1–20.

[15] Siddiqui, J. A, Fan, R, Naz, H, Bamisile, B. S, Hafeez, M, Ghani, M. I, Wei, Y, Xu, Y, & Chen, X. (2023) Insights into insecticide-resistance mechanisms in invasive species: Challenges and control strategies. *Frontiers in Physiology* **13**, 1112278.

[16] Boaventura, D, Martin, M, Pozzebon, A, Mota-Sanchez, D, & Nauen, R. (2020) Monitoring of Target-Site Mutations Conferring Insecticide Resistance in Spodoptera frugiperda. *Insects 2020, Vol. 11, Page 545* **11**, 545.

[17] De Groote, H, Kimenju, S. C, Munyua, B, Palmas, S, Kassie, M, & Bruce, A. (2020) Spread and impact of fall armyworm (Spodoptera frugiperda J.E. Smith) in maize production areas of Kenya. *Agriculture, Ecosystems & Environment* **292**, 106804.

[18] Matova, P. M, Kamutando, C. N, Magorokosho, C, Kutywayo, D, Gutsa, F, & Labuschagne, M. (2020) Fall-armyworm invasion, control practices and resistance breeding in Sub-Saharan Africa. *Crop Science* **60**, 2951.

[19] Bai-Zhong, Z, Xu, S, Cong-Ai, Z, Liu-Yang, L, Ya-She, L, Xing, G, Dong-Mei, C, Zhang, P, Ming-Wang, S, & Xi-Ling, C. (2020) Silencing of Cytochrome P450 in Spodoptera frugiperda (Lepidoptera: Noctuidae) by RNA Interference Enhances Susceptibility to Chlorantraniliprole. *Journal of Insect Science* **20**.

[20] Janbon, G, Quintin, J, Lanternier, F, & d'Enfert, C. (2019) Studying fungal pathogens of humans and fungal infections: fungal diversity and diversity of approaches.

[21] Chareonviriyaphap, T, Bangs, M. J, Suwonkerd, W, Kongmee, M, Corbel, V, & Ngoen-Klan, R. (2013) Review of insecticide resistance and behavioral avoidance of vectors of human diseases in Thailand. *Parasites and Vectors* **6**, 1–28.

[22] Bumcrot, D, Manoharan, M, Koteliansky, V, & Sah, D. W. (2006) RNAi therapeutics: A potential new class of pharmaceutical drugs.

[23] Zhu, K. Y & Palli, S. R. (2020) Mechanisms, applications, and challenges of insect RNA interference.

[24] Kunte, N, McGraw, E, Bell, S, Held, D, & Avila, L.-A. L. A. (2020) Prospects, challenges and current status of RNAi through insect feeding. *Pest Management Science* **76**, 26–41.

[25] McGraw, E, Dissanayaka, R. R, Vaughan, J. J, Kunte, N, Mills, G, Laurent, G. G. G, & Avila, L. A. (2020) Laser-Assisted Delivery of Molecules in Fungal Cells. *ACS Applied Bio Materials* **3**, 6167 – 6176.

[26] Latgé, J. P. (2007) The cell wall: A carbohydrate armour for the fungal cell.

[27] Santos, G. C. O, Vasconcelos, C. C, Lopes, A. J, Cartágenes, M. d. S. S, Filho, A. K, do Nascimento, F. R, Ramos, R. M, Pires, E. R, de Andrade, M. S, Rocha, F. M, & Monteiro, C. d. A. (2018) Candida Infections and Therapeutic Strategies: Mechanisms of Action for Traditional and Alternative Agents. *Frontiers in Microbiology* **9**, 1351.

[28] Revie, N. M, Iyer, K. R, Robbins, N, & Cowen, L. E. (2018) Antifungal Drug Resistance: Evolution, Mechanisms and Impact. *Current opinion in microbiology* **45**, 70.

[29] Segal, B. H, Almyroudis, N. G, Battiwalla, M, Herbrecht, R, Perfect, J. R, Walsh, T. J, & Wingard, J. R. (2007) Prevention and early treatment of invasive fungal infection in patients with cancer and neutropenia and in stem cell transplant recipients in the era of newer broad-spectrum antifungal agents and diagnostic adjuncts. *Clinical Infectious Diseases* **44**, 402–409.

[30] Hope, W. W, Tabernero, L, Denning, D. W, & Anderson, M. J. (2004) Molecular mechanisms of primary resistance to flucytosine in Candida albicans. *Antimicrobial Agents and Chemotherapy* **48**, 4377–4386.

[31] Lakhani, P, Patil, A, & Majumdar, S. (2019) Challenges in the Polyene- and Azole-Based Pharmacotherapy of Ocular Fungal Infections. *Journal of Ocular Pharmacology and Therapeutics* **35**, 6.

[32] Szymański, M, Chmielewska, S, Czyżewska, U, Malinowska, M, & Tylicki, A. (2022) Echinocandins – structure, mechanism of action and use in antifungal therapy. *Journal of Enzyme Inhibition and Medicinal Chemistry* **37**, 876–894.

[33] Vanreppelen, G, Wuyts, J, Van Dijck, P, & Vandecruys, P. (2023) Sources of Antifungal Drugs. *Journal of Fungi 2023, Vol. 9, Page 171* **9**, 171.

[34] Delma, F. Z, Al-Hatmi, A. M, Brüggemann, R. J, Melchers, W. J, de Hoog, S, Verweij, P. E, & Buil, J. B. (2021) Molecular Mechanisms of 5-Fluorocytosine Resistance in Yeasts and Filamentous Fungi. *Journal of Fungi* **7**.

[35] Dong, K, Sun, L, Liu, J. T, Gu, S. H, Zhou, J. J, Yang, R. N, Dhiloo, K. H, Gao, X. W, Guo, Y. Y, & Zhang, Y. J. (2017) RNAi-Induced Electrophysiological and Behavioral Changes Reveal two Pheromone Binding Proteins of Helicoverpa armigera Involved in the Perception of the Main Sex Pheromone Component Z11–16:Ald. *Journal of Chemical Ecology* **43**, 207–214.

[36] Wood, O. R, Hanrahan, S, Coetzee, M, Koekemoer, L. L, & Brooke, B. D. (2010) Cuticle thickening associated with pyrethroid resistance in the major malaria vector Anopheles funestus. *Parasites and Vectors* **3**, 1–7.

[37] Li, W, Yang, W, Shi, Y, Yang, X, Liu, S, Liao, X, & Shi, L. (2024) Comprehensive analysis of the overexpressed cytochrome P450-based insecticide resistance mechanism in Spodoptera litura. *Journal of Hazardous Materials* **461**, 132605.

[38] Valmorbida, I, Hohenstein, J. D, Coates, B. S, Bevilaqua, J. G, Menger, J, Hodgson, E. W, Koch, R. L, & O'Neal, M. E. (2022) Association of voltage-gated sodium channel mutations with field-evolved pyrethroid resistant phenotypes in soybean aphid and genetic markers for their detection. *Scientific Reports 2022 12:1* **12**, 1–14.

[39] Ansari, M. S, Moraiet, M. A, & Ahmad, S. (2014) Insecticides: Impact on the Environment and Human Health. *Environmental Deterioration and Human Health: Natural and Anthropogenic Determinants* **9789400778900**, 99–123.

[40] Huang, B & Zhang, R. (2014) Regulatory non-coding RNAs: Revolutionizing the RNA world. *Molecular Biology Reports* **41**, 3915–3923.

[41] Gourse, R. L, Takebe, Y, Sharrock, R. A, & Nomura, M. (1985) Feedback regulation of rRNA and tRNA synthesis and accumulation of free ribosomes after conditional expression of rRNA genes. *Proceedings of the National Academy of Sciences of the United States of America* **82**, 1069.

[42] Dang, Y, Yang, Q, Xue, Z, & Liu, Y. (2011) RNA interference in fungi: Pathways, functions, and applications.

[43] Kang, H, Ga, Y. J, Kim, S. H, Cho, Y. H, Kim, J. W, Kim, C, & Yeh, J. Y. (2023) Small interfering RNA (siRNA)-based therapeutic applications against viruses: principles, potential, and challenges. *Journal of Biomedical Science 2023 30:1* **30**, 1–18.

[44] Cubillos-Ruiz, J. R, Engle, X, Scarlett, U. K, Martinez, D, Barber, A, Elgueta, R, Wang, L, Nesbeth, Y, Durant, Y, Gewirtz, A. T, Sentman, C. L, Kedl, R, & Conejo-Garcia, J. R. (2009) Polyethylenimine-based siRNA nanocomplexes reprogram tumor-associated dendritic cells via TLR5 to elicit therapeutic antitumor immunity. *The Journal of Clinical Investigation* **119**, 2231–2244.

[45] Davis, M. E, Zuckerman, J. E, Choi, C. H. J, Seligson, D, Tolcher, A, Alabi, C. A, Yen, Y, Heidel, J. D, & Ribas, A. (2010) Evidence of RNAi in humans from systemically administered siRNA via targeted nanoparticles. *Nature 2010 464:7291* **464**, 1067–1070.

[46] Griesenbach, U, Kitson, C, Garcia, S. E, Farley, R, Singh, C, Somerton, L, Painter, H, Smith, R. L, Gill, D. R, Hyde, S. C, Chow, Y. H, Hu, J, Gray, M, Edbrooke, M, Ogilvie, V, MacGregor, G, Scheule, R. K, Cheng, S. H, Caplen, N. J, & Alton, E. W. (2006) Inefficient cationic lipid-mediated siRNA and antisense oligonucleotide transfer to airway epithelial cells in vivo. *Respiratory Research* **7**, 1–15.

[47] Andika, I. B, Kondo, H, & Suzuki, N. (2019) Dicer functions transcriptionally and posttranscriptionally in a multilayer antiviral defense. *Proceedings of the National Academy of Sciences of the United States of America* **116**, 2274–2281.

[48] Iwasaki, Y. W, Siomi, M. C, & Siomi, H. (2015) PIWI-Interacting RNA: Its Biogenesis and Functions. *Annual review of biochemistry* **84**, 405–433.

[49] Lam, J. K, Chow, M. Y, Zhang, Y, & Leung, S. W. (2015) siRNA Versus miRNA as Therapeutics for Gene Silencing. *Molecular Therapy. Nucleic Acids* **4**, e252.

[50] Jinek, M & Doudna, J. A. (2008) A three-dimensional view of the molecular machinery of RNA interference. *Nature 2009 457:7228* **457**, 405–412.

[51] Iwasaki, S, Kobayashi, M, Yoda, M, Sakaguchi, Y, Katsuma, S, Suzuki, T, & Tomari, Y. (2010) Hsc70/Hsp90 chaperone machinery mediates ATP-dependent RISC loading of small RNA duplexes. *Molecular Cell* **39**, 292–299.

[52] Betancur, J. G & Tomari, Y. (2012) Dicer is dispensable for asymmetric RISC loading in mammals. *RNA* **18**, 24.

[53] Noland, C. L & Doudna, J. A. (2013) Multiple sensors ensure guide strand selection in human RNAi pathways. *RNA* **19**, 639–648.

[54] Kwak, P. B & Tomari, Y. (2012) The N domain of Argonaute drives duplex unwinding during RISC assembly. *Nature Structural & Molecular Biology 2012 19:2* **19**, 145–151.

[55] Orban, T. I & Izaurralde, E. (2005) Decay of mRNAs targeted by RISC requires XRN1, the Ski complex, and the exosome. *RNA* **11**, 459.

[56] Yoon, J. S, Gurusamy, D, & Palli, S. R. (2017) Accumulation of dsRNA in endosomes contributes to inefficient RNA interference in the fall armyworm, Spodoptera frugiperda. *Insect Biochemistry and Molecular Biology* **90**, 53–60.

[57] Mishra, S, Dee, J, Moar, W, Dufner-Beattie, J, Baum, J, Dias, N. P, Alyokhin, A, Buzza, A, Rondon, S. I, Clough, M, Menasha, S, Groves, R, Clements, J, Ostlie, K, Felton, G, Waters, T, Snyder, W. E, & Jurat-Fuentes, J. L. (2021) Selection for high levels of resistance to double-stranded RNA (dsRNA) in Colorado potato beetle (Leptinotarsa decemlineata Say) using non-transgenic foliar delivery. *Scientific Reports* **11**, 1–12.

[58] Nakayashiki, H, Kadotani, N, & Mayama, S. (2006) Evolution and diversification of RNA silencing proteins in fungi. *Journal of Molecular Evolution* **63**, 127–135.

[59] Avila, L. A, Chandrasekar, R, Wilkinson, K. E, Balthazor, J, Heerman, M, Bechard, J, Brown, S, Park, Y, Dhar, S, Reeck, G. R, & Tomich, J. M. (2018) Delivery of lethal dsRNAs in insect diets by branched amphiphilic peptide capsules. *Journal of Controlled Release* **273**, 139–146.

[60] Nayerossadat, N, Ali, P, & Maedeh, T. (2012) Viral and nonviral delivery systems for gene delivery. *Advanced Biomedical Research* **1**, 27.

[61] De Haan, P, Van Diemen, F. R, & Toscano, M. G. (2020) Viral gene delivery vectors: the next generation medicines for immune-related diseases. *Human Vaccines & Immunotherapeutics* **17**, 14.

[62] Taghdiri, M & Mussolino, C. (2024) Viral and Non-Viral Systems to Deliver Gene Therapeutics to Clinical Targets. *International Journal of Molecular Sciences* **25**, 7333.

[63] Malyska, A, Bolla, R, & Twardowski, T. (2016) The Role of Public Opinion in Shaping Trajectories of Agricultural Biotechnology. *Trends in Biotechnology* **34**, 530–534.

[64] Kwon, M & Firestein, B. L. (2013) DNA Transfection: Calcium Phosphate Method. *Methods in Molecular Biology* **1018**, 107–110.

[65] Van Hoof, D, Rodenburg, K. W, & Van Der Horst, D. J. (2005) Receptor-mediated endocytosis and intracellular trafficking of lipoproteins and transferrin in insect cells. *Insect Biochemistry and Molecular Biology* **35**, 117–128.

[66] Saadat, M, Zahednezhad, F, Zakeri-Milani, P, Heidari, H. R, Shahbazi-Mojarrad, J, & Valizadeh, H. (2019) Drug Targeting Strategies Based on Charge Dependent Uptake of Nanoparticles into Cancer Cells. *Journal of Pharmacy & Pharmaceutical Sciences* **22**, 191–220.

[67] Patel, S, Kim, J, Herrera, M, Mukherjee, A, Kabanov, A. V, & Sahay, G. (2019) Brief update on endocytosis of nanomedicines.

[68] Jin, L, Zeng, X, Liu, M, Deng, Y, & He, N. (2014) Current Progress in Gene Delivery Technology Based on Chemical Methods and Nano-carriers. *Theranostics* **4**, 240.

[69] Kim, T. K & Eberwine, J. H. (2010) Mammalian cell transfection: The present and the future. *Analytical and Bioanalytical Chemistry* **397**, 3173–3178.

[70] Chicaybam, L, Barcelos, C, Peixoto, B, Carneiro, M, Limia, C. G, Redondo, P, Lira, C, Paraguassú-Braga, F, Vasconcelos, Z. F. M. D, Barros, L, & Bonamino, M. H. (2017) An Efficient Electroporation Protocol for the Genetic Modification of Mammalian Cells. *Frontiers in Bioengineering and Biotechnology* **4**, 229100.

[71] Batista Napotnik, T, Polajžer, T, & Miklavčič, D. (2021) Cell death due to electroporation – A review.

[72] Mitchell, C. A, Kalies, S, Cizmár, T, Heisterkamp, A, Torrance, L, Roberts, A. G, Gunn-Moore, F. J, & Dholakia, K. (2013) Femtosecond optoinjection of intact tobacco BY-2 cells using a reconfigurable photoporation platform. *PLoS ONE* **8**, e79235.

[73] Date, A. A, Hanes, J, & Ensign, L. M. (2016) Nanoparticles for oral delivery: Design, evaluation and state-of-the-art. *Journal of Controlled Release* **240**, 504–526.

[74] Gumustas, M, Sengel-Turk, C. T, Gumustas, A, Ozkan, S. A, & Uslu, B. (2017) in *Multifunctional Systems for Combined Delivery, Biosensing and Diagnostics*, ed. Grumezescu, A. M. (Elsevier), pp. 67–108.

[75] Verma, A & Stellacci, F. (2010) Effect of surface properties on nanoparticle-cell interactions. *Small* **6**, 12–21.

[76] Mendes, B. B, Conniot, J, Avital, A, Yao, D, Jiang, X, Zhou, X, Sharf-Pauker, N, Xiao, Y, Adir, O, Liang, H, Shi, J, Schroeder, A, & Conde, J. (2022) Nanodelivery of nucleic acids. *Nature Reviews Methods Primers 2022 2:1* **2**, 1–21.

[77] Faustino, C & Pinheiro, L. (2020) Lipid systems for the delivery of amphotericin B in antifungal therapy.

[78] Hunter, A. C & Moghimi, S. M. (2010) Cationic carriers of genetic material and cell death: A mitochondrial tale.

[79] Sukthankar, P, Avila, L. A, Whitaker, S. K, Iwamoto, T, Morgenstern, A, Apostolidis, C, Liu, K, Hanzlik, R. P, Dadachova, E, & Tomich, J. M. (2014) Branched amphiphilic peptide capsules: Cellular uptake and retention of encapsulated solutes. *Biochimica et Biophysica Acta - Biomembranes* **1838**, 2296–2305.

[80] Su, Y, Doherty, T, Waring, A. J, Ruchala, P, & Hong, M. (2009) Roles of arginine and lysine residues in the translocation of a cell-penetrating peptide from13C, 31P, and19F Solid-State NMR. *Biochemistry* **48**, 4587–4595.

[81] Luther, D. C, Huang, R, Jeon, T, Zhang, X, Lee, Y. W, Nagaraj, H, & Rotello, V. M. (2020) Delivery of Drugs, Proteins, and Nucleic Acids using Inorganic Nanoparticles. *Advanced drug delivery reviews* **156**, 188.

[82] Mohan, L, Kar, S, Ren Hattori, Ishii-Teshima, M, Bera, P, Roy, S, Santra, T. S, Shibata, T, & Nagai, M. (2021) Can titanium oxide nanotubes facilitate intracellular delivery by laser-assisted photoporation? *Applied Surface Science* **543**, 148815.

[83] Huang, X & El-Sayed, M. A. (2010) Gold nanoparticles: Optical properties and implementations in cancer diagnosis and photothermal therapy.

[84] Boulais, E, Lachaine, R, & Meunier, M. (2013) Plasma-mediated nanocavitation and photothermal effects in ultrafast laser irradiation of gold nanorods in water. *Journal of Physical Chemistry C* **117**, 9386–9396.

[85] Georganopoulou, D. G, Chang, L, Nam, J. M, Thaxton, C. S, Mufson, E. J, Klein, W. L, & Mirkin, C. A. (2005) Nanoparticle-based detection in cerebral spinal fluid of a soluble pathogenic biomarker for Alzheimer's disease. *Proceedings of the National Academy of Sciences of the United States of America* **102**, 2273.

[86] Patlolla, A. K, Kumari, S. A, & Tchounwou, P. B. (2019) A comparison of poly-ethylene-glycol-coated and uncoated gold nanoparticle-mediated hepatotoxicity and oxidative stress in sprague dawley rats. *International Journal of Nanomedicine* **14**, 639–647.

[87] Avila, L. A, Aps, L. R, Ploscariu, N, Sukthankar, P, Guo, R, Wilkinson, K. E, Games, P, Szoszkiewicz, R, Alves, R. P, Diniz, M. O, Fang, Y, Ferreira, L. C, & Tomich, J. M. (2016) Gene delivery and immunomodulatory effects of plasmid DNA associated with Branched Amphiphilic Peptide Capsules. *Journal of Controlled Release* **241**, 15–24.

[88] Xiong, R, Samal, S. K, Demeester, J, Skirtach, A. G, De Smedt, S. C, & Braeckmans, K. (2016) Laser-assisted photoporation: fundamentals, technological advances and applications.

[89] Ameen, M. (2010) Epidemiology of superficial fungal infections.

[90] Li, D, Tang, Y, Lin, J, & Cai, W. (2017) Methods for genetic transformation of filamentous fungi.

[91] Kawai, S, Hashimoto, W, & Murata, K. (2010) Transformation of Saccharomyces cerevisiae and other fungi: methods and possible underlying mechanism.

[92] Lee, W. G, Demirci, U, & Khademhosseini, A. (2009) Microscale electroporation: Challenges and perspectives for clinical applications. *Integrative Biology* **1**, 242–251.

[93] Stewart, M. P, Langer, R, & Jensen, K. F. (2018) Intracellular delivery by membrane disruption: Mechanisms, strategies, and concepts.

[94] Shi, J, Ma, Y, Zhu, J, Chen, Y, Sun, Y, Yao, Y, Yang, Z, & Xie, J. (2018) A review on electroporation-based intracellular delivery.

[95] Van Hoecke, L, Raes, L, Stremersch, S, Brans, T, Fraire, J. C, Roelandt, R, Declercq, W, Vandenabeele, P, Raemdonck, K, Braeckmans, K, & Saelens, X. (2019) Delivery of mixed-lineage kinase domain-like protein by vapor nanobubble photoporation induces necroptotic-like cell death in tumor cells. *International Journal of Molecular Sciences* **20**.

[96] Chakravarty, P, Qian, W, El-Sayed, M. A, & Prausnitz, M. R. (2010) Delivery of molecules into cells using carbon nanoparticles activated by femtosecond laser pulses. *Nature Nanotechnology* **5**, 607–611.

[97] Antkowiak, M, Torres-Mapa, M. L, Gunn-Moore, F, & Dholakia, K. (2010) Application of dynamic diffractive optics for enhanced femtosecond laser based cell transfection. *Journal of Biophotonics* **3**, 696–705.

[98] Slivac, I, Guay, D, Mangion, M, Champeil, J, & Gaillet, B. (2017) Non-viral nucleic acid delivery methods.

[99] Becker, D. M & Lundblad, V. (2001) in *Current Protocols in Molecular Biology*. (John Wiley & Sons, Inc., Hoboken, NJ, USA).

[100] Aigrain, L, Sustarsic, M, Crawford, R, Plochowietz, A, & Kapanidis, A. N. (2015) Internalization and observation of fluorescent biomolecules in living microorganisms via electroporation. *Journal of Visualized Experiments* p. 52208.

[101] Feyder, S, De Craene, J. O, Bär, S, Bertazzi, D. L, & Friant, S. (2015) Membrane trafficking in the yeast Saccharomyces cerevisiae model.

[102] Longenberger, L & Mills, G. (1995) Formation of metal particles in aqueous solutions by reactions of metal complexes with polymers. *Journal of Physical Chemistry* **99**, 475–478.

[103] World Health Organization. (2019) World Health Organization Model List of Essential Medicines, (World Health Organization, Geneva), Technical report.

[104] Grewal, D. S, Schultz, T, Basti, S, & Dick, H. B. (2016) Femtosecond laser-assisted cataract surgery-current status and future directions. *Survey of Ophthalmology* **61**, 103–131.

[105] Meader, V. K, John, M. G, Rodrigues, C. J, & Tibbetts, K. M. (2017) Roles of Free Electrons and H2O2 in the Optical Breakdown-Induced Photochemical Reduction of Aqueous [AuCl4]-. *Journal of Physical Chemistry A* **121**, 6742–6754.

[106] Belmouaddine, H, Shi, M, Karsenti, P. L, Meesat, R, Sanche, L, & Houde, D. (2017) Dense ionization and subsequent non-homogeneous radical-mediated chemistry of femtosecond laser-induced low density plasma in aqueous solutions: Synthesis of colloidal gold. *Physical Chemistry Chemical Physics* **19**, 7897–7909.

[107] Linz, N, Freidank, S, Liang, X. X, & Vogel, A. (2016) Wavelength dependence of femtosecond laser-induced breakdown in water and implications for laser surgery. *Physical Review B* **94**, 024113.

[108] Brown, D. H & Smith, W. E. (1980) The chemistry of the gold drugs used in the treatment of rheumatoid arthritis.

[109] Finch, C. A. (1992) *Poly(ethylene glycol) chemistry: Biotechnical and Biomedical Applications* ed. Harris, J. M. (Plenum Press, New York), pp. 1–14.

[110] Kreibig, U & Vollmer, M. (1996) *Optical Properties of Metal Clusters*. No. Part_2, pp. 278–279.

[111] Bucharskaya, A, Maslyakova, G, Terentyuk, G, Yakunin, A, Avetisyan, Y, Bibikova, O, Tuchina, E, Khlebtsov, B, Khlebtsov, N, & Tuchin, V. (2016) Towards effective photothermal/photodynamic treatment using plasmonic gold nanoparticles.

[112] Bhattacharjee, S. (2016) DLS and zeta potential - What they are and what they are not?

[113] Herzenberg, L. A, Tung, J, Moore, W. A, Herzenberg, L. A, & Parks, D. R. (2006) Interpreting flow cytometry data: A guide for the perplexed.

[114] Riccardi, C & Nicoletti, I. (2006) Analysis of apoptosis by propidium iodide staining and flow cytometry. *Nature Protocols* **1**, 1458–1461.

[115] Izumida, S. Y, Onishi, E. Y, & Saito, M. (1998) Estimation of laser-induced breakdown threshold of microparticles in water. *Japanese Journal of Applied Physics* **37**, 2039–2042.

[116] Scherbaum, F. J, Knopp, R, & Kim, J. I. (1996) Counting of particles in aqueous solutions by laser-induced photoacoustic breakdown detection. *Applied Physics B: Lasers and Optics* **63**, 299–306.

[117] Arita, Y, Antkowiak, M, Venugopalan, V, Gunn-Moore, F. J, & Dholakia, K. (2012) Dynamics of primary and secondary microbubbles created by laser-induced breakdown of an optically trapped nanoparticle. *Physical Review E - Statistical, Nonlinear, and Soft Matter Physics* **85**, 016319.

[118] Arita, Y, Ploschner, M, Antkowiak, M, Gunn-Moore, F, & Dholakia, K. (2013) Laser-induced breakdown of an optically trapped gold nanoparticle for single cell transfection. *Optics Letters* **38**, 3402.

[119] Baumgart, J, Humbert, L, Boulais, E, Lachaine, R, Lebrun, J. J, & Meunier, M. (2012) Off-resonance plasmonic enhanced femtosecond laser optoporation and transfection of cancer cells. *Biomaterials* **33**, 2345–2350.

[120] Boulais, E, Lachaine, R, & Meunier, M. (2012) Plasma mediated off-resonance plasmonic enhanced ultrafast laser-induced nanocavitation. *Nano Letters* **12**, 4763–4769.

[121] Haladjova, E, Halacheva, S, Posheva, V, Peycheva, E, Moskova-Doumanova, V, Topouzova-Hristova, T, Doumanov, J, & Rangelov, S. (2015) Comblike Polyethylenimine-Based Polyplexes: Balancing Toxicity, Cell Internalization, and Transfection Efficiency via Polymer Chain Topology. *Langmuir* **31**, 10017–10025.

[122] Lukianova-Hleb, E. Y, Wagner, D. S, Brenner, M. K, & Lapotko, D. O. (2012) Cell-specific transmembrane injection of molecular cargo with gold nanoparticle-generated transient plasmonic nanobubbles. *Biomaterials* **33**, 5441–5450.

[123] Mirisola, M. G, Braun, R. J, & Petranovic, D. (2014) Approaches to study yeast cell aging and death. *FEMS Yeast Research* **14**, 109–118.

[124] Kwolek-Mirek, M & Zadrag-Tecza, R. (2014) Comparison of methods used for assessing the viability and vitality of yeast cells. *FEMS Yeast Research* **14**, 1068–1079.

[125] Chakraborty, C, Sharma, A. R, Sharma, G, Doss, C. G. P, & Lee, S. S. (2017) Therapeutic miRNA and siRNA: Moving from Bench to Clinic as Next Generation Medicine. *Molecular Therapy - Nucleic Acids* **8**, 132–143.

[126] Opalinska, J. B & Gewirtz, A. M. (2002) Nucleic-acid therapeutics: Basic principles and recent applications.

[127] Brachmann, C. B, Davies, A, Cost, G. J, Caputo, E, Li, J, Hieter, P, & Boeke, J. D. (1998) Designer deletion strains derived from Saccharomyces cerevisiae S288C: A useful set of strains and plasmids for PCR-mediated gene disruption and other applications. *Yeast* **14**, 115–132.

[128] Tlotleng, N, Vetten, M. A, Keter, F. K, Skepu, A, Tshikhudo, R, & Gulumian, M. (2016) Cytotoxicity, intracellular localization and exocytosis of citrate capped and PEG functionalized gold nanoparticles in human hepatocyte and kidney cells. *Cell Biology and Toxicology*.

[129] Chen, A. L, Hu, Y. S, Jackson, M. A, Lin, A. Y, Young, J. K, Langsner, R. J, & Drezek, R. A. (2014) Quantifying spectral changes experienced by plasmonic nanoparticles in a cellular environment to inform biomedical nanoparticle design. *Nanoscale Research Letters* **9**.

[130] Roth, G. A, Tahiliani, S, Neu-Baker, N. M, & Brenner, S. A. (2015) Hyperspectral microscopy as an analytical tool for nanomaterials.

[131] Schomaker, M, Heinemann, D, Kalies, S, Willenbrock, S, Wagner, S, Nolte, I, Ripken, T, Escobar, H. M, Meyer, H, & Heisterkamp, A. (2015) Characterization of nanoparticle mediated laser transfection by femtosecond laser pulses for applications in molecular medicine. *Journal of Nanobiotechnology* **13**, 1–15.

[132] Nedyalkov, N. N, Imamova, S, Atanasov, P. A, Tanaka, Y, & Obara, M. (2011) Interaction between ultrashort laser pulses and gold nanoparticles: Nanoheater and nanolens effect. *Journal of Nanoparticle Research* **13**, 2181–2193.

[133] Westermann, B & Neupert, W. (2000) Mitochondria-targeted green fluorescent proteins: Convenient tools for the study of organelle biogenesis in Saccharomyces cerevisiae. *Yeast* **16**, 1421–1427.

[134] Vallabhaneni, S & Chiller, T. M. (2016) Fungal Infections and New Biologic Therapies. *Current Rheumatology Reports* **18**, 1–10.

[135] Salame, T. M, Ziv, C, Hadar, Y, & Yarden, O. (2011) RNAi as a potential tool for biotechnological applications in fungi. *Applied Microbiology and Biotechnology* **89**, 501–512.

[136] Sengupta, A, Kelly, S. C, Dwivedi, N, Thadhani, N, & Prausnitz, M. R. (2014) Efficient intracellular delivery of molecules with high cell viability using nanosecond-pulsed laser-activated carbon nanoparticles. *ACS Nano* **8**, 2889–2899.

[137] Wiederhold, N. P. (2017) Antifungal resistance: current trends and future strategies to combat. *Infection and drug resistance* **10**, 249–259.

[138] Xiong, R, Sauvage, F, Fraire, J. C, Huang, C, De Smedt, S. C, & Braeckmans, K. (2023) Photothermal Nanomaterial-Mediated Photoporation. *Accounts of Chemical Research* **56**, 631–643.

[139] Raes, L, Pille, M, Harizaj, A, Goetgeluk, G, Van Hoeck, J, Stremersch, S, Fraire, J. C, Brans, T, de Jong, O. G, Maas-Bakker, R, Mastrobattista, E, Vader, P, De Smedt, S. C, Vandekerckhove, B, Raemdonck, K, & Braeckmans, K. (2021) Cas9 RNP transfection by vapor nanobubble photoporation for ex vivo cell engineering. *Molecular Therapy. Nucleic Acids* **25**, 696.

[140] Moazeni, M, Khoramizadeh, M. R, Kordbacheh, P, Sepehrizadeh, Z, Zeraati, H, Noorbakhsh, F, Teimoori-Toolabi, L, & Rezaie, S. (2012) RNA-Mediated Gene Silencing in Candida albicans: Inhibition of Hyphae Formation by Use of RNAi Technology. *Mycopathologia* **174**, 177–185.

[141] Hoyer, L. L, Freeman, B. A, Hogan, E. K, & Hernandez, A. G. (2024) Use of a Candida albicans SC5314 PacBio HiFi reads dataset to close gaps in the reference genome assembly, reveal a subtelomeric gene family, and produce accurate phased allelic sequences. *Frontiers in Cellular and Infection Microbiology* **14**, 1329438.

[142] Iracane, E, Arias-Sardá, C, Maufrais, C, Ene, I. V, d'Enfert, C, & Buscaino, A. (2024) Identification of an active RNAi pathway in Candida albicans. *Proceedings of the National Academy of Sciences of the United States of America* **121**, e2315926121.

[143] De Groot, P. W, Kraneveld, E. A, Qing, Y. Y, Dekker, H. L, Groß, U, Crielaard, W, De Koster, C. G, Bader, O, Klis, F. M, & Weig, M. (2008) The Cell Wall of the Human Pathogen Candida glabrata: Differential Incorporation of Novel Adhesin-Like Wall Proteins. *Eukaryotic Cell* **7**, 1951.

[144] Chithrani, B. D, Ghazani, A. A, & Chan, W. C. (2006) Determining the size and shape dependence of gold nanoparticle uptake into mammalian cells. *Nano Letters* **6**, 662–668.

[145] Alshangiti, D. M, Ghobashy, M. M, Alqahtani, H. A, El-Damhougy, T. K, & Madani, M. (2023) The energetic and physical concept of gold nanorod-dependent fluorescence in cancer treatment and development of new photonic compounds—review. *RSC Advances* **13**, 32223–32265.

[146] Domingo-Diez, J, Souiade, L, Manzaneda-González, V, Sánchez-Díez, M, Megias, D, Guerrero-Martínez, A, Ramírez-Castillejo, C, Serrano-Olmedo, J, & Ramos-Gómez, M. (2023) Effectiveness of Gold Nanorods of Different Sizes in Photothermal Therapy to Eliminate Melanoma and Glioblastoma Cells. *International journal of molecular sciences* **24**.

[147] Deinavizadeh, M, Kiasat, A. R, Shafiei, M, Sabaeian, M, Mirzajani, R, Zahraei, S. M, Khalili, F, Shao, M, Wu, A, Makvandi, P, & Hooshmand, N. (2024) Synergistic chemo-photothermal therapy using gold nanorods supported on thiol-functionalized mesoporous silica for lung cancer treatment. *Scientific Reports 2024 14:1* **14**, 1–12.

[148] Agarwal, A, Shao, X, Rajian, J. R, Zhang, H, Chamberland, D. L, Kotov, N. A, & Wang, X. (2011) Dual-mode imaging with radiolabeled gold nanorods. *Journal of Biomedical Optics* **16**, 051307.

[149] Mahns, A, Melchheier, I, Suschek, C. V, Sies, H, & Klotz, L. O. (2003) Irradiation of Cells with Ultraviolet-A (320-400 nm) in the Presence of Cell Culture Medium Elicits Biological Effects Due to Extracellular Generation of Hydrogen Peroxide. *Free Radical Research* **37**, 391–397.

[150] Xiong, R, Hua, D, Van Hoeck, J, Berdecka, D, Léger, L, De Munter, S, Fraire, J. C, Raes, L, Harizaj, A, Sauvage, F, Goetgeluk, G, Pille, M, Aalders, J, Belza, J, Van Acker, T, Bolea-Fernandez, E, Si, T, Vanhaecke, F, De Vos, W. H, Vandekerckhove, B, van Hengel, J, Raemdonck, K, Huang, C, De Smedt, S. C, & Braeckmans, K. (2021) Photothermal nanofibres enable safe engineering of therapeutic cells. *Nature Nanotechnology 2021 16:11* **16**, 1281–1291.

[151] Godar, D. E & Lucas, A. D. (1995) SPECTRAL DEPENDENCE OF UV-INDUCED IMMEDIATE AND DELAYED APOPTOSIS: THE ROLE OF MEMBRANE AND DNA DAMAGE. *Photochemistry and Photobiology* **62**, 108–113.

[152] Glazier, V. E. (2022) EFG1, Everyone's Favorite Gene in Candida albicans: A Comprehensive Literature Review. *Frontiers in Cellular and Infection Microbiology* **12**, 855229.

[153] Livak, K. J & Schmittgen, T. D. (2001) Analysis of relative gene expression data using real-time quantitative PCR and the 2(-Delta Delta C(T)) Method. *Methods (San Diego, Calif.)* **25**, 402–408.

[154] Tirlapur, U. K & König, K. (2002) Femtosecond near-infrared laser pulses as a versatile non-invasive tool for intra-tissue nanoprocessing in plants without compromising viability. *Plant Journal* **31**, 365–374.

[155] Cravener, M. V & Mitchell, A. P. (2020) Candida albicans Culture, Cell Harvesting, and Total RNA Extraction. *Bio-protocol* **10**.

[156] Zhang, H, Li, H. C, Miao, X. X, Hao, Z, Hai-Chao, L, & Xua-Xia, M. (2013) Feasibility, limitation and possible solutions of RNAi-based technology for insect pest control. *Insect science* **20**, 15–30.

[157] Barros, S. d. M, Whitaker, S. K, Sukthankar, P, Avila, L. A, Gudlur, S, Warner, M, Beltrão, E. I. C, & Tomich, J. M. (2016) A review of solute encapsulating nanoparticles used as delivery systems with emphasis on branched amphipathic peptide capsules. *Archives of Biochemistry and Biophysics* **596**, 22–42.

[158] Jarvis, D. L, Oker-Blom, C, & Summers, M. D. (1990) Role of glycosylation in the transport of recombinant glycoproteins through the secretory pathway of lepidopteran insect cells. *Journal of Cellular Biochemistry* **42**, 181–191.

[159] Bernales, S, Papa, F. R, & Walter, P. (2006) Intracellular signaling by the unfolded protein response.

[160] White, L. D, Coates, C. J, Atkinson, P. W, & O'Brochta, D. A. (1996) An eye color gene for the detection of transgenic non-drosophilid insects. *Insect Biochemistry and Molecular Biology* **26**, 641–644.

[161] Sijen, T, Fleenor, J, Simmer, F, Thijssen, K. L, Parrish, S, Timmons, L, Plasterk, R. H, & Fire, A. (2001) On the Role of RNA Amplification in dsRNA-Triggered Gene Silencing. *Cell* **107**, 465–476.

[162] Kemmerer, M & Bonning, B. C. (2020) Transcytosis of Junonia coenia densovirus VP4 across the gut epithelium of Spodoptera frugiperda (Lepidoptera: Noctuidae). *Insect Science* **27**, 22–32.

[163] Ussing, H. H & Zerahn, K. (1951) Active Transport of Sodium as the Source of Electric Current in the Short-circuited Isolated Frog Skin. *Acta Physiologica Scandinavica* **23**, 110–127.

[164] Granados, R. R, Li, G, & Blissard, G. W. (2007) Insect cell culture and biotechnology. *Virologica Sinica* **22**, 83–93.

[165] Sahay, G, Alakhova, D. Y, & Kabanov, A. V. (2010) Endocytosis of nanomedicines.

[166] Vélez, A. M & Fishilevich, E. (2018) The mysteries of insect RNAi: A focus on dsRNA uptake and transport.

[167] Simovic, S, Song, Y, Nann, T, & Desai, T. A. (2015) Intestinal absorption of fluorescently labeled nanoparticles. *Nanomedicine: Nanotechnology, Biology, and Medicine* **11**, 1169–1178.

[168] Gilleron, J, Querbes, W, Zeigerer, A, Borodovsky, A, Marsico, G, Schubert, U, Manygoats, K, Seifert, S, Andree, C, Stöter, M, Epstein-Barash, H, Zhang, L, Koteliansky, V, Fitzgerald, K, Fava, E, Bickle, M, Kalaidzidis, Y, Akinc, A, Maier, M, & Zerial, M. (2013) Image-based analysis of lipid nanoparticle-mediated siRNA delivery, intracellular trafficking and endosomal escape. *Nature Biotechnology* **31**, 638–646.

[169] Adriana Avila, L, R. M. M. Aps, L, Sukthankar, P, Ploscariu, N, Gudlur, S, Šimo, L, Szoszkiewicz, R, Park, Y, Y. Lee, S, Iwamoto, T, C. S. Ferreira, L, M. Tomich, J, Avila, L. A, Aps, L. R, Sukthankar, P, Ploscariu, N, Gudlur, S, Šimo, L, Szoszkiewicz, R, Park, Y, Lee, S. Y, Iwamoto, T, Ferreira, L. C, Tomich, J. M, Adriana Avila, L, R. M. M. Aps, L, Sukthankar, P, Ploscariu, N, Gudlur, S, Šimo, L, Szoszkiewicz, R, Park, Y, Y. Lee, S, Iwamoto, T, C. S. Ferreira, L, & M. Tomich, J. (2015) Branched amphiphilic cationic oligopeptides form peptiplexes with DNA: A study of their biophysical properties and transfection efficiency. *Molecular Pharmaceutics* **12**, 706–715.

[170] Ramos, A. P. (2017) in *Nanocharacterization Techniques*, eds. Da Roz, A. L, Ferreira, M, de Lima Leite, F, & Oliveria, O. N. (William Andrew Publishing), pp. 99–110.

[171] Maguire, C. M, Rösslein, M, Wick, P, & Prina-Mello, A. (2018) Characterisation of particles in solution–a perspective on light scattering and comparative technologies.

[172] Shao, X. R, Wei, X. Q, Song, X, Hao, L. Y, Cai, X. X, Zhang, Z. R, Peng, Q, & Lin, Y. F. (2015) Independent effect of polymeric nanoparticle zeta potential/surface charge, on their cytotoxicity and affinity to cells. *Cell Proliferation* **48**, 465–474.

[173] Natarajan, P, Roberts, J. D, Kunte, N, Hunter, W. B, Fleming, S. D, Tomich, J. M, & Avila, L. A. (2020) A Study of the Cellular Uptake of Magnetic Branched Amphiphilic Peptide Capsules. *Molecular Pharmaceutics* **17**, 2208–2220.

[174] Vercauteren, D, Vandenbroucke, R. E, Jones, A. T, Rejman, J, Demeester, J, De Smedt, S. C, Sanders, N. N, & Braeckmans, K. (2010) The use of inhibitors to study endocytic pathways of gene carriers: Optimization and pitfalls. *Molecular Therapy* **18**, 561–569.

[175] Dutta, D & Donaldson, J. G. (2012) Search for inhibitors of endocytosis. *Cellular Logistics* **2**, 203–208.

[176] Sato, K, Nagai, J, Mitsui, N, Ryoko Yumoto, & Takano, M. (2009) Effects of endocytosis inhibitors on internalization of human IgG by Caco-2 human intestinal epithelial cells. *Life Sciences* **85**, 800–807.

[177] Saha, K, Kim, S. T, Yan, B, Miranda, O. R, Alfonso, F. S, Shlosman, D, & Rotello, V. M. (2013) Surface functionality of nanoparticles determines cellular uptake mechanisms in mammalian cells. *Small* **9**, 300–305.

[178] Hillaireau, H & Couvreur, P. (2009) Nanocarriers' entry into the cell: Relevance to drug delivery.

[179] Hodgson, J. J, Buchon, N, & Blissard, G. W. (2019) Identification of insect genes involved in baculovirus AcMNPV entry into insect cells. *Virology* **527**, 1–11.

[180] Long, G, Pan, X, Kormelink, R, & Vlak, J. M. (2006) Functional Entry of Baculovirus into Insect and Mammalian Cells Is Dependent on Clathrin-Mediated Endocytosis. *Journal of Virology* **80**, 8830–8833.

[181] Kunz, D, Oliveira, G. B, Uchôa, A. F, Samuels, R. I, Macedo, M. L. R, & Silva, C. P. (2017) Receptor mediated endocytosis of vicilin in Callosobruchus maculatus (Coleoptera: Chrysomelidae) larval midgut epithelial cells. *Comparative Biochemistry and Physiology Part - B: Biochemistry and Molecular Biology* **210**, 39–47.

[182] Mercer, J & Helenius, A. (2009) Virus entry by macropinocytosis.

[183] Paillard, A, Hindré, F, Vignes-Colombeix, C, Benoit, J. P, & Garcion, E. (2010) The importance of endo-lysosomal escape with lipid nanocapsules for drug subcellular bioavailability. *Biomaterials* **31**, 7542–7554.

[184] Ballabio, A. (2016) The awesome lysosome. *EMBO Molecular Medicine* **8**, 73–76.

[185] Battistella, C & Klok, H. A. (2017) Controlling and Monitoring Intracellular Delivery of Anticancer Polymer Nanomedicines.

[186] Meng, Z, Luan, L, Kang, Z, Feng, S, Meng, Q, & Liu, K. (2017) Histidine-enriched multifunctional peptide vectors with enhanced cellular uptake and endosomal escape for gene delivery. *J. Mater. Chem. B* **5**, 74–84.

[187] Shete, H. K, Prabhu, R. H, & Patravale, V. B. (2014) Endosomal escape: A bottleneck in intracellular delivery.

[188] Freeman, E. C, Weiland, L. M, & Meng, W. S. (2013) Modeling the proton sponge hypothesis: Examining proton sponge effectiveness for enhancing intracellular gene delivery through multiscale modeling. *Journal of Biomaterials Science, Polymer Edition* **24**, 398–416.

[189] Shukla, J. N, Kalsi, M, Sethi, A, Narva, K. E, Fishilevich, E, Singh, S, Mogilicherla, K, & Palli, S. R. (2016) Reduced stability and intracellular transport of dsRNA contribute to poor RNAi response in lepidopteran insects. *RNA Biology* **13**, 656–669.

[190] Funhoff, A. M, van Nostrum, C. F, Koning, G. A, Schuurmans-Nieuwenbroek, N. M, Crommelin, D. J, & Hennink, W. E. (2004) Endosomal escape of polymeric gene delivery complexes is not always enhanced by polymers buffering at low pH. *Biomacromolecules* **5**, 32–39.

[191] Denecke, S, Swevers, L, Douris, V, & Vontas, J. (2018) How do oral insecticidal compounds cross the insect midgut epithelium? *Insect Biochemistry and Molecular Biology* **103**, 22–35.

[192] Aronstein, K, Pankiw, T, & Saldivar, E. (2006) SID-I is implicated in systemic gene silencing in the honey bee. *Journal of Apicultural Research* **45**, 20–24.

[193] Cappelle, K, De Oliveira, C. F, Van Eynde, B, Christiaens, O, & Smagghe, G. (2016) The involvement of clathrin-mediated endocytosis and two Sid-1-like transmembrane proteins in double-stranded RNA uptake in the Colorado potato beetle midgut. *Insect Molecular Biology* **25**, 315–323.

[194] Luo, Y, Wang, X, Yu, D, & Kang, L. (2012) The SID-1 double-stranded RNA transporter is not required for systemic RNAi in the migratory locust. *RNA Biology* **9**, 663–671.

[195] Tuma, P. L & Hubbard, A. L. (2003) Transcytosis: Crossing Cellular Barriers. *https://doi.org/10.1152/physrev.00001.2003* **83**, 871–932.

[196] Gibco. (2017) Growth and Maintenance of Insect Cell Lines - User Guide. *ThermoFisher Scientific*.

[197] Hunziker, W, Andrew Whitney, J, & Mellman, I. (1991) Selective inhibition of transcytosis by brefeldin A in MDCK cells. *Cell* **67**, 617–627.

[198] Kaksonen, M & Roux, A. (2018) Mechanisms of clathrin-mediated endocytosis.

[199] Roger, E, Lagarce, F, Garcion, E, & Benoit, J. P. (2009) Lipid nanocarriers improve paclitaxel transport throughout human intestinal epithelial cells by using vesicle-mediated transcytosis. *Journal of Controlled Release* **140**, 174–181.

[200] Manke, A, Wang, L, & Rojanasakul, Y. (2013) Mechanisms of nanoparticle-induced oxidative stress and toxicity.

[201] Yu, Z, Li, Q, Wang, J, Yu, Y, Wang, Y, Zhou, Q, & Li, P. (2020) Reactive Oxygen Species-Related Nanoparticle Toxicity in the Biomedical Field.

[202] Ansari, M. O, Parveen, N, Ahmad, M. F, Wani, A. L, Afrin, S, Rahman, Y, Jameel, S, Khan, Y. A, Siddique, H. R, Tabish, M, & Shadab, G. G. (2019) Evaluation of DNA interaction, genotoxicity and oxidative stress induced by iron oxide nanoparticles both in vitro and in vivo: attenuation by thymoquinone. *Scientific Reports* **9**.

[203] Di Meo, S, Reed, T. T, Venditti, P, & Victor, V. M. (2016) Role of ROS and RNS Sources in Physiological and Pathological Conditions.

[204] Hardy, M, Zielonka, J, Karoui, H, Sikora, A, Michalski, R, Podsiadły, R, Lopez, M, Vasquez-Vivar, J, Kalyanaraman, B, & Ouari, O. (2018) Detection and Characterization of Reactive Oxygen and Nitrogen Species in Biological Systems by Monitoring Species-Specific Products.

[205] Gurusamy, D, Mogilicherla, K, Shukla, J. N, & Palli, S. R. (2020) Lipids help double-stranded RNA in endosomal escape and improve RNA interference in the fall armyworm, Spodoptera frugiperda. *Archives of Insect Biochemistry and Physiology* **104**, e21678.

[206] Price, D. R & Gatehouse, J. A. (2008) RNAi-mediated crop protection against insects. *Trends in Biotechnology* **26**, 393–400.

[207] Yu, N, Christiaens, O, Liu, J, Niu, J, Cappelle, K, Caccia, S, Huvenne, H, & Smagghe, G. (2013) Delivery of dsRNA for RNAi in insects: An overview and future directions.

[208] Kumar, S, Joshi, P. C, Nath, P, & Singh, V. K. (2018) Impacts of Insecticides on Pollinators of Different Food Plants. *Entomology, Ornithology & Herpetology: Current Research*.

[209] Terenius, O, Papanicolaou, A, Garbutt, J. S, Eleftherianos, I, Huvenne, H, Kanginakudru, S, Albrechtsen, M, An, C, Aymeric, J. L, Barthel, A, Bebas, P, Bitra, K, Bravo, A, Chevalier, F, Collinge, D. P, Crava, C. M, de Maagd, R. A, Duvic, B, Erlandson, M, Faye, I, Felföldi, G, Fujiwara, H, Futahashi, R, Gandhe, A. S, Gatehouse, H. S, Gatehouse, L. N, Giebultowicz, J. M, Gómez, I, Grimmelikhuijzen, C. J, Groot, A. T, Hauser, F, Heckel, D. G, Hegedus, D. D, Hrycaj, S, Huang, L, Hull, J. J, Iatrou, K, Iga, M, Kanost, M. R, Kotwica, J, Li, C, Li, J, Liu, J, Lundmark, M, Matsumoto, S, Meyering-Vos, M, Millichap, P. J, Monteiro, A, Mrinal, N, Niimi, T, Nowara, D, Ohnishi, A, Oostra, V, Ozaki, K, Papakonstantinou, M, Popadic, A, Rajam, M. V, Saenko, S, Simpson, R. M, Soberón, M, Strand, M. R, Tomita, S, Toprak, U, Wang, P, Wee, C. W, Whyard, S, Zhang, W, Nagaraju, J, ffrench Constant, R. H, Herrero, S, Gordon, K, Swevers, L, & Smagghe, G. (2011) RNA interference in Lepidoptera: an overview of successful and unsuccessful studies and implications for experimental design. *Journal of insect physiology* **57**, 231–245.

[210] Avila, L. A, Chandrasekar, R, Wilkinson, K. E, Balthazor, J, Heerman, M, Bechard, J, Brown, S, Park, Y, Dhar, S, Reeck, G. R, & Tomich, J. M. (2018) Delivery of

lethal dsRNAs in insect diets by branched amphiphilic peptide capsules. *Journal of Controlled Release* **273**, 139–146.

[211] Debnath, N & Das, S. (2018) Nanoparticle mediated RNAi in insects: A novel feeding assay based method for controlling insect pests. *Proceedings of the IEEE Conference on Nanotechnology* **2019-January**.

[212] de Barros, S. M, Adriana Avila, L, K. Whitaker, S, E. Wilkinson, K, Sukthankar, P, I. C. Beltrão, E, & M. Tomich, J. (2017) Branched Amphipathic Peptide Capsules: Different Ratios of the Two Constituent Peptides Direct Distinct Bilayer Structures, Sizes, and DNA Transfection Efficiency. *Langmuir* **33**, 7096–7104.

[213] Mo, D, Chen, Y, Jiang, N, Shen, J, & Zhang, J. (2020) Investigation of Isoform Specific Functions of the V-ATPase a Subunit During Drosophila Wing Development. *Frontiers in Genetics* **11**, 544283.

[214] Wieczorek, H, Beyenbach, K. W, Huss, M, & Vitavska, O. (2009) Vacuolar-type proton pumps in insect epithelia. *Journal of Experimental Biology* **212**, 1611–1619.

[215] Pamarthy, S, Kulshrestha, A, Katara, G. K, & Beaman, K. D. (2018) The curious case of vacuolar ATPase: Regulation of signaling pathways. *Molecular Cancer* **17**, 1–9.

[216] Dow, J. A. T. (1995) V-ATPases in Insects. pp. 75–102.

[217] Amrein, H & Thorne, N. (2005) Gustatory Perception and Behavior in Drosophila melanogaster. *Current Biology* **15**, R673–R684.

[218] Zhou, D, van Loon, J. J, & Wang, C. Z. (2010) Experience-based behavioral and chemosensory changes in the generalist insect herbivore Helicoverpa armigera exposed to two deterrent plant chemicals. *Journal of Comparative Physiology A: Neuroethology, Sensory, Neural, and Behavioral Physiology* **196**, 791–799.

[219] Wang, H, Zhao, R, Gao, J, Xiao, X, Yin, X, Hu, S, Zhang, Y, Liang, P, & Gu, S. (2024) Two cuticle-enriched chemosensory proteins confer multi-insecticide resistance in Spodoptera frugiperda. *International Journal of Biological Macromolecules* **266**, 130941.

[220] Villegas-Mendoza, J. M & Rosas-García, N. M. (2013) Visual and Gustatory Responses of Spodoptera frugiperda (Lepidoptera: Noctuidae) Larvae to Artificial Food Dyes. *https://doi.org/10.1653/024.096.0350* **96**, 1102–1106.

[221] Ramkumar, G, Asokan, R, Prasannakumar, N. R, Kariyanna, B, Karthi, S, Alwahibi, M. S, Elshikh, M. S, Abdel-Megeed, A, Ghaith, A, Senthil-Nathan, S, Kalaivani, K, Hunter, W. B, & Krutmuang, P. (2021) RNA Interference Suppression of v-ATPase B and Juvenile Hormone Binding Protein Genes Through Topically Applied dsRNA on Tomato Leaves: Developing Biopesticides to Control the South American Pinworm, Tuta absoluta (Lepidoptera: Gelechiidae). *Frontiers in Physiology* **12**, 742871.

[222] Camargo, R. A, Barbosa, G. O, Possignolo, I. P, Peres, L. E, Lam, E, Lima, J. E, Figueira, A, & Marques-Souza, H. (2016) RNA interference as a gene silencing tool to control Tuta absoluta in tomato (Solanum lycopersicum). *PeerJ* **2016**, e2673.

[223] Cipriano, D. J, Wang, Y, Bond, S, Hinton, A, Jefferies, K. C, Qi, J, & Forgac, M. (2008) Structure and Regulation of the Vacuolar ATPases. *Biochimica et biophysica acta* **1777**, 599.

[224] MacLeod, K. J, Vasilyeva, E, Baleja, J. D, & Forgac, M. (1998) Mutational analysis of the nucleotide binding sites of the yeast vacuolar proton-translocating ATPase. *Journal of Biological Chemistry* **273**, 150–156.

[225] Sato, K, Miyata, K, Ozawa, S, & Hasegawa, K. (2019) Systemic RNAi of V-ATPase subunit B causes molting defect and developmental abnormalities in Periplaneta fuliginosa. *Insect Science* **26**, 721–731.